High-pressure Raman study of graphene: a spectroscopic evidence for the diamondol

Luiz Gustavo Pimenta Martins

Março 2015

Universidade Federal de Minas Gerais - UFMG
Instituto de Ciências Exatas - ICEx
Programa de Pós-Graduação em Física

High-pressure Raman study of graphene: a spectroscopic evidence for the diamondol

Luiz Gustavo Pimenta Martins

Orientador: Prof. Luiz Gustavo de Oliveira Lopes Cançado

Dissertação apresentada ao departamento de Física da Universidade Federal de Minas Gerais, para a obtenção de Título de Mestre em Física
Área de Concentração: Física da Matéria Condensada

2015

“ Aos meus pais, Carlos e Clea ...

ao meu amor, Alice...”

Agradecimentos

A vida é definitivamente imprevisível (por mais contraditório que isso possa soar). Quem diria que a matéria mais odiada por mim nos tempos de colégio se tornaria o meu objeto de trabalho! Com o perdão do clichê, a caminhada foi longa até aqui e muitos foram os percalços, mas tenho a certeza de estar no caminho certo. E muitos foram os que trilharam esse caminho comigo. Portanto, a conquista de mais essa etapa é de todos vocês também.

Agradeço aos meus pais por serem o meu alicerce e a minha referência de seres verdadeiramente humanos. À minha mãe, por ser a pessoa mais generosa e justa desse mundo, estando presente e me apoiando incondicionalmente em todos os momentos da minha vida, além de me ensinar, através de sua história de vida, o poder da determinação. Ao meu pai, pela exemplo de serenidade, equilíbrio e honestidade, além do carinho e empolgaçao em ter um filho cientista! Herdei de você a curiosidade, a principal característica de todo aquele que deseja fazer ciência. Ao meu irmão, pela amizade, preocupação e pelos conselhos ao longo da minha vida, e à sua esposa Sílvia e ao meu sobrinho André, pelo carinho. Às minhas irmãs Ana Luiza, Marcele e Noara pela amizade e presença desde sempre. À Aparecida por cuidar de mim ao longo de todos esses anos. À Tia Eliene, Tio Ildeu e Tia Lêda por extenderem o conceito de pai e mãe. À Tia Queu, Tia Lula e a todos os Neves por todo apoio e pelas farras.

Agradeço à Alice, meu amor e meu porto seguro, por ser a minha maior e melhor compania sempre. Aos meus sogros, Laura e ao Orlando por abrir as portas de sua casa, (que acabou se tornando a minha 1^a casa em BH rs), e por tudo que fizeram e fazem por mim, tendo uma contribuição direta em diversas etapas do meu mestrado.

Ao Gusta, por ter acreditado em mim desde o início, me apontando uma vocação para Física experimental que até então eu não sabia que possuía, e por ser o exemplo de profissional a que tento me espelhar, combinando a paixão pela Física experimental com o sólido conheci-

mento teórico aplicado em prol da geração do conhecimento. Agradeço por todas as excelentes oportunidades que me proporcionou, pelos conversas fiadas e pelos jogos do Galo!

A todo o pessoal da UFC por ter me recebido da melhor maneira possível em todas as minhas idas e por ter viabilizado os experimentos de Raman sob alta pressão: Professores Alexandre Paschoal, Paulo Tarso, Nádia Ferreira, Antônio Gomes e Acrísio Lins. Sem a contribuição e dedicação de vocês, esse trabalho não teria sido possível, literalmente. Agradecço ao Paschoal, ao Edilan, à tia Valdira e à Gabi por terem me hospedado e por me fazer sentir em casa. Agradeço à minha família em Fortaleza: Tio Joaquim, Tia Valdira e meus primos (e respectivas esposas) Boris, Breno, Bráulio, Bruno e Gabriela, por terem feito minhas idas a Fortaleza mais divertidas.

I would like to thank Professor Jing Kong for hosting me in the NanoMaterials and Electronics Group (NME) in MIT where all the samples of this work were produced, also for being the perfect example of brightness and kindness. I also would like to thank all people from the NME group for all support and fun I had during my time in MIT. I would like to thank Professor Mildred Dresselhaus for the fruitful discussions and for the example of how science can be used to promote social equality. Ao Paulo T. Araújo (Simpa) pelas orientações acadêmicas e não acadêmicas.

Aos Amigores, aos Mansos, aos amigos do Dom Bosco, da EQ, aos amigos do Vale do Aço, aos do Vale do Aço que estão em BH e aos amigos que não se encaixaram em nenhuma das categorias anteriores: vocês fazem minha vida muito melhor. Em especial gostaria de agradecer aos meus amigos/irmãos Matheus, Ricardo, Carlos Alberto (Gurta), Transitions (Tiago), Amigor, Neto e Bruninha que me deram força durante um dos momentos mais difíceis da minha vida. Serei eternamente grato a vocês.

À Rosana, por sempre me indicar o caminho certo e por me explicar o Princípio da Incerteza na prática rs.

Aos meus amigos do Departamento de Física da UFMG, Paloma (Cabeça), Paula Favela, Thales e Paulim que fizeram esses dois anos de mestrado muito melhores. Ao Lucas Cpamm pelas conversas e apoio para as aplicaçoes de doutorado nos EUA.

Ao Wagner Rodrigues pelo exemplo de amor à Física e a orientação/discussão no processo de fabricação das amostras de grafeno sob silício para os experimentos de alta pressão. Também gostaria de agradecer aos colegas Eduardo Ney e Thiago Bueno por me auxiliar nesse processo.

Ao Mario Sérgio pela paciência ao responder as milhares de dúvidas das mais diversas áreas da Física que já lhe perguntei, além das discussões em conjunto com o colega Matheus Matos, que contribuiram diretamente para esse trabalho.

Ao Ado pela visão de correlação entre ciência e inovação e a todas as discussões e contribuições diretas a esse trabalho.

Ao Chubaka pelos galhos quebrados e pelas contribuiçes a esse trabalho.

A todos os colegas do Laboratório de Nano-Espectroscopia pela convivência.

A todos os professores do Departamento de Física da UFMG que contribuiram com a minha formação.

A todos os outros funcionários do departamento de Física da UFMG, ao pessoal da limepza, das secretarias e às bibliotecárias. Em especial à Shirley por sempre me ajudar em tudo que precisei.

Aos Programas de Pós Graduação em Física da UFMG e da UFC e à Rede de Nano-Instrumentação em Espectrosocpia Óptica por financiar minhas idas à UFC.

Ao CNPq e ao povo brasileiro pelo auxílio financeiro.

E a Deus por tudo.

Resumo

Nessa dissertação investigou-se o efeito de altas pressões sobre o espectro Raman de bicamadas de grafeno CVD depositadas sobre substratos de Teflon. Para tanto, foi utilizada uma célula de bigorna de diamante (DAC) com água como meio transmissor de pressão. Os espectros foram obtidos com excitação em 488 nm e 532 nm. Inicialmente foi feito um estudo detalhado das propriedades eletrônicas e vibracionais do grafeno, bem como da interação entre essas. Em seguida investigou-se o processo de Espalhamento Raman e as origens da banda G no grafeno, assim como as perturbações causadas a essa banda por efeitos de dopagem e distorção (strain). Obteve-se um valor númerico para a dispersão da banda G em função da pressão igual a 5 cm^{-1}/GPa através de uma combinação de análise teórica e resultados experimentais. Este valor está de acordo com observações experimentais para amostras de grafeno suspenso sujeitas a altas pressões. Os resultados do experimento fornecem fortes evidências da ocorrência de uma transição de fase de uma estrutura sp^2 para uma estrutura híbrida $sp^2 - sp^3$ ocorrida entre $5 - 6$ GPa. A transição é reversível com a redução da pressão. As principais evidências para essa transição foram o deslocamento para maiores frequências (ω_G) e a diminuição da largura a meia altura da banda G (Γ_G) com o aumento da energia de excitação do laser e a mudança de regime da curva $\omega_G \times P$. Foi proposto que a estrutura com hibridização sp^3 tem origem na formação do diamondol, um diamante hidroxilado bidimensional formado por duas camadas de átomos de carbono hibridizadas em sp^3. Foi levantada a hipótese de que a camada superior sofreu uma hidroxilação entre $5 - 6$ GPa, seguida de um "descolamento" do diamondol do substrato de Teflon em 9.5 GPa, resultando em uma hidroxilação da camada inferior. Essa hipótese é consistente com os dados obtidos das variações de ω_G e Γ_G em funcção da pressão, que permitem inferir o conteúdo de carbono sp^3 do sistema, e com o fato de o grafeno realmente ter se "descolado" do substrato de Teflon em algumas regiões após a abertura da DAC. Para testar a hipótese do diamondol, mono e bicamada de grafeno CVD sobre um substrato de Teflon foram submetidas a altas pressões usando água e Nujol (óleo mineral) respectivamente, como meios transmissores de pressão. Não foram observadas dispersão na banda G, mudança no regime

da curva $\omega_G \times P$, nem mudança de Γ_G com excitação do laser em nenhuma das amostras, o que corrobora com a hipótese do diamondol. Observou-se também o surgimento de uma nova banda em torno de 620 cm^{-1} a pressões superiores a 1 GPa e as possíveis origens dessa banda foram discutidas. Se a hipótese do diamondol for confirmada, esse trabalho irá abrir novas perspectivas para a síntese de materiais bidimensionais através de experimentos de alta pressão.

Palavras-chave: grafeno CVD, altas pressões, transição de fase, diamondol.

Abstract

In this dissertation, the effect of high pressures on double transferred CVD graphene sitting on a Teflon substrate were investigated via Raman spectroscopy in a diamond anvil cell (DAC) using water as the pressure transmitting media (PTM). The Raman spectra were acquired with both 488 nm and 532 nm excitation light sources. Initially, a detailed study of the electronic and vibrational properties of graphene, as well as the interaction between them, was performed. Then, an investigation on the origin of the G band in graphene was carried out, as well as the perturbations to this band caused by strain and doping. A numerical value for the slope of G band frequency with pressure ($\partial\omega_G/\partial P$) of 5 cm^{-1}/GPa was obtained via a combination of theoretical analysis and experimental data. This value agrees with experimental observations for free-standing graphene samples subjected to high pressures. The results provide strong evidence of a phase transition from a sp^2 to a $sp^2 - sp^3$ mixed structure at 5 – 6 GPa, reversible upon pressure release. The main evidences were the blueshift of the G band frequency (ω_G) and the decrease of G band's full width at half maximum (Γ_G) with increasing excitation energy, and the change of régime of the $\omega_G \times P$ curve. Based on the experimental data, we propose the formation of diamondol, a 2D hydroxylated diamond consisting of two layers of sp^3 carbon. We hypothesized that the top layer was hydroxylated at 5 – 6 GPa, followed by a detachment of the diamondol from the Teflon substrate at 9.5 GPa, which in turn led to the hydroxylation of the bottom layer. This hypothesis is consistent with the sp^3 content of the system inferred from the variation of ω_G and Γ_G data, and with the fact that graphene was found to be detached from the Teflon substrate in some regions after the DAC was opened and the water evaporated. To test the diamondol hypothesis, mono and double layer CVD graphene sitting on a Teflon substrate were compressed using water and Nujol (mineral oil) as PTMs, respectively. No dispersion of the G band, change in the $\omega_G \times P$ curve or any net decrease in Γ_G with excitation energy were observed for both systems, corroborating with the diamondol hypothesis. The rise of a new band at $\sim$ 620 cm^{-1} under 1 GPa and above was also observed, and possible origins

for this band were proposed. If the diamondol hypothesis is confirmed, this work will open up directions for synthesizing new 2D materials with remarkable properties via high pressure experimental routes.

Keywords: CVD graphene, high pressures, phase transition, diamondol.

Contents

Introduction

High-pressure experiments conducted with graphite at room temperature using different pressure transmitting media (PTM) indicates that this material goes through a phase transition between 10-20 GPa [1, 2, 3, 4, 5, 6]. The new phase, as well as its properties, could be detected through different experimental techniques. High-pressure in situ X-ray diffraction experiments indicate new additional peaks around 14 GPa [1]. Inelastic X-ray scattering reveals that half of the π bonds between graphite layers is converted to σ bonds at 17 GPa [2]. Raman measurements and x-ray diffraction studies indicate an abrupt broadening of G band's full-width at half-maximum, Γ_G, around 10 GPa and the subsequent loss of that signal around 14 GPa, coinciding with the loss of graphite diffraction peaks at that same pressure [3]. The abrupt broadening of Γ_G was assigned to the formation of sp^3 bonds. Optical observations of graphite single crystals indicate the formation of a transparent phase at 18 GPa [4] and a drastic drop on its reflectivity around 16 GPa [5]. Electrical resistivity measurements reveal a rapid increase in resistivity for pressures above 15 GPa [6]. The new phase is superhard, capable of indenting the diamond used in the high-pressure apparatus [2]. The scattered values for the transition pressure found in literature reveals that the phase transition is very sensitive to the nature of the starting material as well as to the nature of the pressure applied to the sample [1]. Depending on the maximum pressure reached, the transformation is reversible [1, 2, 3, 4] showing large hysteresis [1, 3, 4]. Different models of the structure of this new phase were proposed to explain these experimental results [1, 2, 7, 8, 9, 10], being generally accepted that this new phase is formed by the appearance of sp^3 bonds between graphite layers during compression [11].

After the discovery of graphene, these high-pressure experiments were conducted with mono- and few-layer graphene [11, 12, 13, 14, 15] in order to study the effect of the applied pressure

on the properties of these materials. Ressonant Raman Spectroscopy (RRS) has proven to be an efficient technique to determine these materials' properties [16, 17], therefore RRS has been the main chosen technique to investigate the effects of applied pressure on graphene. A phase transition in graphene nanoplates around 15 GPa [11] was identified by Raman Spectroscopy. Similarly to graphite, the transition was related to an abrupt broadening of Γ_G. X-ray measurements in few layer graphene indicated the loss of the diffraction peak with increasing pressure for an interlayer distance of 2.8 Å[12]. The effects of strain and doping from the PTM as the pressure is increased were also studied trough RRS. An important parameter in these studies is the G band's position (ω_G) since it is directly affected by strain and doping. The derivative of ω_G with respect to the pressure ($\partial\omega_G/\partial P$) give information about how these two parameters evolve with increasing pressure. However, there is no agreement regarding the contributions of doping and strain to the displacement of ω_G in literature data [13, 14, 15]. Nicolle et al. [13] considered both factors and reported giant doping levels in graphene and bilayer graphene immersed in alcohol mixture. Filintoglou et al. [14] suggested that any pressure-induced doping is too small to influence the pressure response of graphene, which is rather determined by the compressibility of the substrate and the graphene interaction with the substrate and the PTM. Proctor et al. [15] also considered only mechanical effects to explain the pressure response of graphene, mentioning that doping effects could explain the difference in the observed behavior of graphene and graphite under pressure. The only common agreement in all these works is that $\partial\omega_G/\partial P$ is positive, and its value depend on both, number of layers and PTM.

An interesting effect involving graphene under high-pressure was observed by Barboza et al. [18]. In their work, ab initio calculations show that two layers of graphene under compression can be turned to a 2D hydroxilated diamond, called diamondol, if the top layer is covered with hydroxyl groups (Fig.1).

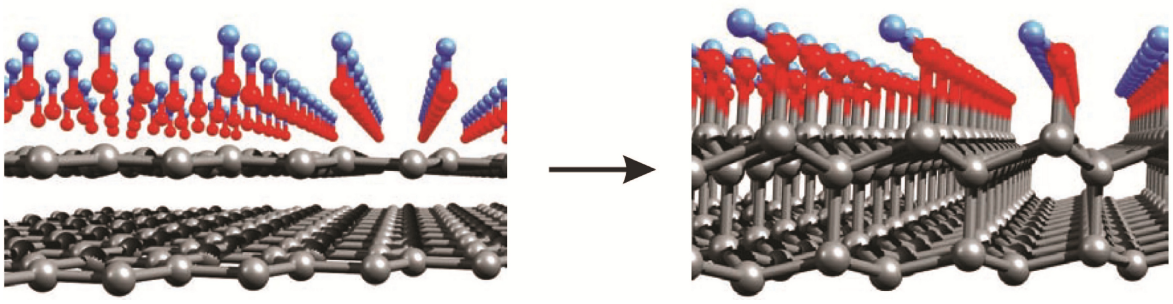

Figure 1: The formation of diamondol. Two layers of graphene are under compression while the topmost is covered with hydroxyl groups. The result is a 2D hydroxylated diamond called diamondol. Figure taken from Ref. [18].

The top layer becomes fully sp^3 hybridized with the four first neighbors, while the bottom layer has a carbon atom per unit cell, with only three neighbors, leaving a dangling bond. This periodic array of dangling bonds gives rise to an important feature of the electronic dispersion close to the Fermi level: the two spin polarized bands, indicated by red and blue curves in Fig.2. As a result, an energy gap of 0.6 eV opens up and the system acquires a magnetic moment of one Bohr magneton per unit cell, making diamondol a 2D ferromagnetic semiconductor.

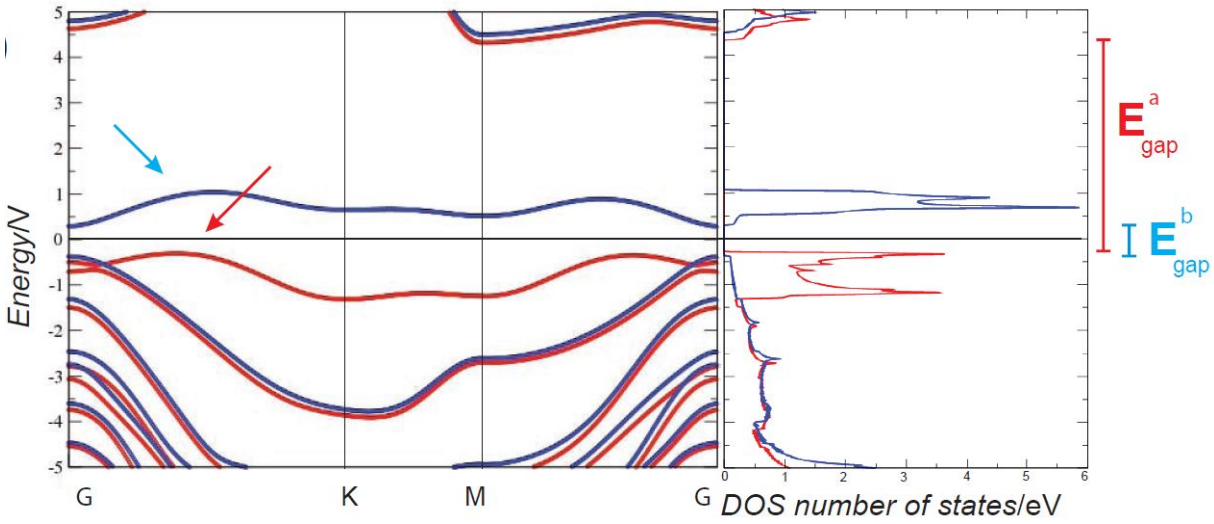

Figure 2: Electronic dispersion (left) and electron density of states for diamondol (right). Figure taken from [18].

A strong evidence of the experimental realization of the diamondol hypothesis was obtained through electric force microscopy (EFM) experiments. EMF was used to both inject and monitor charges and to apply pressure on mono-, bi-, and multi-layer graphene, while the water content on the sample surface was controlled by regulating the temperature of the experiment. It was observed a strong inhibition on the charging efficiency for bilayer and multilayer graphene as the tip pressure increased, while monolayer charging was pressure-independent [18].

All these works show that there are many opened questions and a vast field to be explored involving graphene under high pressures. In this context, in order to observe a phase transition involving the formation of sp^3 carbon, double layer CVD graphene was subjected to high pressures in a diamond anvil cell (DAC), while the Raman spectra was acquired using water as a pressure transmission medium (PTM).

This dissertation is arranged as follows. In chapter 1 we start from the electronic structure of the carbon atom, and move to the electronic structure of graphene, which is followed by a

classical treatment of the normal modes of vibration in graphene, and an introduction to the (quantum mechanical) concept of phonon. We finish this chapter by studying the interaction between the electrons and the vibrating lattice (the electron-phonon interaction) which is, according to the author's opinion, the most important single concept to understand the Raman spectrum of graphene. Chapter 2 covers the Raman process through a quantum mechanical approach. Chapter 3 is the key chapter of this dissertation, providing the basis for understanding the experimental results. The perturbations to the G band from mechanical strain and doping are introduced. An important result obtained in this chapter is a value for the slope of the G band frequency with pressure ($\partial\omega_G/\partial P$), which was obtained via a combination of theoretical analysis and experimental data. This value agrees with experimental observations for free-standing graphene samples. Chapters 4 to 6 cover the original contribution of this dissertation. Chapter 4 provides a detailed description about the sample fabrication process, covering both, the synthesis of graphene by the chemical vapor deposition (CVD) technique, and the direct transfer of graphene onto Teflon substrates. Chapter 5 covers the high-pressure Raman experiment. The results indicate that graphene undergoes a phase transition to a mixed $sp^2 - sp^3$ phase. To explain the results, we discuss how the Raman data is consistent with the hypothesis that the two layer graphene has became a diamondol under high-pressure conditions, and using water as PTM. We also report on the appearance of a new Raman band centered at ~ 620 cm^{-1} under 1 Gpa and upwards, and propose explanations for its origin. In Chapter 6 the conclusions and perspectives for future work and applications are drawn.

Chapter 1

Graphene

1.1 Carbon atom: electronic hybridization

The electronic configuration of a carbon atom in its ground state is $1s^2\ 2s^2\ 2p^2$, with four valence electrons at the $2s$ and $2p$ levels, and two core electrons at the 1s level. Based on its electronic configuration, it is physically sound that carbon should be chemically divalent, with two $2p$ electrons involved in chemical bonds, the other two $2s$ electrons being chemically inert. However, monoatomic carbon materials are found in several forms in which carbon atoms are covalent bonded to two, three, and four neighboring carbon atoms as in carbynes [19], graphene, and diamond respectively. The reason why carbon atoms are able to form such distinct structures is related to their many possible electronic configurations, which is known as hybridization of atomic orbitals [20]. Hybridized orbitals are constructed from linear combinations of atomic orbitals, the later serving as basis functions to the former. The superposition of these hybridized orbitals with neighboring atoms gives rise to different types of chemical bonding, depending on the hybridization of the central atom.

Recalling that the orbitals are a first approximation (ignoring electron-electron repulsion) to the problem of electrons in a Coulomb potential of a nucleus with charge Ze, they correspond to one-particle hydrogenic states $\psi_{n,l,m}$ characterized by the quantum numbers n, l and m [21]. Accordingly, they can be decomposed in a product between a radial component $R_{n,l}(r)$ given by

the Laguerre polynomials, and an angular component $Y_{l,m}(\theta,\phi)$ corresponding to the spherical harmonics, on the form

$$\psi_{n,l,m} = R_{n,l}(r)Y_{l,m}(\theta,\phi). \tag{1.1}$$

Since chemical bonding involves only valence electrons, we are concerned with the $\psi_{2,l,m}$ states. The radial components of the $2s$ and $2p$ wave functions are equal in magnitude, and may be omitted at this point [22]. The angular components of the atomic orbitals s and p_i ($i = x, y, z$) are given, respectively, as:

$$\begin{aligned} \text{s}: &\qquad Y_{0,0}(\theta,\phi) = \frac{1}{\sqrt{4\pi}} \\ p_z: &\qquad Y_{1,0}(\theta,\phi) = i\sqrt{\frac{1}{4\pi}}\cos\theta \\ p_{x,y}: &\qquad Y_{1,\pm1}(\theta,\phi) = \mp i\sqrt{\frac{3}{8\pi}}\sin\theta e^{\pm\phi}. \end{aligned} \tag{1.2}$$

The formation of covalent bonds in molecules or solids generates a drop on the total energy due to the overlap of the electron wave functions, giving rise to the molecular orbitals, in case of molecules, or electronic bands, in case of solids. In this case, the extra energy can be sufficient to promote a $2s$ electron into a $2p$ orbital, (this energy being approximately 4.2 eV for carbon atoms). However, the necessary extra energy is only achieved if the overlap of the wave functions between neighboring atoms is maximal. Such a condition is satisfied when the relative position between the central and neighboring atoms assume those directions for which the atomic wave functions take on maximal values. These values can be achieved through the process of hybridization and the larger they are, the stronger the bond is.

In order to construct the hybridized states, we need to choose a set of basis functions. Rather than taking the $\psi_{l,m}(\theta,\phi)$, it is more convenient to choose their orthonormalized linear combinations:

$$\begin{aligned} i\sqrt{2\pi}[\psi_{1,1}(\theta,\phi) - \psi_{1,-1}(\theta,\phi)] &= \sqrt{3}\sin\theta\cos\phi \\ i\sqrt{2\pi}[\psi_{1,1}(\theta,\phi) + \psi_{1,-1}(\theta,\phi)] &= \sqrt{3}\sin\theta\sin\phi \\ -i\sqrt{4\pi}\psi_{1,0}(\theta,\phi) &= \sqrt{3}\cos\theta, \end{aligned} \tag{1.3}$$

and therefore, the basis functions can be represented as

$$\begin{aligned} |2s\rangle &= 1 \\ |x\rangle = \sqrt{3}\sin\theta\cos\phi, \quad |y\rangle &= \sqrt{3}\sin\theta\sin\phi, \quad |z\rangle = \sqrt{3}\cos\theta. \end{aligned} \tag{1.4}$$

Finally, the hybridized orbital can then be constructed as

$$\psi(\theta,\phi) = a + \sqrt{3}(b\sin\theta\cos\phi + c\sin\theta\sin\phi + d\cos\theta) \tag{1.5}$$

or in Dirac's notation

$$|\psi\rangle = a\,|s\rangle + b\,|x\rangle + c\,|y\rangle + d\,|z\rangle\,, \tag{1.6}$$

with $|s\rangle$, $|x\rangle$, $|y\rangle$, and $|z\rangle$ defined in (1.4). We now look for a set of real numbers (a,b,c,d) that will maximizes the norm of $|\psi\rangle$. In other words, we must find the directions for which ψ assumes its maximum value (ψ_{max}). Since $|\psi\rangle$ is the angular component of the total wave function, it must be normalized

$$\begin{aligned} \langle\psi\,|\,\psi\rangle \equiv \int |\,\langle\psi\,|\,\psi\rangle^2|d\Omega &= 4\pi \\ &= a^2\,\langle s\,|\,s\rangle + b^2\,\langle x\,|\,x\rangle + c^2\,\langle y\,|\,y\rangle + d^2\,\langle z\,|\,z\rangle \end{aligned} \tag{1.7}$$

with $d\Omega$ being the differential solid angle element. It follows that, to satisfy the normalization condition 1.7, we must have

$$a^2 + b^2 + c^2 + d^2 = 1 \tag{1.8}$$

We thus need to maximize the function $\psi(\theta,\phi)$ with the restriction given from equation 1.8 . This can be solved by the method of Lagrange Multipliers. For that, we must solve the set of equations

$$\nabla\psi = \lambda\nabla g, \tag{1.9}$$

with λ being the Lagrange multiplier, and g the restriction

$$g = a^2 + b^2 + c^2 + d^2 - 1. \tag{1.10}$$

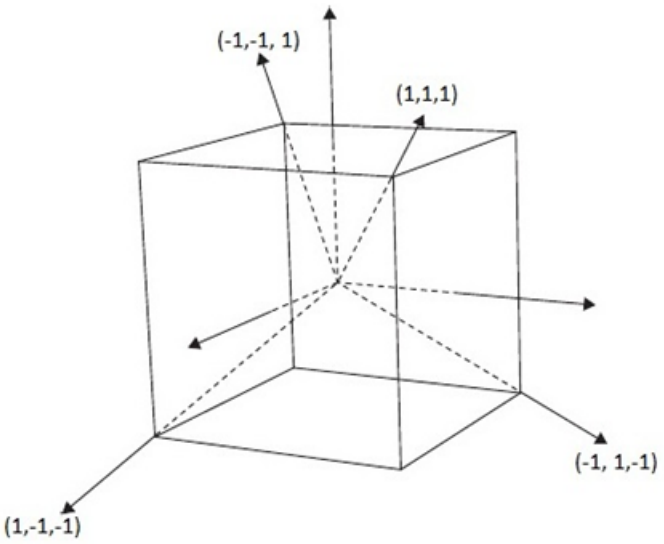

Figure 1.1: Coordinate system for finding directions of maximum value for hybridized wave functions of a carbon atom. The carbon atom is placed at the origin coinciding with the center of a side two cube. Figure adapted from [22].

Let us place the origin, and the central carbon atom as well, at the center of a cube of side 2 and coordinate axes parallel to its edges. We are going to assume that, for a specific $|\psi\rangle$, ψ_{max} is reached along the diagonal direction of the cube $(1, 1, 1)$, (see Fig. 1.1). Thus we need to find (a, b, c, d) for that specific $|\psi\rangle$. Along the $(1, 1, 1)$ direction, we have

$$\sin\phi = \cos\phi = \frac{1}{\sqrt{2}}, \quad \cos\theta = \frac{1}{\sqrt{3}}, \quad \sin\theta = \sqrt{\frac{2}{3}}, \tag{1.11}$$

so that

$$|x\rangle = 1, |y\rangle = 1, |z\rangle = 1. \tag{1.12}$$

It follows that, by considering the conditions (1.10) and (1.12), Eq. 1.9 can be solved to

$$a = b = c = d. \tag{1.13}$$

Next, (1.13) combined to (1.10) gives

$$a = \frac{1}{2}. \tag{1.14}$$

Thus substitution of (1.14) into (1.6) determines the first orbital

$$|sp_1^3\rangle = \frac{1}{2}(|s\rangle + |x\rangle + |y\rangle + |z\rangle), \tag{1.15}$$

for which ψ assumes the maximum value ψ_{max}. Next, we need to find a set of three orthonormal orbitals orthogonal to $|sp_1^3\rangle$. In other words, we need to find a basis that spans the three dimensional subspace orthogonal to $|sp_1^3\rangle$. Let us assume that these orbitals have the form

$$|sp_i^3\rangle = \alpha\,|s\rangle + \beta\,|x\rangle + \gamma\,|y\rangle + \delta\,|z\rangle\,. \tag{1.16}$$

The orthogonality with $|sp_1^3\rangle$ implies

$$\langle sp_i^3|sp_1^3\rangle = 0 \rightarrow \alpha + \beta + \gamma + \delta = 0. \tag{1.17}$$

Equation 1.17, combined with the normalization condition, gives the necessary ingredients for the determination of the three orbitals. Since they are not uniquely determined, one possible solution is on the form

$$\begin{aligned} |sp_2^3\rangle &= \frac{1}{2}(|s\rangle + |x\rangle - |y\rangle - |z\rangle) \\ |sp_3^3\rangle &= \frac{1}{2}(|s\rangle - |x\rangle + |y\rangle - |z\rangle) \\ |sp_4^3\rangle &= \frac{1}{2}(|s\rangle - |x\rangle - |y\rangle + |z\rangle). \end{aligned} \tag{1.18}$$

The norms of the wavefunctions $|sp_i^3\rangle$ $(i = 1, 2, 3, 4)$ take their maximum values along the (1,1,1),(1,-1,-1),(-1,1,-1) and (-1,-1,1) directions, coinciding with the vertices of a tetrahedron. Therefore, the maximum overlap of the wave functions, leading to the maximum gain in chemical-bonding energy of a central carbon atom with four neighboring atoms corresponds to a tetrahedral geometry. This qualitative analysis explains the shape of the methane molecule, as well as the symmetry of the diamond solid. The wavefunctions described in Eq. 1.18 corresponds to

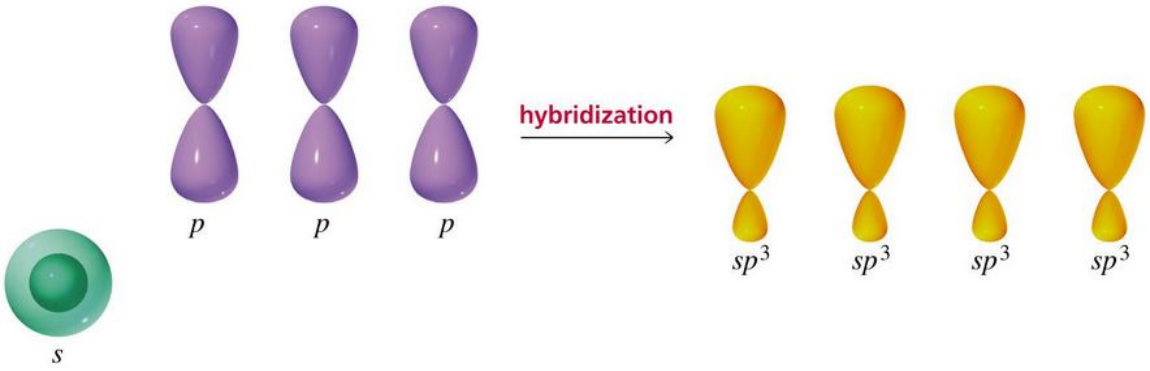

Figure 1.2: Illustration of the process of sp^3 hybridization. A s orbital combines with three p orbitals, resulting in four hybridized sp^3 orbitals. Figure taken from [23].

the angular component of the so-called sp^3 orbitals of the carbon atom. In this configuration, the $1s$ orbital combines with three p orbitals resulting in four hydridized orbitals, as illustrated in Fig. 1.2.

Another option is to take the linear combination of a $2s$ orbital with two $2p$ orbitals, for example $2p_x$ and $2p_y$, whereas the remaining p orbital, p_z in this case, remains unchanged. This configuration of the carbon atom is called sp^2 hybridization and can be achieved if one repeats the aforementioned procedure for a smaller basis including only functions $|s\rangle$, $|x\rangle$ and $|y\rangle$. The calculations are straightforward and will not be reproduced here. The result is

$$\begin{aligned} |sp_1^2\rangle &= \frac{1}{\sqrt{3}}|s\rangle + \sqrt{2}|x\rangle \\ |sp_2^2\rangle &= \frac{1}{\sqrt{3}}|s\rangle - \frac{1}{\sqrt{6}}|x\rangle + \frac{1}{\sqrt{2}}|y\rangle) \\ |sp_3^2\rangle &= \frac{1}{\sqrt{3}}|s\rangle - \frac{1}{\sqrt{6}}|x\rangle - \frac{1}{\sqrt{2}}|y\rangle). \end{aligned} \tag{1.19}$$

The corresponding orbitals have their maxima in the $x-y$ plane along the directions intercepting the vertex of an equilateral triangle, as depicted in Fig.1.3. If neighboring atoms are positioned in such directions, it will lead to a maximum overlap of the wave functions, and the resultant bonds are called σ bonds. The overlap of neighboring p_z orbitals forms π bonds. Carbon atoms in graphene and graphite lattice are sp^2 hybridized.

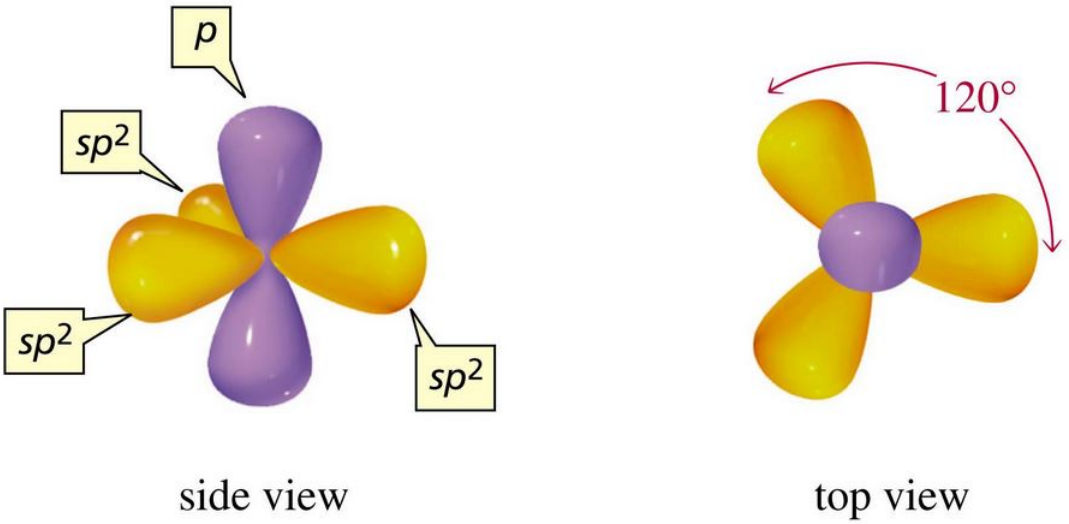

Figure 1.3: Illustration of the sp^2 hybridized orbitals. The sp^2 orbitals lie in the x-y plane forming angles of 120° to each other while the p_z orbital lies in the z axis. The sp^2 orbitals are responsible for the formation of σ bonds, while the p_z orbitals are responsible for formation of the π bonds. Figure taken from [23].

1.2 Electronic structure of graphene: the tight binding method

In Sec.1.1 we linearly combined atomic orbitals of a carbon atom in order to obtain new hybridized atomic orbitals. In this section we are going to somewhat extend this procedure for a crystal, and the method we will employ is called the tight binding. In this method, the wave function of the crystal is constructed by a linear combination of the atomic orbitals of its constituents, with the coefficients of the expansion given by the Bloch Theorem. The tight binding method is one of the simplest methods for calculating electronic structures of solids and it is of great practical utility.

In order to determine the electronic structure of graphene using this method, the first step is to specify the unit cell and the unit vectors $\vec{a_i}$ $(i = 1, 2)$ of the crystal lattice. In graphene, the carbon atoms are disposed in a hexagonal lattice as show in Fig. 1.4 (a). The graphene Bravais lattice is triangular , and the lattice vectors are given [in the x,y basis defined in Fig.1.4 (a)] as

$$\vec{a_1} = \frac{a}{2}(\sqrt{3}, 1), \quad \vec{a_2} = \frac{a}{2}(\sqrt{3}, -1), \tag{1.20}$$

where $a = |\vec{a_1}| = |\vec{a_2}| = \sqrt{3}a_{c-c} = 2.46$ Å is the lattice parameter of graphene, a_{c-c} being the nearest neighbor distance ($a_{c-c} = 1.42$Å). The unit cell contains two atoms, each of them belonging to a distinct sublattice, A or B. In this configuration, each atom belonging to the A sublattice is surrounded by three atoms belonging to the B sublattice, and vice-versa.

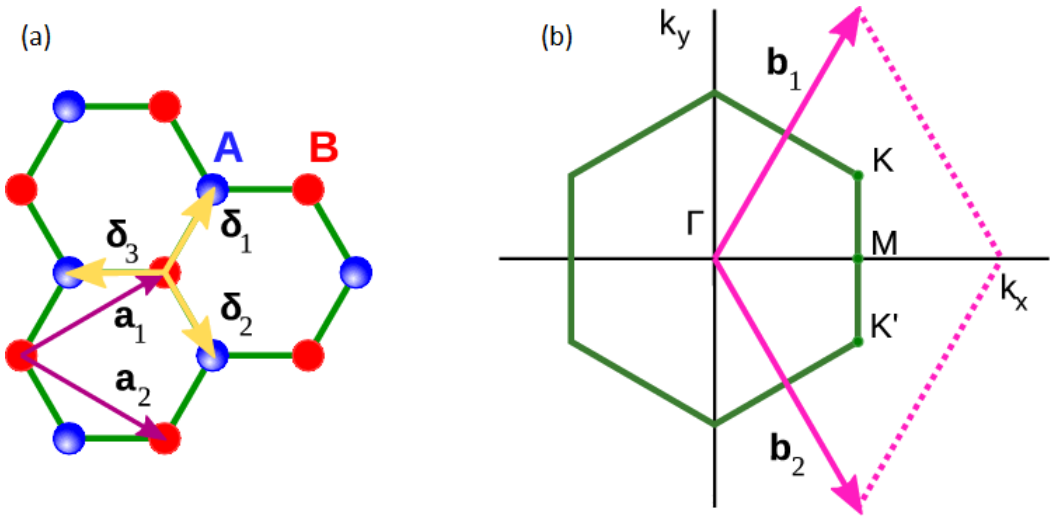

Figure 1.4: In (a): direct lattice with primitive vectors $\vec{a_i}$ and first neighbours $\vec{\delta_i}$. In (b): reciprocal lattice with high symmetry points Γ, K and M. Figures taken from [24].

The next step is to specify the Brillouin zone and the reciprocal lattice vectors, $\vec{b_i}$ $(i = 1, 2)$, followed by the selection of high symmetry points and lines. For a two dimensional crystal, the reciprocal lattice vectors can be determined by

$$\vec{b_i} = \frac{2\pi(\hat{n} \times \vec{a_j})}{\hat{n} \cdot (\vec{a_j} \times \vec{a_i})}, \quad (i, j = 1, 2) \tag{1.21}$$

where $\hat{n}$ is the vector normal to the plane containing the vectors $\vec{a_1}$ and $\vec{a_2}$. The reciprocal lattice is also triangular, with lattice vectors:

$$\vec{b_1} = \frac{2\pi}{a}(\frac{1}{\sqrt{3}}, 1), \quad \vec{b_2} = \frac{2\pi}{a}(\frac{1}{\sqrt{3}}, -1), \tag{1.22}$$

corresponding to a lattice constant of $4\pi/\sqrt{3}a$. The Brillouin zone is represented by the hexagon in Fig. 1.4 (b). The three high symmetry points Γ, K and M are indicated, corresponding to the center, the corner and the center of the edge respectively. Their coordinates are:

$$\Gamma = (0, 0), \quad K = \frac{2\pi}{a}(\frac{1}{\sqrt{3}}, \frac{1}{3}), \quad M = (\frac{2\pi}{\sqrt{3}a}, 0). \tag{1.23}$$

The π electrons are the valence electrons which are the relevant ones for the transport properties; therefore we are going to perform the tight binding calculation considering only the $2p_z$ orbitals. We start by constructing a tight binding Bloch function $\phi_i(\vec{k}, \vec{r})$, which is given by

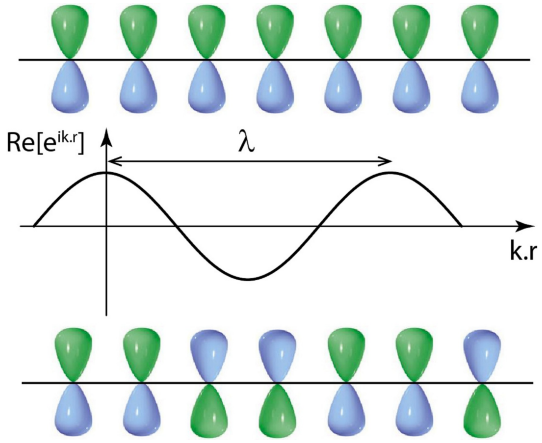

Figure 1.5: Representation of the Bloch orbitals in a 1D lattice. The top shows the p_z wavefunctions (actually its square modulus) of individual carbon atoms, the middle shows (the real part) of the phase $e^{i\vec{k}\cdot\vec{r}}$ of of the Bloch orbitals and the bottom shows the amplitude of the Bloch orbitals.

$$\phi_i(\vec{k},\vec{r}) = \frac{1}{\sqrt{N}}\sum_{\vec{R}} e^{i\vec{k}\cdot\vec{r}}\phi_i(\vec{r}-\vec{R}), \qquad (i=1,...,n), \tag{1.24}$$

where $\vec{R}$ is the position of the atom, ϕ_i denotes the atomic wave function index by i and n is the number of the wavefunctions in the unit cell. The function $\phi_i(\vec{r}-\vec{R})$ represents an atomic wave function centered at position $\vec{R}$ in the lattice. As all lattice vectors are being swept by the index $\vec{R}$ in the summation, the total wave function $\phi_i(\vec{k},\vec{r})$ will be a linear combination of all atomic wave functions of the crystal. These functions are weighted by the factor $e^{i\vec{k}\cdot\vec{r}}$, which modulates the crystal wavefunction as pictured in Fig. 1.5 for a $1D$ lattice. In case of π electrons in graphene there are two wavefunctions in the unit cell, namely the two $2p_z$ orbitals, associated with the two inequivalent carbon atoms A and B. Thus, there will be two functions, ϕ_A and ϕ_B, which are formed by combining $2p_z$ orbitals between A and B atoms respectively. Let us place the origin of our x, y coordinate system in atom A, as illustrated in Fig. 1.4 (a). In this case, we have

$$\phi_A(\vec{k},\vec{R}) = \frac{1}{\sqrt{N}}\sum_{\vec{R}} e^{i\vec{k}\cdot\vec{r}}\phi_A(\vec{r}-\vec{R}), \qquad \vec{R} = n_1\vec{a_1} + n_2\vec{a_2}, \tag{1.25}$$

where $\vec{a_1}$ and $\vec{a_2}$ are the primitive vectors defined in (1.20). To construct ϕ_B we use the same coordinate system, choosing a vector $\vec{B}$ that connects A atoms to B atoms. The aid of this vector is necessary because when the summation is performed over $\vec{R}$, with the origin placed at an A

atom, only the orbitals of A atoms are summed. The trick of introducing the $-\vec{B}$ vector in the argument of the wavefunction during the summation, changes the summation over A atoms to the summation over their nearest neighbors B atoms.

$$\phi_B(\vec{k},\vec{R}) = \frac{1}{\sqrt{N}}\sum_{\vec{R}} e^{i\vec{k}\cdot\vec{r}}\phi_B(\vec{r}-\vec{B}-\vec{R}), \qquad \vec{B} = \left(\frac{2a}{\sqrt{3}}, 0\right) \tag{1.26}$$

To obtain the one-electron energy eigenvalues $E_i(\vec{k})$ the secular equation must be solved [20]

$$|\mathbf{H} - \mathrm{E}\mathbf{S}| = \mathbf{0}. \tag{1.27}$$

The **H** and **S** matrices are the transfer integral matrix and the overlap integral matrix, respectively, whose matrix elements are defined as are defined as

$$H_{ij}(\vec{k}) = \langle\phi_i|H|\phi_j\rangle\,,\ S_{ij}(\vec{k}) = \langle\phi_i|\phi_j\rangle\,, \qquad (i,j=1,...,n). \tag{1.28}$$

Thus, both **H** and **S** are $n\times n$ matrices and the solution to Eq. 1.27 gives all n eigenvalues $E_i(\vec{k})$. The (2×2) transfer integral matrix is obtained by substituting Eq. (1.24) into Eq. (1.28). We are going to first calculate the diagonal terms,

$$\begin{aligned} H_{AA} = \langle\phi_A|H|\phi_A\rangle &= \frac{1}{N}\sum_{\vec{R},\vec{R'}} e^{i\vec{k}\cdot(\vec{R}-\vec{R'})}\,\langle\phi_A(\vec{r}-\vec{R'})|H|\phi_A(\vec{r}-\vec{R})\rangle \\ &= \frac{1}{N}\sum_{\vec{R}=\vec{R'}} \langle\phi_A(\vec{r}-\vec{R'})|H|\phi_A(\vec{r}-\vec{R})\rangle \\ &+ \frac{1}{N}\sum_{\vec{R}=\vec{R'}\pm\vec{a_i}} e^{\pm i\vec{k}\cdot\vec{a_i}}\,\langle\phi_A(\vec{r}-\vec{R'})|H|\phi_A(\vec{r}-\vec{R})\rangle \\ &+ (\text{terms in which } \vec{R}-\vec{R'} \geqslant 2\vec{a_i}). \end{aligned} \tag{1.29}$$

The maximum contribution to H_{AA} comes from $\vec{R} = \vec{R'}$, therefore we are going to neglect the other terms for simplicity. The crystal Hamiltonian in one electron approximation can be written as

$$
\begin{aligned}
&H(\vec{r}) = -\frac{\hbar}{2m}\nabla^2 + \sum_i U_{atomic,i}(\vec{r}) + \Delta U_i(\vec{r}) \quad i = A, B \text{ where} \\
&U_{atomic,A}(\vec{r}) = U_{atomic,A}(\vec{r} + \vec{R});\ \Delta U_A(\vec{r}) = \Delta U_A(\vec{r} + \vec{R}) \\
&U_{atomic,B}(\vec{r}) = U_{atomic,B}(\vec{r} + \vec{B} + \vec{R});\ \Delta U_B(\vec{r}) = \Delta U_B(\vec{r} + \vec{B} + \vec{R}).
\end{aligned} \tag{1.30}
$$

The functions $U_{atomic,i}$ and $\Delta U_i(\vec{r})$ are the potential energy functions associated with the interaction between the electron and the carbon atoms (A and B), and the correction to that energy at that position, respectively. The ΔU_i term contains all corrections to the atomic potential to reproduce the full periodic potential of the crystal. The functions $\phi_i(\vec{k}, \vec{r})$ are well localized at the atomic positions, with its amplitude being very small when $\vec{r}$ exceeds a distance of the order of the lattice constant. Therefore the first term of Eq. 1.29 yields:

$$
\begin{aligned}
&\frac{1}{N}\sum_{\vec{R}=\vec{R'}} \langle \phi_A(\vec{r} - \vec{R'})|H|\phi_A(\vec{r} - \vec{R})\rangle = \\
&\frac{1}{N}\sum_{\vec{R}=\vec{R'}} \int \phi_A(\vec{r} - \vec{R'})H\phi_A(\vec{r} - \vec{R})d\vec{r} = \varepsilon^*_{2p_z}
\end{aligned} \tag{1.31}
$$

where each integral has only an appreciable value on the vicinity of each atom. Note that $\varepsilon^*_{2p_z}$ is not simply the electron energy for the free carbon atom, because the Hamiltonian contains the ΔU_i terms. We can use the same approximations to get that $H_{BB} = \varepsilon^*_{2p_z}$. For the off-diagonal matrix elements we are going to consider only the three nearest neighbor B atoms relative to an A atom. The relative positions between the central atom A and the three nearest neighbors B are denoted by $\vec{\delta}_1$, $\vec{\delta}_2$, and $\vec{\delta}_3$. Following these definitions, the off-diagonal matrix elements H_{AB} are evaluated as

$$
\begin{aligned}
H_{AB} &= \langle \phi_A|H|\phi_B\rangle \\
&= \frac{1}{N}\sum_{\vec{R},\vec{R'}} e^{i\vec{k}\cdot(\vec{R}-\vec{R'})} \langle \phi_A(\vec{r} - \vec{R'})|H|\phi_B(\vec{r} - \vec{B} - \vec{R})\rangle \\
&= \frac{1}{N}\sum_{\vec{R}=\vec{R'}\pm\vec{\delta}_i} e^{i\vec{k}\cdot\vec{R}_i} \langle \phi_A(\vec{r} - \vec{R'})|H|\phi_B(\vec{r} - \vec{R})\rangle, \quad i = 1, 2, 3 \\
&= \gamma(e^{i\vec{k}\cdot\vec{\delta_1}} + e^{i\vec{k}\cdot\vec{\delta_2}} + e^{i\vec{k}\cdot\vec{\delta_3}}) = \gamma f(\vec{k}).
\end{aligned} \tag{1.32}
$$

where γ is the nearest neighbor transfer integral. In the graphene case, γ has the form

$$
\gamma = \langle \phi_A(\vec{r} - \vec{R'})|H|\phi_B(\vec{r} - \vec{R} + \vec{\delta}_i)\rangle\,, \quad i = 1, 2, 3. \tag{1.33}
$$

Substituting the relative coordinates of the nearest neighbors ($\vec{\delta}_1$, $\vec{\delta}_2$, and $\vec{\delta}_3$), $f(\vec{k})$ is evaluated to

$$f(\vec{k}) = e^{ik_x \frac{a}{\sqrt{3}}} + 2e^{-ik_x \frac{a}{2\sqrt{3}}} \cos \frac{k_y a}{\sqrt{3}}. \tag{1.34}$$

Since **H** is Hermitian ($H = H^{\dagger}$), we have $H_{BA} = {H_{AB}}^*$, where the symbol $*$ stands for the complex conjugate. To calculate the overlap integral matrix **S**, we use the fact that $S_{AA} = S_{BB} = 1$, assuming that $|\phi_A\rangle$ and $|\phi_B\rangle$ are normalized. To calculate the off-diagonal elements of **S** we can repeat the same method used to obtain H_{ij}. In this case, we have $S_{AB} = sf(\vec{k}) = {S_{BA}}^*$ with

$$s = \langle \phi_A(\vec{r} - \vec{R}) | \phi_B(\vec{r} - \vec{R} + \vec{\delta_i}) \rangle \,, \quad (i = 1, 2, 3). \tag{1.35}$$

The final form of the matrices **H** and **S** are

$$\mathbf{H} = \begin{pmatrix} \varepsilon^*_{2p_z} & \gamma f(\vec{k}) \\ \gamma f(\vec{k}) & \varepsilon^*_{2p_z} \end{pmatrix}, \quad \mathbf{S} = \begin{pmatrix} 1 & sf(\vec{k}) \\ sf(\vec{k}) & 1 \end{pmatrix}. \tag{1.36}$$

Solving the Secular Equation (1.27), with **H** and **S** being given by Eq. 1.36, the eigeinvalues $E(\vec{k})$ are obtained as a function of $\vec{k} = (\vec{k_x}, \vec{k_y})$

$$E(\vec{k_x}, \vec{k_y}) = \frac{\varepsilon^*_{2p_z} \pm \gamma w(\vec{k})}{1 \mp s w(\vec{k})}, \tag{1.37}$$

with the function $w(\vec{k})$ given by:

$$w(\vec{k}) = |f(\vec{k})|^2 = \sqrt{1 + 4cos\frac{\sqrt{3}k_x a}{2} \cos \frac{k_y a}{2} + 4 \cos^2 \frac{k_y a}{2}}. \tag{1.38}$$

The solution with + signs in the numerator and − sign in the denominator gives the π bonding energy band, while the other solution gives the π^* anti-bonding energy band. A plot of the energy dispersion relation throughout the first Brillouin zone of graphene is displayed in Fig. 1.6 (b). Figure 1.6 (c) shows the energy dispersion relations along the high symmetry axes along the perimeter of the triangle ΓKM. The tight binding method is not sufficient to completely determine electronic structures of crystals because the parameters $\varepsilon^*_{2p_z}$, γ and s need to be determined either from first principle calculations or experimentally. Here we use the parameters $\varepsilon^*_{2p_z} = 0$ eV,$\gamma = -3.033$ eV and $s = 0.129$ [20].

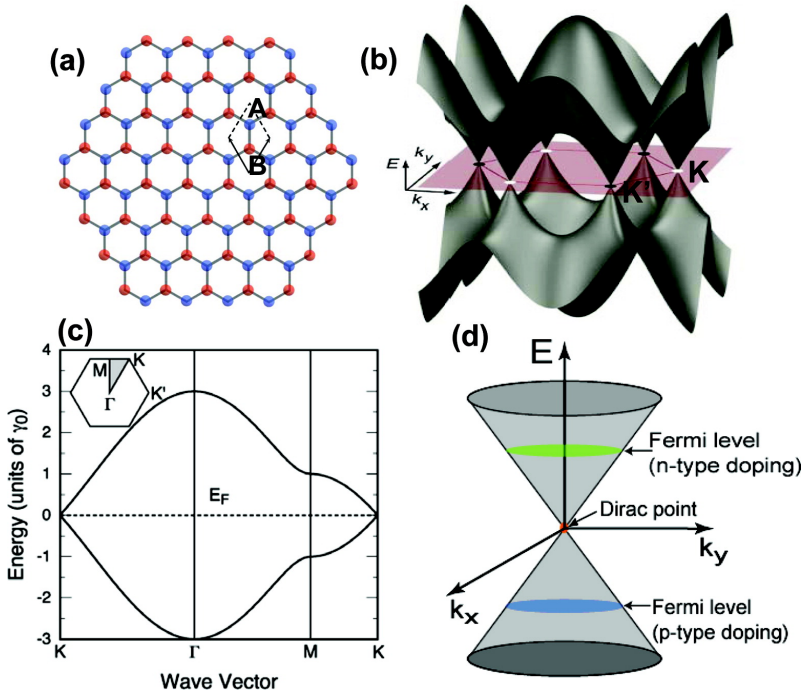

Figure 1.6: (a) Graphene lattice in real space. (b) The energy dispersion plot of π electrons in graphene over the first Brillouin Zone. (c) The energy dispersion along the high symmetry directions along the ΓKM trajectory. (d) The Dirac Cone near the $K(K^{'})$ points. Figure taken from [25].

Since there are two π electrons per unit cell, for undoped graphene the lower π band is completely occupied. The upper π^* and the lower π bands touch each other at the K points, through which the Fermi energy passes. The density of states at the Fermi level is zero, therefore graphene is a zero-gap semiconductor. This comes from the symmetry requirement that the two carbon atoms at sites A and B are equivalent to each other. If the A and B sites had different atoms such as B and N, which is the case for boron nitride, the site energy $\varepsilon^*_{2p_z}$ would be different for B and N, and therefore the calculated energy dispersion would show an energy gap between π and π^* bands [20]. The energy dispersion close to the K point is exhibited in Fig. 1.6 (d). Note that the energy dispersion around this point takes the form of a cone, called the Dirac Cone. The linear dispersion of the π electrons around the K point is the responsible for the remarkable optical and transport properties of graphene.

1.3 Vibration modes in Graphene

In Sec. 1.2 we described the electronic structure of graphene. In this section we are going to study the dynamics of the graphene lattice within the harmonic approximation. We will use

a force-constant model to obtain the eigenfrequencies $\omega(\vec{k})$ of the normal modes, where $\vec{k}$ is in the first Brillouin Zone. As a result, we will obtain the phonon dispersion relation of $\omega(\vec{k})$ along high symmetry directions of the *BZ*. The concept of phonon is associated with quantum mechanics and will be explained at the end of this section. Until that point, our approach lies completely within classical theory, with all "quantumness" hidden in the spring constants.

1.3.1 Dynamical matrix

The equilibrium position of the i^{th} atom in a lattice is given by the lattice vector $\vec{R}_i$, while its instantaneous position of it is represented by $\vec{R'}_i$. We start by writing the Lagrangian in the harmonic approximation:

$$\mathscr{L} = \frac{1}{2}\sum_i m_i\left|\dot{\vec{R'}}_i\right|^2 - \frac{1}{4}\sum_{i,j}\mathbb{K}^{(ij)}\left|\vec{R'}_i - \vec{R'}_j - \Delta\vec{R}_{ij}\right|^2, \Delta\vec{R}_{ij} = \vec{R}_i - \vec{R}_j. \tag{1.39}$$

Here m_i is the mass of the i^{th} atom and $\mathbb{K}^{(ij)}$ is the force constant tensor between the i^{th} and j^{th} atoms, which is represented by a 3×3 matrix. The sum over j is taken, in principle, over all neighbors of the i^{th} atom in the lattice.

It is useful to define the relative displacement of the i^{th} atom $\vec{u}\left(\vec{R}_i\right)$ or, in a more condensed notation, $\vec{u}_i = \vec{R'}_i - \vec{R}_i$. Using this notation we have

$$\begin{gathered}\vec{R'}_i - \vec{R'}_j = \vec{u}_i - \vec{u}_j + \left(\vec{R}_i - \vec{R}_j\right) = \vec{u}_i - \vec{u}_j + \Delta\vec{R}_{ij} \\ \text{and} \qquad \dot{\vec{R'}}_i = \dot{\vec{u}}_i.\end{gathered} \tag{1.40}$$

By substituting 1.40 intto 1.39 we get the Lagrangian expressed in terms of the relative displacements on the form

$$\mathscr{L} = \frac{1}{2}\sum_i m_i\left|\dot{\vec{u}}_i\right|^2 - \frac{1}{4}\sum_{i,j}\mathbb{K}^{(ij)}\left|\vec{u}_i - \vec{u}_j\right|^2. \tag{1.41}$$

From the Euler-Lagrange equation, we obtain the equation of motion for the displacement of the i^{th} coordinate

$$m_i\ddot{\vec{u}}_i = \sum_j \mathbb{K}^{(ij)}\left(\vec{u}_j - \vec{u}_i\right) \qquad (i = 1, ...n), \tag{1.42}$$

where n is the number of atoms in the unit cel. The sum over j is usually taken over only a few neighbor distances relative to the i^{th} site, which for graphene has been carried out up to the 4th nearest-neighbor interactions [20].

A travelling wave is one solution to Eq. 1.42, thus a more general solution can be chosen by representing $\vec{u}_i$ as a superposition of traveling waves with polarization $\vec{u}_k$. In other words, we can perform a Fourier transform of the displacement of the i^{th} atom with the wave number $\vec{k}$ to obtain the normal mode displacements $\vec{u}^{(i)}_{\vec{k}}$

$$\vec{u}_i = \frac{1}{\sqrt{N}}\sum_{\vec{k}} e^{-i\left(\vec{k}\cdot\vec{R}_i - \omega t\right)}\vec{u}^{(i)}_{\vec{k}} \quad \text{or} \quad \vec{u}^{(i)}_{\vec{k}} = \frac{1}{\sqrt{N}}\sum_{\vec{R}_i} e^{i\left(\vec{k}'\cdot\vec{R}_i - \omega t\right)}\vec{u}_i, \tag{1.43}$$

where the sum is taken over all N wave vectors $\vec{k}$ in the first Brillouin zone, with N being the number of unit cells in the solid. The crucial point is to understand that the travelling wave 1.43 is not simply a mathematical solution to the differential equation 1.42, but it actually represents a collective motion of all atoms in the lattice. This can be clearly seen in Fig. 1.7 , which represents a normal mode associated with a travelling wave with wave vector k. If one fix their attention to a single position $\vec{R}_i$, the displacement of the atom at that position $\vec{u}_i$, describes an harmonic motion as the wave passes trough it. Now if one pay attention to different positions in the lattice, what will be seeing is that each atom is moving up and down performing an harmonic oscillation, although the overall result is a collective motion, along the horizontal direction in this case, consisting of a normal mode.

Taking the second derivative of $\vec{u}_i$ in Eq. 1.43, and assuming the same eigenfrequencies ω for all $\vec{u}_i$, we have $\ddot{\vec{u}}_i = -\omega^2\vec{u}_i$. The substitution of this relation in Eq. 1.42 yelds

$$\left(\sum_j \mathbb{K}^{(ij)} - m_i\omega^2(\vec{k})\right)\sum_{\vec{k}} e^{-i\vec{k}\cdot\vec{R}_i}u^{(i)}_{\vec{k}} = \sum_j \mathbb{K}^{(ij)}\sum_k e^{-i\vec{k}\cdot\vec{R}_j}\vec{u}^{(j)}_{\vec{k}}. \tag{1.44}$$

Next, if we multiply both sides of Eq. 1.44 by $e^{i\vec{k}'\cdot\vec{R}_i}$, and perform a summation on $\vec{R}_i$, we get

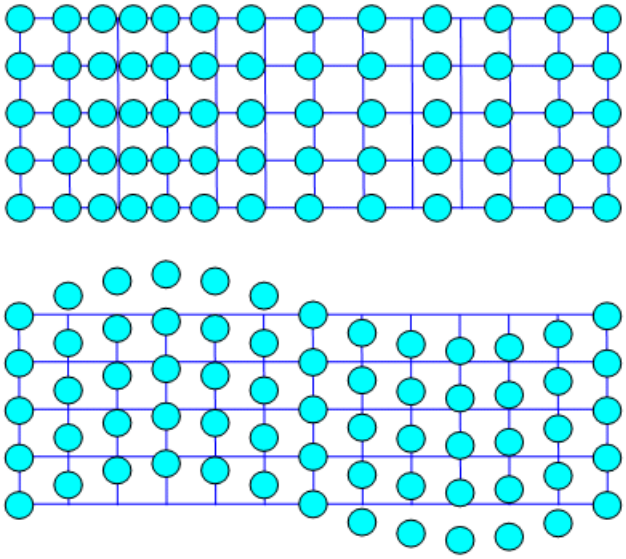

Figure 1.7: Normal mode associated with a travelling wave.

$$\left(\sum_j \mathbb{K}^{(ij)} - m_i\omega^2(\vec{k})\right)\sum_{\vec{k}}\sum_{\vec{R}_i} e^{i\left(\vec{k'}-\vec{k}\right)\cdot\vec{R}_i} u_{\vec{k}}^{(i)} = \sum_j \mathbb{K}^{(ij)} \sum_k \sum_{\vec{R}_i} e^{i\left(\vec{k'}-\vec{k}\right)\cdot\vec{R}_i} e^{i\vec{k}\cdot\left(\vec{R}_i-\vec{R}_j\right)} \vec{u}_{\vec{k}}^{(j)}. \tag{1.45}$$

Now we use the orthogonality condition in the continuum $\vec{k}$ space [20]

$$\sum_{\vec{R}_i} e^{i\left(\vec{k'}-\vec{k}\right)\cdot\vec{R}_i} = N\delta_{\vec{k'}\vec{k}}, \tag{1.46}$$

to have

$$\left(\sum_j \mathbb{K}^{(ij)} - m_i\omega^2(\vec{k})\mathbb{I}\right) u_{\vec{k}}^{(i)} - \sum_j \mathbb{K}^{(ij)} e^{\vec{k}\cdot\Delta R_{ij}} u_{\vec{k}}^{(j)} = 0, \qquad (i = 1, .., n), \tag{1.47}$$

where $\mathbb{I}$ is the 3×3 identity matrix. Remember that our unit cell has n atoms. Let us develop Eq. 1.47 for the atom $i = 1$:

$$\left(\sum_j \mathbb{K}^{(1j)} - m_1\omega^2(\vec{k})\mathbb{I}\right)u_{\vec{k}}^{(1)} - \left(\mathbb{K}^{(11)}e^0 u_{\vec{k}}^{(1)} + \mathbb{K}^{(11')}e^{\vec{k}\cdot\Delta R_{11'}}u_{\vec{k}}^{(1')} + ...\right)$$
$$- \left(\mathbb{K}^{(12)}e^{\vec{k}\cdot\Delta R_{12}}u_{\vec{k}}^{(2)} + \mathbb{K}^{(12')}e^{\vec{k}\cdot\Delta R_{12'}}u_{\vec{k}}^{(2')} + ...\right) + ... - \left(\mathbb{K}^{(1n)}e^{\vec{k}\cdot\Delta R_{1n}}u_{\vec{k}}^{(n)}\right. \tag{1.48}$$
$$\left. + \mathbb{K}^{(1n')}e^{\vec{k}\cdot\Delta R_{1n'}}u_{\vec{k}}^{(n')} + ...\right)$$

The summation inside each parenthesis is taken for equivalent atoms. It means that the coordinates $\vec{R}_1$ and $\vec{R}_{1'}$ differ only by a lattice vector. In fact, because the j and j' sites are equivalent to each other, we can show that $u_{\vec{k}}^{j}$ is equal to $u_{\vec{k}}^{j'}$. To prove this we go back to the definition of $u_{\vec{k}}^{j}$ in Eq. 1.43:

$$\begin{aligned}
\vec{u}_{\vec{k}}^{(j')} &= \frac{1}{\sqrt{N}}\sum_{\vec{R}_{j'}} e^{i\left(\vec{k}\cdot\vec{R}_{j'}-\omega t\right)}\vec{u}_{j'}, \quad \vec{R}_j - \vec{R}_{j'} = \sum_{i=1}^{3} n_i\vec{a}_i \\
&= \frac{1}{\sqrt{N}}\sum_{\vec{R}_j-\sum n_i\vec{a}_i} e^{i\left(\vec{k}\cdot\vec{R}_j-\omega t\right)}\vec{u}_{\left(\vec{R}_j-\sum n_i\vec{a}_i\right)}\underbrace{e^{\left(-i\vec{k}\cdot\sum n_i\vec{a}_i\right)}}_{1} \\
&= \frac{1}{\sqrt{N}}\sum_{\vec{R}_j} e^{i\left(\vec{k}\cdot\vec{R}_j-\omega t\right)}\vec{u}_j = \vec{u}_{\vec{k}}^{(j)}.
\end{aligned} \tag{1.49}$$

It is important noticing that, in (1.51), the wavevector k can be written as a linear combination of primitive reciprocal vectors, that is, $\vec{k} = \sum_{i=1}^{3} n_i\vec{b}_i$, $\vec{b}_i$ being a basis vector and n_i an integer. Here we have used the property $a_i \cdot b_j = 2\pi\delta_{ij}$. Thus we can rewrite Eq. 1.48 as

$$\left(\left(\sum_j \mathbb{K}^{(1j)} - m_1\omega^2(\vec{k})\mathbb{I}\right) - \left(\mathbb{K}^{(11)}e^0 + \mathbb{K}^{(11')}e^{\vec{k}\cdot\Delta R_{11'}} + ...\right)\right)u_{\vec{k}}^{(1)}$$
$$- \left(\mathbb{K}^{(12)}e^{\vec{k}\cdot\Delta R_{12}} + \mathbb{K}^{(12')}e^{\vec{k}\cdot\Delta R_{12'}} + ...\right)u_{\vec{k}}^{(2)} + ... - \left(\mathbb{K}^{(1n)}e^{\vec{k}\cdot\Delta R_{1n}}\right. \tag{1.50}$$
$$\left. + \mathbb{K}^{(1n')}e^{\vec{k}\cdot\Delta R_{1n'}} + ...\right)u_{\vec{k}}^{(n)},$$

Equation 1.50 can now be written in a more compact form as

$$\mathbb{D}^{11}u_{\vec{k}}^{(1)} + \mathbb{D}^{12}u_{\vec{k}}^{(2)} + ... + \mathbb{D}^{1n}u_{\vec{k}}^{(1)} = 0. \tag{1.51}$$

If we proceed developing Eq. 1.47 for each i atom in the unit cell, we will obtain n simultaneous equations similar to Eq. 1.51 :

$$\begin{aligned}
\mathbb{D}^{11}u_{\vec{k}}^{(1)} + \mathbb{D}^{12}u_{\vec{k}}^{(2)} + ... + \mathbb{D}^{1n}u_{\vec{k}}^{(n)} &= 0 \\
\mathbb{D}^{21}u_{\vec{k}}^{(1)} + \mathbb{D}^{22}u_{\vec{k}}^{(2)} + ... + \mathbb{D}^{2n}u_{\vec{k}}^{(n)} &= 0 \\
. & \quad . \\
. & \quad . \\
. & \quad . \\
\mathbb{D}^{n1}u_{\vec{k}}^{(1)} + \mathbb{D}^{n2}u_{\vec{k}}^{(2)} + ... + \mathbb{D}^{nn}u_{\vec{k}}^{(n)} &= 0
\end{aligned} \tag{1.52}$$

Since each variable $\vec{u}^{i}$ is a 3-component vector, we have a set of $3n$ equations for $3n$ unknown variables $u_{\vec{k}} = {}^{t}\left(u_{\vec{k}}^{(1)}, u_{\vec{k}}^{(2)}, ...u_{\vec{k}}^{(n)}\right)$ where t denotes the transpose. Therefore Equation 1.47 can be formally written as follows by defining a $(3n \times 3n)$ matrix, called the dynamical matrix $\mathbb{D}(\vec{k})$ of the system

$$\mathbb{D}(\vec{k})u_{\vec{k}} = 0. \tag{1.53}$$

In order to obtain the non-trivial eigenvectors $u_{\vec{k}} \neq 0$ and eigenfrequencies $\omega(\vec{k})$ we must solve the secular equation $\mathrm{Det}\mathbb{D}(\vec{k}) = 0$ for a given $\vec{k}$ vector. It is convenient to divide the dynamical matrix $\mathbb{D}(\vec{k})$ into smaller (3×3) matrices $\mathbb{D}^{ij}(\vec{k})$, $(i, j = 1, ..., n)$. By generalizing Equation 1.50, $\mathbb{D}^{ij}(\vec{k})$ can be expressed as

$$\mathbb{D}^{ij}(\vec{k}) = \left(\sum_{j''} \mathbb{K}^{(ij'')} - m_i\omega^2(\vec{k})\mathbb{I}\right)\delta_{ij} - \sum_{j'} \mathbb{K}^{(ij')}e^{\vec{k}\cdot\Delta R_{ij'}}, \tag{1.54}$$

where the sum over j'' runs for all neighbor sites from the i^{th} atom, and the sum over j' runs over those sites which are equivalent to the j^{th} atom [20].

1.3.2 Phonon dispersion relations in Graphene

In graphene there are two inequivalent atoms in the unit cell, A and B, therefore we must consider six coordinates $u_{\vec{k}}$, or six degrees of freedom, in Eq. 1.53. Therefore, in order to obtain

the eigenfrequencies $\omega^2(\vec{k})$, therefore the phonon dispersion relations, we must solve the secular equation for a 6×6 matrix. The dynamical matrix $\mathbb{D}$ is written in terms of the 3×3 matrices $\mathbb{D}^{AA}$, $\mathbb{D}^{AB}$, $\mathbb{D}^{BA}$ and $\mathbb{D}^{BB}$

$$\mathbb{D} = \begin{pmatrix} \mathbb{D}^{AA} & \mathbb{D}^{AB} \\ \mathbb{D}^{BA} & \mathbb{D}^{BB} \end{pmatrix}, \tag{1.55}$$

with each $\mathbb{D}^{ij}$ matrix given by Eq. 1.54. Therefore, to define the dynamic matrix 1.55, we need prior information about the force constant tensor $\mathbb{K}^{(ij)}$ which represents the interaction between i and j atoms. Lets set $i = A$ and $j = B$ to construct the $\mathbb{D}^{AB}$ matrix element. In this case, the first term of Eq. 1.54 vanishes since $i \neq j$, and the matrix will be constructed by adding the product of the constant tensor $\mathbb{K}^{(AB')}$ with the phase factor $e^{i\vec{k}\cdot\Delta\vec{R}_{AB'}}$, where the sum ranges over all equivalent B atoms. So, let us fix an A atom and look for its interactions with its first neighbors as illustrated in Fig. 1.8 (a), and verify which of these are $A - B'$ interactions (represented by $\mathbb{K}^{(AB')}$). In Fig. 1.8 (a) they correspond to interactions of A atom with the first, third, and fourth neighbors represented, respectively, by open circles, open squares, and open hexagons.

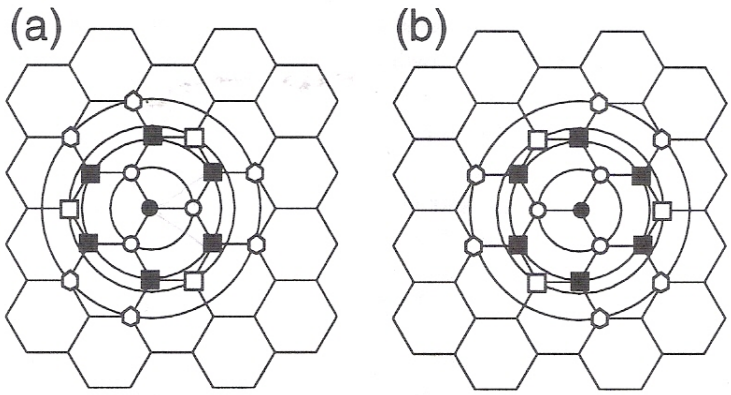

Figure 1.8: First-neighbor atoms in a graphene plane, considering up to the 4th nearest neighbors for (a) an A atom, and (b) a B atom at the center of the solid circles. The circles connect the same neighbor atoms and are drawn as guides to the eye. From the 1^{st} to the 4^{st} neighbor atoms, they are represented by open circles, solid squares, open squares, and open hexagons, respectively. Figure taken from [20].

To obtain the $\mathbb{D}^{AA}$ matrix element we set $i = j = A$. In this case, we must consider both terms in Eq. 1.54. Since the summation in the first term is taken over all neighbor sites from the A atom, there will be contributions from all first 4th nearest neighbors in Fig. 1.8 (a) to this term. The second term will contain contributions only from the equivalent A atoms, that is, the second

neighbors. The $\mathbb{D}^{BB}$ and $\mathbb{D}^{BA}$ matrix elements can be obtained in a similar fashion, by fixing the B atoms and looking for its interactions with its first neighbors, as illustrated in Fig. 1.8 (b).

The remaining problem is to construct the force constant tensor $\mathbb{K}^{(ij)}$. First we consider the force constant between an A atom and a nearest-neighbor B_1 atom, both of them lying on the x-axis as shown in Fig. 1.9.

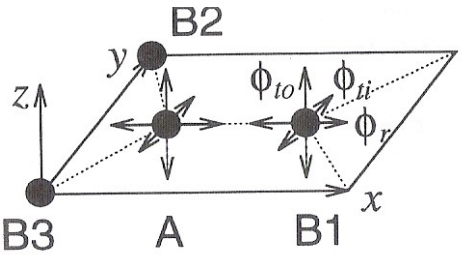

Figure 1.9: Force constants between the A and B_1 atoms on a graphene sheet. The interaction is represented by the components of the force constant tensor ϕ_r, ϕ_{ti} and ϕ_{to} for the nearest-neighbor atoms in the radial (bond-streching), in-plane, and out-of plane tangential (bond-bending) directions, respectively. B_2 and B_3 are the nearest neighbors equivalent to B_1, whose force constant tensor is obtained by rotation of the system. Figure taken from [20].

For the coordinate system defined in Fig. 1.9, the force constant tensor can be written in a diagonal form as

$$\mathbb{K}^{AB_1} = \begin{pmatrix} \phi_r^{(1)} & 0 & 0 \\ 0 & \phi_{ti}^{(1)} & 0 \\ 0 & 0 & \phi_{to}^{(1)}, \end{pmatrix} \tag{1.56}$$

where $\phi_r^{(n)}, \phi_{ti}, \text{and} \phi_{to}$ represent the force constant parameters in the radial (bond-straching), in-plane and out-of-plane tangential (bond-bending) directions of the n^{th} nearest neighbors, respectively [20]. The graphene plane is in the xy plane, and the radial direction corresponds to the direction of the σ bonds. The two tangential directions (y and z) are taken to be perpendicular to the radial direction. The corresponding phase factor $\exp(i\vec{k} \cdot \Delta\vec{R}_{ij})$ becomes $\exp(-i\, k_x a/\sqrt{3})$ for the B_1 atom at $(a/\sqrt{3}, 0, 0)$.

The force constant matrices for the two other nearest-neighbor atoms, B_2 and B_3 are obtained by rotating the system. Thus, according to the rules for a second-rank tensor we have

$$\mathbb{K}^{A,B_\alpha} = \mathbb{U}_\alpha^{-1}\mathbb{K}^{A,B_1}\mathbb{U}, \qquad (\alpha = 2,3) \tag{1.57}$$

where the unitary matrix $\mathbb{U}_\alpha$ is here defined as a rotation matrix around the z axis in Fig. 1.9, taking the B_1 atom into the B_α atom,

$$\mathbb{U}_\alpha = \begin{pmatrix} \cos\theta_\alpha & \sin\theta_\alpha & 0 \\ -\sin\theta_\alpha & \cos\theta_\alpha & 0 \\ 0 & 0 & 1, \end{pmatrix} \tag{1.58}$$

As an example, the force constant matrix for the B_2 atom at $(-a/(2\sqrt{3}), a/2, 0)$, with $\mathbb{U}_2$ evaluated at $\theta_2 = 2\pi/3$, is given by

$$\mathbb{K}^{AB_2} = \frac{1}{4}\begin{pmatrix} \phi_r^{(1)} + 3\phi_{ti}^{(1)} & \sqrt{3}\left(\phi_{ti}^{(1)} - \phi_r^{(1)}\right) & 0 \\ \sqrt{3}\left(\phi_{ti}^{(1)} - \phi_r^{(1)}\right) & 3\phi_r^{(1)} + \phi_{ti}^{(1)} & 0 \\ 0 & 0 & \phi_{to}^{(1)} \end{pmatrix}, \tag{1.59}$$

and the corresponding phase factor is $\exp(-ik_x a/(2\sqrt{3}) + ik_y a/2)$.

To calculate the phonon dispersion relations for graphene, the interaction between two nearest-neighbor atoms is not sufficient to reproduce the experimental results, and we generally need to consider contributions from long-distance forces, such as from the n^{th} neighbor atoms, ($n = 1, 2, 3, 4, ...$) [20]. The values for the force constants ϕ^n [26] are obtained by fitting experimental data over the Brillouin zone, as for example from inelastic neutron scattering or electron energy loss spectroscopy measurements along the ΓM direction [26, 27].

Table 1.1: Force constants parameters for graphene obtained experimentally in units of 10^4 dyn/cm [26]. The subscripts r, *ti*, and *to* refer to radial, transverse in-plane and transverse out-of-plane, respectively.

Radial	Tangential	
$\phi_r^{(1)} = 36.50$	$\phi_{ti}^{(1)} = 24.50$	$\phi_{to}^{(1)} = 9.82$
$\phi_r^{(2)} = 8.80$	$\phi_{ti}^{(2)} = -3.23$	$\phi_{to}^{(2)} = -0.40$
$\phi_r^{(3)} = 3.00$	$\phi_{ti}^{(3)} = -5.25$	$\phi_{to}^{(3)} = 0.15$
$\phi_r^{(4)} = -1.92$	$\phi_{ti}^{(4)} = 2.29$	$\phi_{to}^{(4)} = -0.58$

In Fig. 1.10 the phonon dispersion curves for graphene are shown using the set of force constants depicted in Table 1.1. The three phonon branches with null frequency at the Γ point of the Brillouin zone correspond to the three acoustic modes, namely the out of plane, the in-plane tangential (bond-bending), and the in-plane radial modes listed in order of increasing energy, along the ΓM of ΓK directions. The remaining three branches correspond to the optical modes, one out of plane and two in plane.

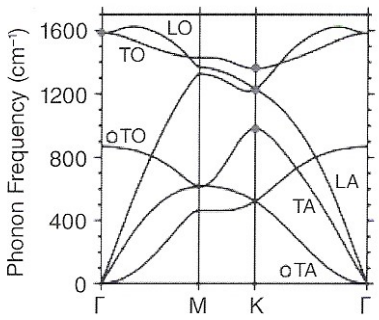

Figure 1.10: Phonon dispersion in graphene along the high-symmetry directions in the Brillouin zone. Figure taken from [28].

Thus far, everything we did lies within the scope of classical mechanics. However an accurate description of the motion of the lattice requires quantum mechanical considerations. For instance there is a quantum mechanical analog for the classical lattice wave described by Eq. 1.43, and it is called a *phonon*. As expected, the energy carried by this excitation is quantized, as a single phonon of angular frequency ω carries energy $\hbar\omega$ [29].

1.4 The electron-phonon interaction

Having studied both the electronic and phonon dispersion relations of graphene, the next step is to understand how these particles interact, and which phenomena arises from this interaction. Such an understanding will be needed when studying the Raman effect in graphene. Even though the assumptions made during the calculations in this section do not strictly hold for graphene, the qualitative analysis is still important to give some insight into the electron-phonon interaction. The electron-phonon interaction is the responsible for the scattering of electrons by phonons, which constitutes a major step in a Raman process. Besides, phenomena such as the Khon anomaly and the renormalization of the phonon frequency play important roles in the Raman Spectrum of graphene.

1.4.1 The residual electric field

The best way to picture the origin of the electron-phonon interaction is to start by considering a vibration of a lattice of unscreened ions. We then allow the electron gas to flow into the regions of compression in order to restore the electrical neutrality of the system on a macroscopic scale. However, an increase in the local density of electrons must be balanced by extra kinetic energy according to the uncertainty principle. Therefore, these regions exhibit a lower electric potential energy and a higher kinetic energy for the electrons. The opposite is true for regions of decompression, where the decrease in the local density of electrons is balanced by a decrease in the kinetic energy resulting in a higher electric potential energy and lower kinetic energy for the electrons. In a more careful treatment, the electron gas would not completely screen the electric field of the ions, and they would not be able to restore the electrical neutrality of the system. Instead, the electrons would flow until the sum of the electric potential energy and the kinetic energy became uniform. There would then be a residual electric field tending to restore the ions to their equilibrium positions. The action of this residual electric field on the electrons that gives rise to the electron-phonon interaction [29].

1.4.2 The Fröhlich Hamiltonian

The interaction of phonons with electrons is a complicated subject and the more complex the system is, the more difficult its mathematical treatment will be. In order to illustrate the main consequences of the interaction between phonons and electrons, in this section we shall consider our system to be a simple metal in which, the ions interact with each other and with the electrons only through a short-range screened potential. By making use of the second-quantized notation, the unperturbed Hamiltonian of our material system is

$$\mathscr{H}_0 = \sum_{\vec{k}} \mathscr{E}_{\vec{k}}\, c^{\dagger}_{\vec{k}}\, c_{\vec{k}} + \sum_{\vec{q},\vec{s}} \hbar\omega_{\vec{q},\vec{s}}\, a^{\dagger}_{\vec{q},\vec{s}}\, a_{\vec{q},\vec{s}} \tag{1.60}$$

with $c^{\dagger}_{\vec{k}}$ and $a^{\dagger}_{\vec{q},\vec{s}}$ ($c_{\vec{k}}$ and $a_{\vec{q},\vec{s}}$) being the creation (annihilation) operators creating (annihilating) an electron in the state characterized by the wave vector $\vec{k}$, and a phonon with wave vector $\vec{q}$ and polarization $\vec{s}$, respectively. Next, we add the interaction Hamiltonian $\mathscr{H}_I$ of the electrons with the screened ions. We assume that the potential due to a particular ion in a given position depends only on the distance from the center of the ion, assumption known as the rigid-ion

approximation.In this scenario, the perturbative Hamiltonian assumes the form

$$\begin{aligned}\mathscr{H}_I &= \sum_{\vec{k},\vec{k}',l} \langle \vec{k}|V(\vec{r}-(\vec{l}+\vec{y}_l))|\vec{k}'\rangle\, c^\dagger_{\vec{k}} c_{\vec{k}'} \\ &= \sum_{\vec{k},\vec{k}',l} e^{i(\vec{k}'-\vec{k})\cdot(\vec{l}+\vec{y}_l)} V_{\vec{k}-\vec{k}'}\, c^\dagger_{\vec{k}} c_{\vec{k}'} \\ V_{\vec{k}-\vec{k}'} &= \frac{1}{\Omega}\int e^{i(\vec{k}'-\vec{k})\cdot\vec{r}} V(\vec{r}) d\vec{r}\end{aligned} \tag{1.61}$$

with Ω being the volume of the solid, $\vec{l}$ and $\vec{y}_l$ the equilibrium position and the displacement from the equilibrium position of the ion, respectively. Here $V(\vec{r})$ is the potential due to a single ion at the origin. Note that we are adopting plane wave $\exp i(\vec{k}\cdot\vec{r})$ solutions as the eigenstates of the unperturbed electrons. With the assumption that the displacement $\vec{y}_l$ of the ion (whose equilibrium position is $\vec{l}$) is sufficiently small to lead $(\vec{k}-\vec{k}')\cdot\vec{y}_l \ll 1$, we can write

$$\begin{aligned}e^{i(\vec{k}'-\vec{k})\cdot\vec{y}_l} &\simeq 1 + i(\vec{k}-\vec{k}')\cdot\vec{y}_l \\ &= 1 + iN^{-1/2}(\vec{k}-\vec{k}')\cdot\sum_{\vec{q}} e^{i\vec{q}\cdot\vec{l}}\vec{y}_q.\end{aligned} \tag{1.62}$$

Where we used that

$$\vec{y}_l = N^{-1/2}\sum_{\vec{q}} e^{i\vec{q}\cdot\vec{l}}\vec{y}_q. \tag{1.63}$$

Here, Eq. 1.63 is the quantum analog of Eq. 1.43 and arises when solving the motion of the lattice in a quantum mechanical approach. Notice that, unlike Eq. 1.43, there is no time dependent term in this equation, which resembles a static wave solution. This is the underlying assumption behind the adiabatic Born-Oppenheimer approximation (ABO) which, as we shall see in Sec. 3.2.2, does not hold for graphene. However, we are going to use ABO to get some important results that will enable a better understanding of the electron-phonon interaction. Back to our analysis,the perturbative Hamiltoninan $\mathscr{H}_I$ can be split in two parts,

$$\mathscr{H}_I = \mathscr{H}_{\text{Bloch}} + \mathscr{H}_{ep}, \tag{1.64}$$

with $\mathscr{H}_{\text{Bloch}}$ being the periodic potential of the stationary lattice, which is independent of the lattice displacements, and $\mathscr{H}_{ep}$ the electron-phonon interaction Hamiltonian.. For $\mathscr{H}_{\text{Bloch}}$ we have

$$\mathscr{H}_{\text{Bloch}} = \sum_{\vec{k},\vec{k}',\vec{l}} e^{i(\vec{k}'-\vec{k})\cdot\vec{l}} V_{\vec{k}-\vec{k}'}\, c^\dagger_{\vec{k}} c_{\vec{k}'}. \tag{1.65}$$

Now recall that a summation on the form $\sum_{\vec{l}} \exp i(\vec{q}\cdot\vec{l})$ vanishes unless $\vec{q}$ is equal to some $\vec{g}$, a vector of the reciprocal lattice, in which case the sum is equal to N, the total number of atoms. Thus

$$\begin{aligned} \sum_{\vec{k},\vec{k}',\vec{l}} e^{i(\vec{k}'-\vec{k})\cdot\vec{l}} &= \sum_{\vec{k},\vec{k}',\vec{l}} \delta_{\vec{k}'-\vec{k},\vec{g}}\, e^{i(\vec{k}'-\vec{k})\cdot\vec{l}} = N \\ \mathscr{H}_{\text{Bloch}} &= N \sum_{\vec{k},\vec{g}} V_{-\vec{g}}\, c^{\dagger}_{\vec{k}-\vec{g}} c_{\vec{k}}. \end{aligned} \tag{1.66}$$

The electron-phonon Hamiltonian is given as

$$\begin{aligned} \mathscr{H}_{ep} &= iN^{-1/2} \sum_{\vec{k},\vec{k}',\vec{l},\vec{q}} e^{i(\vec{k}'-\vec{k}+\vec{q})\cdot\vec{l}} (\vec{k}'-\vec{k})\cdot\vec{y}_{\vec{q}}\, V_{\vec{k}-\vec{k}'}\, c^{\dagger}_{\vec{k}} c_{\vec{k}'} \\ &= iN^{1/2} \sum_{\vec{k},\vec{k}'} (\vec{k}'-\vec{k})\cdot\vec{y}_{\vec{k}-\vec{k}'}\, V_{\vec{k}-\vec{k}'}\, c^{\dagger}_{\vec{k}} c_{\vec{k}'}. \end{aligned} \tag{1.67}$$

Again, we made use of the property of summation over $\vec{l}$: it vanishes unless $\vec{k}'-\vec{k}+\vec{q}=\vec{g}$.

Next, we express $\vec{y}_{\vec{k}-\vec{k}'}$ in terms of the creation and annihilation operators, a result that comes from the quantum treatment of the motion of the crystal:

$$\vec{y}_{\vec{q}} = \left(\frac{\hbar}{2M\omega_{\vec{k}-\vec{k}',\vec{s}}}\right)^{1/2} \vec{s}\left(a^{\dagger}_{-\vec{q},\vec{s}} + a_{\vec{q},\vec{s}}\right) \tag{1.68}$$

Inserting Eq. 1.68 into Eq. 1.67 we get the expression for the Electron-Phonon interaction Hamiltonian,

$$\mathscr{H}_{ep} = i \sum_{\vec{k},\vec{k}',\vec{s}} \left(\frac{N\hbar}{2M\omega_{\vec{k}-\vec{k}',\vec{s}}}\right)^{1/2} (\vec{k}'-\vec{k})\cdot\vec{s}\, V_{\vec{k}-\vec{k}'} (a^{\dagger}_{\vec{k}'-\vec{k},\vec{s}} + a_{\vec{k}-\vec{k}',\vec{s}}) c^{\dagger}_{\vec{k}} c_{\vec{k}'}. \tag{1.69}$$

For the sake of simplicity we shall assume the phonon spectrum to be isotropic, that is, the phonons will be either longitudinally or transversely polarized. With this assumption only the longitudinal modes, for which $\vec{s}$ is parallel to $\vec{k}'-\vec{k}$, are considered in $\mathscr{H}_{ep}$. We shall also neglect the effects of $\mathscr{H}_{\text{Bloch}}$. After this simplifications we are left with the Fröhlich Hamiltonian,

$$\mathscr{H} = \sum_{\vec{k}} \mathscr{E}_{\vec{k}} c^{\dagger}_{\vec{k}} c_{\vec{k}} + \sum_{\vec{q}} \hbar\omega_{\vec{q}} a^{\dagger}_{\vec{q}} a_{\vec{q}} + \sum_{\vec{k},\vec{k}'} M_{\vec{k}\vec{k}'} \left(a^{\dagger}_{-\vec{q}} + a_{\vec{q}}\right) c^{\dagger}_{\vec{k}} c_{\vec{k}'}, \tag{1.70}$$

where the electron-phonon matrix element is defined as

$$M_{\vec{k}\vec{k}'} = i\left(\frac{N\hbar}{2M\omega_{\vec{q}}}\right)^{1/2} \left|\vec{k}'-\vec{k}\right| V_{\vec{k}-\vec{k}'}, \tag{1.71}$$

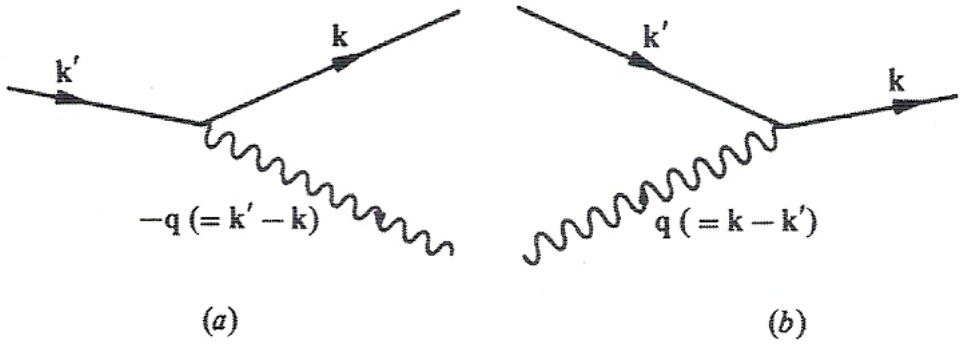

Figure 1.11: Diagrams representing the interaction terms in the Frohlich Hamiltonian. The electron is scattered from state $\vec{k}'$ to state $\vec{k}$ either by (a) emission of (b) absorption of a phonon. Figure from [29].

with the phonon wavenumber $\vec{q}$, reduced to the first Brillouin zone, equals to $\vec{k} - \vec{k}'$.

We can think of the electron-phonon Hamiltonian $\mathscr{H}_{ep}$ as composed of two parts, terms involving $a^{\dagger}_{-\vec{q}} c^{\dagger}_{\vec{k}} c_{\vec{k}'}$ and terms involving $a^{\dagger}_{\vec{q}} c^{\dagger}_{\vec{k}} c_{\vec{k}'}$. These may be represented by the diagrams shown in Figs. 1.11 (a) and 1.11 (b), respectively. In the first diagram we have an electron scattered from state $\vec{k}'$ to state $\vec{k}$ by emission of a phonon with wavenumber $\vec{k}' - \vec{k}$. In the second diagram the electron is scattered from state $\vec{k}'$ to state $\vec{k}$ by absorption of a phonon of wavenumber $\vec{k} - \vec{k}'$ [29].

1.4.3 Renormalization of the phonon frequencies and the Khon Anomaly

In order to determine how the electron-phonon interaction affects the phonon spectrum, we must use Perturbation Theory to calculate the energy of the system described by the Fröhlich Hamiltonian. The first two terms of the Fröhlich Hamiltonian 1.70 are the unperturbed terms, while the $\mathscr{H}_{ep}$ term represents the perturbation. The energy up to second order in $\mathscr{H}_{ep}$ is

$$\mathscr{E} = \mathscr{E}_0 + \langle\phi|\mathscr{H}_{ep}|\phi\rangle + \langle\phi|\mathscr{H}_{ep}(\mathscr{E}_0 - \mathscr{H}_0)^{-1}\mathscr{H}_{ep}|\phi\rangle \tag{1.72}$$

with $\mathscr{E}_0$ being the unperturbed energy of the state $|\phi\rangle$ having $n_{\vec{q}}$ phonons in the longitudinally polarized mode $\vec{q}$ and $n_{\vec{k}}$ electrons in state $\vec{k}$, $|\phi\rangle = |n_{\vec{q}}, n_{\vec{k}}\rangle$. Since the components of $\mathscr{H}_{ep}$ act on $|\phi\rangle$ either to create or destroy one phonon, the resulting wavefunction must be orthogonal to $|\phi\rangle$, therefore the first-order term vanishes from this expression. The second-order term is

$$
\begin{aligned}
\mathscr{E}_2 &= \langle\phi| \sum_{\vec{k},\vec{k}'} M_{\vec{k}\vec{k}'} \left(a^\dagger_{-\vec{q}} + a_{\vec{q}}\right) c^\dagger_{\vec{k}} c_{\vec{k}'} (\mathscr{E}_0 - \mathscr{H}_0)^{-1} \\
&\times \sum_{\vec{k}'',\vec{k}'''} M_{\vec{k}''\vec{k}'''} \left(a^\dagger_{-\vec{q}'} + a_{\vec{q}'}\right) c^\dagger_{\vec{k}''} c_{\vec{k}'''} |\phi\rangle \\
&= \langle\phi| \sum_{\vec{k},\vec{k}',\vec{k}'',\vec{k}'''} M_{\vec{k}\vec{k}'} M_{\vec{k}''\vec{k}'''} \left[a^\dagger_{-\vec{q}} c^\dagger_{\vec{k}} c_{\vec{k}'} (\mathscr{E}_0 - \mathscr{H}_0)^{-1} + a_{\vec{q}} c^\dagger_{\vec{k}} c_{\vec{k}'} (\mathscr{E}_0 - \mathscr{H}_0)^{-1}\right] \\
&\left(a_{-\vec{q}'} c^\dagger_{\vec{k}''} c_{\vec{k}'''} + a^\dagger_{\vec{q}'} c^\dagger_{\vec{k}''} c_{\vec{k}'''}\right) |\phi\rangle \,.
\end{aligned}
\tag{1.73}
$$

By developing this expression, we have

$$
\begin{aligned}
\mathscr{E}_2 = \sum_{\vec{k},\vec{k}',\vec{k}'',\vec{k}'''} & M_{\vec{k}\vec{k}'} M_{\vec{k}''\vec{k}'''} \langle\phi| \Big(a^\dagger_{-\vec{q}} c^\dagger_{\vec{k}} c_{\vec{k}'} (\mathscr{E}_0 - \mathscr{H}_0)^{-1} a^\dagger_{-\vec{q}'} c^\dagger_{\vec{k}''} c_{\vec{k}'''} + \\
& a^\dagger_{-\vec{q}} c^\dagger_{\vec{k}} c_{\vec{k}'} (\mathscr{E}_0 - \mathscr{H}_0)^{-1} a_{\vec{q}'} c^\dagger_{\vec{k}''} c_{\vec{k}'''} + a_{\vec{q}} c^\dagger_{\vec{k}} c_{\vec{k}'} (\mathscr{E}_0 - \mathscr{H}_0)^{-1} a^\dagger_{-\vec{q}'} c^\dagger_{\vec{k}''} c_{\vec{k}'''} \\
& + a_{\vec{q}} c^\dagger_{\vec{k}} c_{\vec{k}'} (\mathscr{E}_0 - \mathscr{H}_0)^{-1} a_{\vec{q}'} c^\dagger_{\vec{k}''} c_{\vec{k}'''} \Big) |\phi\rangle
\end{aligned}
\tag{1.74}
$$

The first and the fourth term inside the parenthesis in Eq. 1.74 vanish because the creation (annihilation) operators act twice on $|\phi\rangle$ resulting in a wavefunction orthogonal to $|\phi\rangle$. Besides, the second and third terms will vanish unless $\vec{k}'''$ is equal to $\vec{k}$, and $\vec{k}''$ is equal to $\vec{k}'$. Thus the contribution from the second order term is

$$
\begin{aligned}
\mathscr{E}_2 = \langle\phi| \sum_{\vec{k},\vec{k}'} & \left|M_{\vec{k}\vec{k}'}\right|^2 \left[a^\dagger_{-\vec{q}} c^\dagger_{\vec{k}} c_{\vec{k}'} (\mathscr{E}_0 - \mathscr{H}_0)^{-1} a_{-\vec{q}} c^\dagger_{\vec{k}'} c_{\vec{k}} \right. \\
& \left. + a_{\vec{q}} c^\dagger_{\vec{k}} c_{\vec{k}'} (\mathscr{E}_0 - \mathscr{H}_0)^{-1} a^\dagger_{\vec{q}} c^\dagger_{\vec{k}'} c_{\vec{k}} |\phi\rangle \,,\right.
\end{aligned}
\tag{1.75}
$$

where we used $M_{\vec{k}'\vec{k}} = M_{\vec{k}\vec{k}'}{}^*$. The first term in brackets in Eq. 1.75 can be represented as in Fig. 1.12 (a). An electron is first scattered from the state $\vec{k}$ to $\vec{k}'$ with the absorption of a phonon of wavenumber $-\vec{q} = \vec{k}' - \vec{k}$. The factor $(\mathscr{E}_0 - \mathscr{H}_0)^{-1}$ then measures the amount of time the electron is allowed to stay in the intermediate state $\vec{k}'$ by the Uncertainty Principle. In the situation illustrated in Fig. 1.12 (a), the energy difference between the initial and intermediate states is $\mathscr{E}_{\vec{k}} + \hbar\omega_{-\vec{q}} - \mathscr{E}_{\vec{k}'}$, so a factor of $(\mathscr{E}_{\vec{k}} + \hbar\omega_{-\vec{q}} - \mathscr{E}_{\vec{k}'})^{-1}$ is considered. The electron is then scattered back into its original state $\vec{k}$ with the re-emission of a phonon. The second term in Eq. 1.75 can be represented by Fig. 1.12 (b). An electron is first scattered from state $\vec{k}$ to state $\vec{k}'$ by emission of a phonon of wavenumber $\vec{q} = \vec{k} - \vec{k}'$. In this case a factor of $(\mathscr{E}_{\vec{k}} - (\hbar\omega_{\vec{q}} + \mathscr{E}_{\vec{k}'}))^{-1}$ is attained.

We can rewrite Eq. 1.75 in terms of the occupation numbers $n_{\vec{k}}$ and $n_{\vec{q}}$, and by making use of the commutation and anticommutation relations of the creation/annihilation operators for

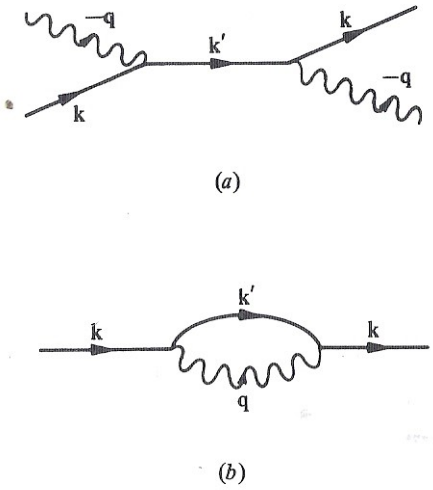

Figure 1.12: These interactions contribute to a second-order correction to the energy of the electron-phonon system in perturbaion theory. Figure from [29].

bosons and fermions. For electrons (fermions) we have,

$$\begin{aligned} c^\dagger_{\vec{k}} c_{\vec{k}} &= n_{\vec{k}}, \qquad c_{\vec{k}} c^\dagger_{\vec{k}} = (1 - n_{\vec{k}}) \\ \{c_{\vec{k}}, c^\dagger_{\vec{k}}\} &= 1, \quad \{c_{\vec{k}}, c^\dagger_{\vec{k}'}\} = 0, \quad \{c_{\vec{k}}, c_{\vec{k}'}\} = 0. \end{aligned} \tag{1.76}$$

For phonons (bosons) we have,

$$a^\dagger_{\vec{q}} a_{\vec{q}} = n_{\vec{q}}, \quad a_{\vec{q}} a^\dagger_{\vec{q}} = (1 + n_{\vec{q}}), \quad [a_{\vec{q}}, a^\dagger_{\vec{q}}] = 1. \tag{1.77}$$

Thus Eq. 1.75 can be rewritten as

$$\mathscr{E}_2 = \sum_{\vec{k},\vec{k}'} \left| M_{\vec{k}\vec{k}'} \right|^2 \langle n_{\vec{k}}(1 - n_{\vec{k}'}) \rangle \left(\frac{\langle n_{-\vec{q}} \rangle}{\mathscr{E}_{\vec{k}} + \hbar\omega_{-\vec{q}} - \mathscr{E}_{\vec{k}'}} + \frac{\langle n_{\vec{q}} + 1 \rangle}{\mathscr{E}_{\vec{k}} - (\hbar\omega_{\vec{q}} + \mathscr{E}_{\vec{k}'})} \right). \tag{1.78}$$

It may be assumed that $\omega_{\vec{q}} = \omega_{-\vec{q}}$, so that in equilibrium $\langle n_{\vec{q}} \rangle = \langle n_{-\vec{q}} \rangle$. The term $\langle n_{\vec{k}} n_{\vec{k}'} n_{\vec{q}} \rangle$ cancels by symmetry. Thus Eq. 1.78 can be rearranged to find,

$$\begin{aligned} \mathscr{E}_2 = \sum_{\vec{k},\vec{k}'} \left| M_{\vec{k}\vec{k}'} \right|^2 \Big(& \frac{[\langle n_{\vec{k}} n_{\vec{q}} \rangle + \cancel{\langle n_{\vec{k}} n_{\vec{k}'} n_{\vec{q}} \rangle}^{0}](\mathscr{E}_{\vec{k}} - \mathscr{E}_{\vec{k}'} - \hbar\omega_{\vec{q}})}{(\mathscr{E}_{\vec{k}} - \mathscr{E}_{\vec{k}'})^2 - (\hbar\omega_{\vec{q}})^2} \\ & + \frac{[\langle n_{\vec{k}} n_{\vec{q}} \rangle + \langle n_{\vec{k}} \rangle - \cancel{\langle n_{\vec{k}} n_{\vec{k}'} n_{\vec{q}} \rangle}^{0} - \langle n_{\vec{k}} n_{\vec{k}'} \rangle](\mathscr{E}_{\vec{k}} - \mathscr{E}_{\vec{k}'} + \hbar\omega_{\vec{q}})}{(\mathscr{E}_{\vec{k}} - \mathscr{E}_{\vec{k}'})^2 - (\hbar\omega_{\vec{q}})^2} \Big) \\ \mathscr{E}_2 = \sum_{\vec{k},\vec{k}'} \left| M_{\vec{k}\vec{k}'} \right|^2 \langle n_{\vec{k}} \rangle & \left[\frac{2\langle n_{\vec{q}} \rangle (\mathscr{E}_{\vec{k}} - \mathscr{E}_{\vec{k}'})}{(\mathscr{E}_{\vec{k}} - \mathscr{E}_{\vec{k}'})^2 - (\hbar\omega_{\vec{q}})^2} + \frac{1 - \langle n_{\vec{k}'} \rangle}{\mathscr{E}_{\vec{k}} - \mathscr{E}_{\vec{k}'} - \hbar\omega_{\vec{q}}} \right] \end{aligned} \tag{1.79}$$

Finally the energy corrected to second order is on the form

$$\mathscr{E} = \hbar\omega_{\vec{q}} \langle n_{\vec{q}} \rangle + \sum_{\vec{k},\vec{k}'} \left| M_{\vec{k}\vec{k}'} \right|^2 \langle n_{\vec{k}} \rangle \left[\frac{2\langle n_{\vec{q}} \rangle (\mathscr{E}_{\vec{k}} - \mathscr{E}_{\vec{k}'})}{(\mathscr{E}_{\vec{k}} - \mathscr{E}_{\vec{k}'})^2 - (\hbar\omega_{\vec{q}})^2} + \frac{1 - \langle n_{\vec{k}'} \rangle}{\mathscr{E}_{\vec{k}} - \mathscr{E}_{\vec{k}'} - \hbar\omega_{\vec{q}}} \right] \tag{1.80}$$

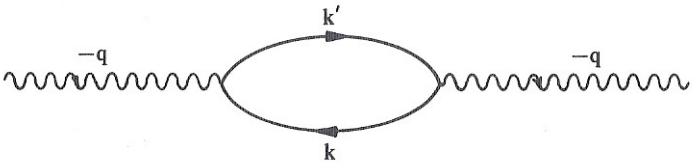

Figure 1.13: An alternative way of representing Figure 1.12 (a). In this picture the phonon spends part of its time as a virtual electron-hole pair. Figure from [29]

The effect of the electron-phonon interaction on the phonon spectrum is contained in the term proportional to $\langle n_{\vec{q}} \rangle$ in Eq. 1.80 [29]. We identify the perturbed phonon energy, $\hbar\omega^p_{\vec{q}}$, with the energy required to increase $\langle n_{\vec{q}} \rangle$ by unity, so

$$\begin{aligned} \hbar\omega^p_{\vec{q}} &= \frac{\partial \mathscr{E}}{\partial \langle n_{\vec{q}} \rangle} \\ &= \hbar\omega_{\vec{q}} + \sum_{\vec{k}} \left| M_{\vec{k}\vec{k}'} \right|^2 \frac{2\langle n_{\vec{k}} \rangle (\mathscr{E}_{\vec{k}} - \mathscr{E}_{\vec{k}'})}{(\mathscr{E}_{\vec{k}} - \mathscr{E}_{\vec{k}'})^2 - (\hbar\omega_{\vec{q}})^2} \end{aligned} \tag{1.81}$$

If we neglect the phonon energy in the denominator, compared to the electron energies, we have

$$\hbar\omega^p_{\vec{q}} \approx \hbar\omega_{\vec{q}} - \sum_{\vec{k}} 2 \left| M_{\vec{k}\vec{k}'} \right|^2 \frac{\langle n_{\vec{k}} \rangle}{(\mathscr{E}_{\vec{k}} - \mathscr{E}_{\vec{k}'})} \tag{1.82}$$

with $\vec{k}' = \vec{k} - \vec{q}$. There is a nice interpretation of the origin of this change in phonon frequency if we redraw Fig.1.12(a) in the form of Fig. 1.13. In the latter, the first interaction is represented not as the scattering of an electron but as the creations of an electron-hole pair. Thus it is possible to interpret that it is the fact that the phonon decay into an electron-hole pair that modifies its energy.

An important consequence of Eq. 1.82 occurs in metals when $\vec{q}$ approaches the diameter $2\vec{k}_F$ of the Fermi surface. Let us suppose $\vec{q}$ to be in the x-direction and evaluate $\partial\hbar\omega^p_{\vec{q}}/\partial q_x$. If we neglect the variation of $M_{\vec{k}\vec{k}'}$ with $\vec{q}$ we get

$$\begin{aligned} \frac{\partial\hbar\omega^p_{\vec{q}}}{\partial q_x} &= \sum_{\vec{k}} 2 \left| M_{\vec{k}\vec{k}'} \right|^2 \frac{\langle n_{\vec{k}} \rangle}{(\mathscr{E}_{\vec{k}-\vec{q}} - \mathscr{E}_{\vec{k}})^2} \frac{\partial \mathscr{E}_{\vec{k}-\vec{q}}}{\partial q_x} \\ &= \sum_{\vec{k}} 2 \left| M_{\vec{k}\vec{k}'} \right|^2 \langle n_{\vec{k}} \rangle \frac{4m}{\hbar^2} \frac{k_x - q}{[q^2(2k_x - q)]^2}. \end{aligned} \tag{1.83}$$

Thus the term $[q(2k_x - q)]^2$ causes a logarithmic divergence when the summation is performed whenever $q = 2k_F$. The kink in the spectrum when $q = 2k_F$ constitutes the *Khon anomaly*.

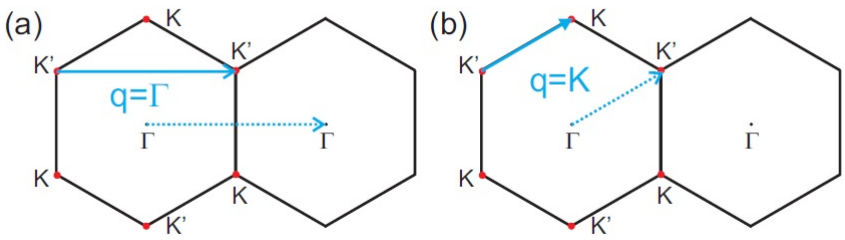

Figure 1.14: Representation of the two phonons $\vec{q} = \Gamma$ (a) and $\vec{q} = \vec{K}$ (b) that can connect two electronic states at the Fermi surface in graphene. Figure from [32].

Kohn anomalies will occur when there is only one reciprocal lattice vector $\vec{K_L}$ such that the vector $\vec{q}$ connecting two states $\vec{K_1}$ and $\vec{K_2}$, both at the Fermi surface, lies in the First Brillouin Zone [30], that is

$$\vec{q} = \vec{k_2} - \vec{k_1} + \vec{K_L}. \tag{1.84}$$

In graphene, the Fermi "surface" is formed by the six K points. There are two possible $\vec{q}$ vectors connecting two electronic states at the Fermi surface according to Equation 1.83: $\vec{q} = \Gamma$, connecting equivalent states as in Fig. 1.14 (a) and $\vec{q} = \vec{K}$ connecting inequivalent states as in Fig. 1.14 (b). Therefore, Khon anomalies can occur in Graphene for $\vec{q} = \Gamma$ or $\vec{q} = \vec{K}$ [31].

Chapter 2

Raman Spectroscopy

2.1 Raman Theory: a quantum approach

The Raman effect is the inelastic scattering of light by matter. In this work we will keep our focus on the light scattering by solids. There are two possibilities for this phenomena, either the incident light looses energy to the medium or it gains energy from it. The first possibility gives rise to the so called Stokes component of the scattered light, while the last one gives the anti-Stokes component.

If the incident light has a frequency ω_I, each scattered photon of the Stokes component has a lower frequency ω_S. This frequency downshift is related to a gain in energy $\hbar\omega_{\vec{q}}$ by the sample, where

$$\omega_{\vec{q}} = \omega_I - \omega_S . \tag{2.1}$$

The reason of the subscript $\vec{q}$ will soon be explained. Likewise, each scattered photon of the anti-Stokes component has a higher frequency ω_{AS} with a loss in energy (by the same amount) $\hbar\omega_{\vec{q}}$ by the sample, where

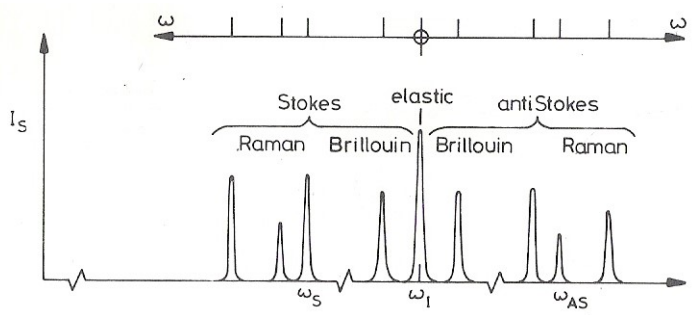

Figure 2.1: Schematic representation of a typical spectrum of scattered light. Left: The Stokes components, lower frequencies. Center: The elastic component of scattered light. Right: The anti-Stokes components, higher frequencies. Figure taken from [33].

$$\omega_{\vec{q}} = \omega_{AS} - \omega_I. \tag{2.2}$$

A typical spectrum of the scattered ligh is represented in Fig. 2.1. As explained in section 1.3, the energy $\hbar\omega_{\vec{q}}$ is quantized and represents the energy of the phonon which represents a quantum of vibration (a normal mode) of the lattice.

This brief introduction gives a clue that we will need Quantum Mechanics to get a broad understanding of the Raman effect. As a matter of fact we will need the full machinery of time dependent perturbation theory to describe the Raman scattering process. Thus the main goal of this chapter is to provide a complete discussion of Raman scattering through the Quantum Mechanics point of view.

2.1.1 The cross section

Since Raman is a light-scattering process we must start by defining a central parameter in any scattering process in physics, which is the scattering cross section σ. For that, we will keep our focus to the Stokes component of the scattered light. The scattering cross section is a measure of the likelihood of a scattering event to occur, and is the main meeting point of experiment with theory [33]. In the scope of ligh-scattering phenomena, the cross section is defined as the rate at which energy is removed from an incident photon beam by the scattering medium, divided by the rate at which energy in the incident photon beam crosses a unit area perpendicular to its propagation direction [34]. It has units of area and the bigger σ is, the greater is the probability of a scattering event to occur.

In that sense

$$\sigma = \frac{\hbar\omega_I}{\tau \bar{I}_I}. \tag{2.3}$$

Here $\bar{I}_I$ is the surface power density with units of energy/ (time $\times$ area), ω_I is the angular frequency of the incident beam, and $1/\tau$ is the transition rate at which the whole scattering process take place. Therefore the product of these last two quantities gives the rate at which energy (carried by the photons with frequency ω_I) is removed by the system by creation of phonons. The quantity $\frac{1}{\tau}$ is a fundamental parameter in order to understand the Raman Intensities and it can be theoretically obtained via Time Dependent Perturbation Theory.

2.1.2 The scattering process

As explained in Sec. 2.1, in order to obtain a theoretical expression for σ we need to calculate the transition rate, $1/\tau$. The transition is caused by an interaction of matter with an external field. Since the external fields are sufficiently weak and have an explicit time dependence, their effect can be handled within the framework of time-dependent perturbation theory. The unperturbed wavefunctions will serve as a basis for describing the perturbed system. The calculation will be carried out for a one-phonon Stokes process.

Let us define our system as the scattering medium plus the radiation interacting with it. The Hamiltonian of the whole system is then composed of four parts [35]:

$$\mathscr{H} = \mathscr{H}_m + \mathscr{H}_r + \mathscr{H}_{er} + \mathscr{H}_{ep}. \tag{2.4}$$

Here $\mathscr{H}_m$ is the scattering medium Hamiltonian, $\mathscr{H}_r$ is the radiation field Hamiltonian, $\mathscr{H}_{er}$ is the electron-radiation interaction Hamiltonian, and $\mathscr{H}_{ep}$ is the electron-phonon interaction Hamiltonian. The form of $\mathscr{H}_{ep}$ was detailed in Sec. 1.4 and for our purposes it is sufficient to say that $\mathscr{H}_{er}$ is equal to the electric-dipole interaction Hamiltonian. The total Hamiltonian can then be written as:

$$\mathscr{H} = \mathscr{H}_0 + \mathscr{H}_I, \tag{2.5}$$

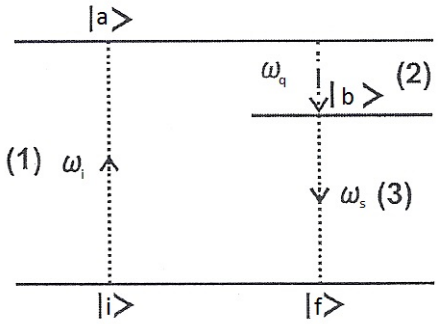

Figure 2.2: Schematics showing the one-phonon Stokes Raman process in a medium. The upwards arrow $|i\rangle \rightarrow |a\rangle$ represents the absorption of a photon with frequency ω_i and the creation of an electron-hole pair through an electron-radiation interaction. The downward arrow $|a\rangle \rightarrow |b\rangle$ represents the electron losing energy to the lattice by creation of a phonon of frequency $\omega_{\vec{q}}$ through an electron-phonon interaction. The downward arrow $|b\rangle \rightarrow |f\rangle$ represents the emission of a photon with angular frequency ω_s by recombination of the electron-hole pair through an electron-photon interaction. The horizontal lines do not correspond to the electronic levels. Figure adapted from [36]

where $\mathscr{H}_0 = \mathscr{H}_m + \mathscr{H}_r$ is the unperturbed Hamiltonian, and $\mathscr{H}_I = \mathscr{H}_{er} + \mathscr{H}_{ep}$ is the Hamiltonian of the perturbation.

Let us define the initial state $|i\rangle$ as the state before the scattering process take place. This state, as well as every other intermediate state is an eigenstate of $\mathscr{H}_0$ and is specified by: the number of the incident and scattered photons with frequencies ω_i and ω_s, respectively; the number of phonons and the electronic wavefunction. In the initial state $|i\rangle$, there are $n_i(\omega_i)$ and $n_i(\omega_s)$ incident and scattered photons at the frequencies ω_i and ω_s respectively, $n_{\vec{q}}$ phonons, and we can designate the state function of the electron as ψ_i. The state $|i\rangle$ can be represented as:

$$|i\rangle = |n_i(\omega_i), n_s(\omega_s), n_{\vec{q}}, \psi_i\rangle \,. \tag{2.6}$$

The final state $|f\rangle$ has $n_i(\omega_i)-1$ incident photons, $n_s(\omega_s)+1$ scattered photons and $n_{\vec{q}}+1$ phonons, while the electron state remains unchanged, $\psi_i = \psi_f$. Since the electrons remain unchanged, at first sight one could reason that this scattering process does not involve electrons at all, and that the photons are directly scattered by phonons through a photon-phonon interaction Hamiltonian. The strength of this interaction, however, is very weak unless the photons and phonons have a comparable frequency [34]. When visible light is used to excite Raman scattering, the photons couple to electrons via the electron-radiation interaction Hamiltonian $\mathscr{H}_{er}$. The scattering then proceeds in three steps:

1. The incident photon excites the medium into an intermediate state $|a\rangle$ via $\mathscr{H}_{er}$ and creates an electron-hole pair.

2. The electron-hole pair is scattered into other intermediate state $|b\rangle$ by creating a phonon via $\mathscr{H}_{ep}$.

3. The electron-hole pair in $|b\rangle$ recombines via $\mathscr{H}_{er}$ with the emission of the scattered photon.

The intermediate states $|a\rangle$ and $|b\rangle$ are in principle virtual states. In perturbation theory, virtual states are described by a linear combination of the electron eigenstates of the system with a large energy uncertainty and a small lifetime to compensate for the uncertainty principle [28]. If any of the intermediate states happens to be a real electronic state, then we have the phenomena of resonance.

Thus electrons mediate the Raman scattering of light by phonons, although they remain unchanged after the process. Since the transitions involving electrons are virtual, they do not have to conserve energy, although they still have to conserve wave vectors [34]. The whole aforementioned process is illustrated in Fig. 2.2, and the four states involved are described as:

$$\begin{aligned} |i\rangle &= |n_i(\omega_I), n_s(\omega_s), n_{\vec{q}}, \psi_i\rangle \\ |a\rangle &= |n_i(\omega_I) - 1, n_s(\omega_s), n_{\vec{q}}, \psi_a\rangle \\ |b\rangle &= |n_i(\omega_I) - 1, n_s(\omega_s), n_{\vec{q}} + 1, \psi_b\rangle \\ |f\rangle &= |n_i(\omega_I) - 1, n_s(\omega_s) + 1, n_{\vec{q}} + 1, \psi_i\rangle\,. \end{aligned} \tag{2.7}$$

The respective eigenenergies are

$$\begin{aligned} \mathscr{H}_0\,|i\rangle &= E_i\,|i\rangle = \left(n_i\hbar\omega_I + n_s\hbar\omega_s + n_{\vec{q}}\hbar\omega_{\vec{q}} + E_v\right)|i\rangle \\ \mathscr{H}_0\,|a\rangle &= E_a\,|a\rangle = \left((n_i - 1)\hbar\omega_I + n_s\hbar\omega_s + n_{\vec{q}}\hbar\omega_{\vec{q}} + E_c^a\right)|a\rangle \\ \mathscr{H}_0\,|b\rangle &= E_b\,|b\rangle = \left((n_i - 1)\hbar\omega_I + n_s\hbar\omega_s + (n_{\vec{q}} + 1)\hbar\omega_{\vec{q}} + E_c^b\right)|b\rangle \\ \mathscr{H}_0\,|f\rangle &= E_f\,|f\rangle = \left((n_i - 1)\hbar\omega_I + (n_s + 1)\hbar\omega_s + (n_{\vec{q}} + 1)\hbar\omega_{\vec{q}} + E_v\right)|f\rangle\,, \end{aligned} \tag{2.8}$$

where E_v and E_c are the energies of the electron in the valence and conduction bands respectively. Now that we have a clear picture of the whole scattering process with all associated state

vectors, energies and Hamiltonians specified, we are ready to calculate the transition rate $1/\tau$ using the Schrödinger representation.

2.1.3 Time-dependent Perturbation Theory

We start our analysis by considering our system to be represented by a pure state $|\phi(t)\rangle$ at a time t, which can be determined by the action of the time evolution operator on the initial state $|\phi(t_0)\rangle$ at a time t_0, that is,

$$|\phi(t)\rangle = exp(-i\mathscr{H}(t-t_0)/\hbar)\,|\phi(t_0)\rangle\,, \tag{2.9}$$

where $\mathscr{H}$ is given by Eq. 2.5. Our goal is to determine the probability of finding the system in a specific state $|\psi_f\rangle$ by performing a measurement at instant t. The state $|\psi_f\rangle$ is an eigenstate of $\mathscr{H}_0$ with energy $\hbar\omega_f$,

$$\mathscr{H}_0\,|\psi_f\rangle = \hbar\omega_f\,|\psi_f\rangle\,. \tag{2.10}$$

Since our system is represented by a pure state, the probability that a measurement at time t will find the system in state $|f\rangle$ is given by

$$|\,\langle f|\phi(t)\rangle\,|^2 = |\,\langle f|exp(-i\mathscr{H}(t-t_0)/\hbar)|\phi(t_0)\rangle\,|^2, \tag{2.11}$$

where $|\phi(t)\rangle$ is defined in Eq. 2.9. We then consider that at $t = t_0$, there is no perturbation, which is "turned on" after that instant. The presence of the perturbation term $\mathscr{H}_I$ in the Hamiltonian causes $|\,\langle f|\phi(t)\rangle\,|^2$ to differ in general from $|\,\langle f|\phi(t_0)\rangle\,|^2$. The difference is physically described as being due to the occurrence of transitions induced by the interaction of radiation with the medium during the time interval $t - t_0$.

Let us consider that at t_0 the system is at state $|i\rangle$. The probability of transition from state $|i\rangle$ to state $|f\rangle$ is then

$$|\langle f|exp(-i\mathscr{H}(t-t_0)/\hbar)|i\rangle|^2 \tag{2.12}$$

The transition rate from state $|i\rangle$ to state $|f\rangle$ is equal to the time derivative of this probability. Experimentally, transitions to a range of final states are observed simultaneously, therefore it is appropriate to define the transition rate as [34]:

$$\frac{1}{\tau} = \frac{d}{dt}\sum_f |\langle f|exp(-i\mathscr{H}(t-t_0)/\hbar)|i\rangle|^2 \tag{2.13}$$

where the sum is taken over all possible eigenstates $|f\rangle$.This is our central equation, but the way it is presented in (2.13) is not useful for calculations. It can be made more useful if we expand the time-evolution operator $\exp(-i\mathscr{H}(t-t_0)/\hbar)$ in a series of powers of the matrix elements of $\mathscr{H}_I$. The matrix elements of the perturbed Hamiltonian,(or the energies involved), are small compared to the energies of the unperturbed system, therefore the series expansion of the transition rate can be expected to converge rapidly. However this expansion is not entirely straightforward because

$$exp(-i\mathscr{H}(t-t_0)/\hbar) \neq exp(-i\mathscr{H}_0(t-t_0)/\hbar)exp(-i\mathscr{H}_I(t-t_0)/\hbar) \tag{2.14}$$

and the reason is that $\mathscr{H}_0$ and $\mathscr{H}_I$ do not commute [34](remember that the argument of the exponentials are operators, therefore the exponentials must be handled with care). This difficulty is overcome if we find a way to express $\exp(-i\mathscr{H}(t-t_0)/\hbar)$ in recursive way ,with the $\mathscr{H}$ operator appearing on both sides of the equality, so that the expansion can be performed via an iteration process. We start by the identity

$$exp(i\mathscr{H}_0 t/\hbar)\,\mathscr{H}_1 exp(-i\mathscr{H}t/\hbar) = i\hbar\frac{d}{dt}\left[exp(i\mathscr{H}_0 t/\hbar)\,exp(-i\mathscr{H}t/\hbar)\right]. \tag{2.15}$$

The identity is easily proved by explicit differentiation on the right side and with use of Equation (2.5). There is a slight trick here that should be elucidated. When differentiating the exponential

whose argument is an operator, one may place the argument of the exponential either to the right or to the left. Here is in an example:

$$\frac{d}{dt}exp(i\mathscr{H}t/\hbar) = \frac{i}{\hbar}exp(i\mathscr{H}t/\hbar)\mathscr{H} = \frac{i}{\hbar}\mathscr{H}\,exp(i\mathscr{H}t/\hbar). \tag{2.16}$$

And the reason is that the operators $\mathscr{H}$ and $exp(i\mathscr{H}t/\hbar)$ do commute. Therefore one can place the argument according to their convenience. Integrating both sides of Eq. 2.15 with respect to time yields

$$\begin{aligned}&\int_{t_0}^{t} exp(i\mathscr{H}_0 t_1/\hbar)\mathscr{H}_I exp(-i\mathscr{H}t_1/\hbar)dt_1 \\ &=i\hbar\left[exp(i\mathscr{H}_0 t/\hbar)exp(-i\mathscr{H}t/\hbar) - exp(i\mathscr{H}_0 t_0/\hbar)exp(-i\mathscr{H}t_0/\hbar)\right],\end{aligned} \tag{2.17}$$

which can be rearranged in order to express $\exp\left(-i\mathscr{H}(t-t_0)/\hbar\right)$ in a recursive way as

$$\begin{aligned}exp\left(-i\mathscr{H}t/\hbar\right) = exp\left(-i\mathscr{H}_0 t/\hbar\right)\Big[&exp\left(i\mathscr{H}_0 t_0/\hbar\right)exp\left(i\mathscr{H}t_0/\hbar\right) \\ &-\frac{i}{\hbar}\int_{t_0}^{t} exp\left(i\mathscr{H}_0 t_1/\hbar\right)\mathscr{H}_I \exp\left(-i\mathscr{H}t_1/\hbar\right)dt_1\Big].\end{aligned} \tag{2.18}$$

Notice that, in Eq. 2.18 the time-evolution operator has a dependence on t_0. However, under steady-state conditions, the transition rate given by Eq. 2.13 is expected to be independent of both t and t_0 [34]. Thus, in order to ensure that the system has reached the steady state condition by the time t, we assume that t_0 is a time in the infinitely remote past, $t_0 \to -\infty$. Now if we consider that $\mathscr{H}_I$ was "turned on" at time t_0, the sudden application of the interaction to the system could lead to transient effects that would increase the complexity of the problem. We can solve this by inserting a factor $exp(\varepsilon t)$ in the perturbed Hamiltonian $\mathscr{H}_I$,

$$\mathscr{H}_I \to \mathscr{H}_I exp(\varepsilon t), \tag{2.19}$$

where ε is a small parameter that is made to tend to zero in the final expressions for the transitions rates. With this substitution, instead of an "off-on" interaction, we consider it as having been gradually built up, starting from $t = -\infty$. This will avoid transient effects.

Substituting (2.19) into (2.18) and noting that $\mathscr{H}_I$ is now zero at $t_0 \to -\infty$, Eq. 2.18 becomes

$$exp\,(-i\mathscr{H}t/\hbar) = exp\,(-i\mathscr{H}_0 t/\hbar)$$
$$\left[1 - \frac{i}{\hbar}\int_{-\infty}^{t} exp\,(i\mathscr{H}_0 t_1/\hbar)\,\mathscr{H}_I exp(\varepsilon t_1)\,exp\,(-i\mathscr{H}t_1/\hbar)\,dt_1\right]. \tag{2.20}$$

Next, the right-hand side of Eq. 2.20 can be developed as a power series in $\mathscr{H}_I$ by iteration. The process goes as follows; we set an initial value for $\mathscr{H}$ on the argument of exponential on the right side of Eq. 2.20, then after integration we will obtain a new expression for $exp\,(-i\mathscr{H}t/\hbar)$. We then insert this new expression into the right side of Eq. 2.20 again to obtain a new expression for the time-evolution operator and so on. In this way we are able to obtain a series expansion in ascending orders of $\mathscr{H}_I$ that will be used to calculate $1/\tau$. The scattering process we described in Sec. 2.1.2 is a third-order process, therefore we are interested in the third-order term of the expansion (third order perturbation). The process is simple but laborious and we are going to fully develop it, from the zeroth order up to the third order. We just need the first term, (the zeroth order), to start the iteration and obtain expressions for higher-order terms.

Thus far everything we did is rigorous. The approximation comes when we set an expression for the zeroth order term as follows.

Zeroth order

The zeroth order in $\mathscr{H}_I$ is obtained by setting $\mathscr{H} = \mathscr{H}_0$, yielding

$$exp(-i\mathscr{H}t/\hbar) = exp(-i\mathscr{H}_0 t/\hbar) \tag{2.21}$$

This term leads to a matrix element

$$\langle f|exp(-i\mathscr{H}t/\hbar)|i\rangle = \langle f|exp(-i\mathscr{H}_0 t/\hbar)|i\rangle = exp(-i\omega_0 t)\,\langle f|i\rangle = 0, \tag{2.22}$$

since, as discussed in Sec. 2.1.2, $|f\rangle$ and $|i\rangle$ are distinct eigenstates. Therefore the zero-order contribution to the transition rate is null.

First order

The first order term in $\mathscr{H}_I$ is obtained by replacing the zero-order term (2.21) with $exp\,(-i\mathscr{H}t/\hbar)$ in the right hand side of Eq. 2.20.

The expansion up to first order is now

$$\begin{aligned}&\exp(-i\mathscr{H}t/\hbar) = \text{zero-order term+}\\&-\frac{i}{\hbar}\exp(-i\mathscr{H}_0 t/\hbar)\int_{-\infty}^{t} exp\,(i\mathscr{H}_0 t_1/\hbar)\,\mathscr{H}_I \exp(\varepsilon t_1)\exp(-i\mathscr{H}_0 t_1/\hbar)\,dt_1.\end{aligned} \tag{2.23}$$

The contribution of the first order term to the matrix element is obtained by "sandwiching" the second term of Eq. 2.23 between states $|f\rangle$ and $|i\rangle$, yielding:

$$\begin{aligned}\langle f|-\frac{i}{\hbar}\exp(-i\mathscr{H}_0 t/\hbar)\int_{-\infty}^{t}\exp(i\mathscr{H}_0 t_1/\hbar)\,\mathscr{H}_I\exp(\varepsilon t_1)\exp(-i\mathscr{H}_0 t_1/\hbar)\,dt_1|i\rangle&\\ = -\frac{i}{\hbar}\exp(-i\omega_f t_1/\hbar)\langle f|\mathscr{H}_I|i\rangle\int_{-\infty}^{t}\exp(i\omega t_1+\varepsilon t_1-i\omega_i t_1)dt_1&\\ = \frac{\langle f|\mathscr{H}_I|i\rangle}{\hbar}\frac{\exp(\varepsilon t-i\omega_i t)}{(i\varepsilon+(\omega_i-\omega_f))}.&\end{aligned} \tag{2.24}$$

Here the $\exp(-i\mathscr{H}_0 t/\hbar)$ operator has acted on the ket $|i\rangle$, and $\exp(i\mathscr{H}_0 t/\hbar)$ has acted on the bra $\langle f|$, , both interactions taking place inside the integral. Outside the integral, we have the action of the $\exp(-i\mathscr{H}_0 t/\hbar)$ operator upon the bra $\langle f|$. The transition rate, according to Eq. 2.13 is

$$\begin{aligned}\frac{1}{\tau} &= \frac{d}{dt}\sum_f \frac{|\langle f|\mathscr{H}_I|i\rangle|^2}{\hbar^2}\frac{\exp(2\varepsilon t)}{(\omega_i-\omega_f)^2+\varepsilon^2}\\ &= \frac{2}{\hbar^2}\sum_f |\langle f|\mathscr{H}_I|i\rangle|^2\frac{\varepsilon\exp(2\varepsilon t)}{(\omega_i-\omega_f)^2+\varepsilon^2}.\end{aligned} \tag{2.25}$$

Now as planned before, we take the limit of $\varepsilon \to 0$. The exponential $\exp(2\varepsilon t)$ tends to unity and the limit of the remaining term in ε has the form of the delta distribution [34]:

$$\lim_{\varepsilon\to 0}\frac{\varepsilon\exp(2\varepsilon t)}{(\omega_i-\omega_f)^2+\varepsilon^2} = \pi\delta(\omega_i-\omega_f). \tag{2.26}$$

The final expression is then

$$\frac{1}{\tau} = \frac{2\pi}{\hbar^2}\sum_f |\langle f|\mathscr{H}_I|i\rangle|^2\delta(\omega_i-\omega_f), \tag{2.27}$$

broadly known as the Fermi's golden rule, which applies only to first-order radiative processes.

Second order

The second order term is obtained by substituting the first order expansion of $\exp(-i\mathscr{H}t/\hbar)$ (2.23) in (2.20) and replacing t with t_1 and t_1 with t_2 in the right-hand side of Eq. 2.20. The expansion up to second order is then

$$\begin{aligned}&\exp(-i\mathscr{H}t/\hbar) = \text{zero-order term} + \text{first-order term}\\ &-\frac{1}{\hbar^2}\exp(-i\mathscr{H}_0 t/\hbar)\int_{-\infty}^{t}\exp(i\mathscr{H}_0 t_1/\hbar)\mathscr{H}_I\exp(\varepsilon t_1)\exp(-i\mathscr{H}_0 t_1/\hbar)dt_1\\ &\int_{-\infty}^{t_1}\exp(\varepsilon t_2)\exp(i\mathscr{H}_0 t_2/\hbar)\mathscr{H}_I\exp(-i\mathscr{H}_0 t_2/\hbar)dt_2\end{aligned} \tag{2.28}$$

The contribution of the second-order term to the matrix element is

$$\begin{aligned}&-\langle f|\frac{1}{\hbar^2}\exp(-i\mathscr{H}_0 t/\hbar)\int_{-\infty}^{t}\int_{-\infty}^{t_1}\exp(i\mathscr{H}_0 t_1/\hbar)\mathscr{H}_I\exp(\varepsilon t_1)\exp(-i\mathscr{H}_0 t_1/\hbar)\\ &\exp(i\mathscr{H}_0 t_2/\hbar)\exp(\varepsilon t_2)\mathscr{H}_I\exp(-i\mathscr{H}_0 t_2/\hbar)dt_2 dt_1\,|i\rangle\,.\end{aligned} \tag{2.29}$$

In order to reduce Eq. 2.29 to a more compact form we make use of the closure theorem

$$\sum_a |a\rangle\langle a| = \mathbb{I}, \tag{2.30}$$

where the summation runs over all eigenstates of $\mathscr{H}_0$. The Identity must then be inserted between the two $\mathscr{H}_I$ operators in Eq. 2.29

$$\begin{aligned}&-\sum_a\langle f|\frac{1}{\hbar^2}\exp(-i\mathscr{H}_0 t/\hbar)\int_{-\infty}^{t}\int_{-\infty}^{t_1}\exp(i\mathscr{H}_0 t_1/\hbar)\mathscr{H}_I\exp(\varepsilon t_1)\exp(-i\mathscr{H}_0 t_1/\hbar)\\ &|a\rangle\langle a|\exp(i\mathscr{H}_0 t_2/\hbar)\exp(\varepsilon t_2)\mathscr{H}_I\exp(-i\mathscr{H}_0 t_2/\hbar)dt_2 dt_1\,|i\rangle\,,\end{aligned} \tag{2.31}$$

where the summation was interchanged with the integrals. The matrix element can now be evaluated, paying close attention to whether the operator is acting on a bra or on a ket:

$$
\begin{aligned}
&\text{matrix element} = -\frac{1}{\hbar^2}\sum_a \exp(-i\omega_f t)\,\langle f|\mathscr{H}_I|a\rangle\,\langle a|\mathscr{H}_I|i\rangle \\
&\int_{-\infty}^{t}\int_{-\infty}^{t_1} \exp(i\omega_f t_1 + \varepsilon_1 - i\omega_a(t_1 - t_2) + \varepsilon t_2 - i\omega_i t_2)dt_2 dt_1 \\
&\quad = \sum_a \frac{\langle f|\mathscr{H}_I|a\rangle\,\langle a|\mathscr{H}_I|i\rangle}{\hbar^2}\,\frac{\exp(2\varepsilon t - i\omega_i t)(-i)}{(\omega_i - \omega_a + i\varepsilon)(\omega_i - \omega_f) + 2\varepsilon i}.
\end{aligned}
\tag{2.32}
$$

Since ε is an arbitrary small quantity, we are allowed to make the substitution $2\varepsilon \to \varepsilon$ in Eq. 2.32. The transition rate becomes

$$
\begin{aligned}
\frac{1}{\tau} &= \frac{d}{dt}\sum_f \left|\sum_a \frac{\langle f|\mathscr{H}_I|a\rangle\,\langle a|\mathscr{H}_I|i\rangle}{(\omega_i - \omega_a + i\varepsilon/2)}\right|^2 \frac{\exp(2\varepsilon t)}{(\omega_i - \omega_f)^2 + \varepsilon^2} \\
&= \frac{2}{\hbar^4}\sum_f \left|\sum_a \frac{\langle f|\mathscr{H}_I|a\rangle\,\langle a|\mathscr{H}_I|i\rangle}{(\omega_i - \omega_a + i\varepsilon/2)}\right|^2 \frac{\varepsilon\exp(2\varepsilon t)}{(\omega_i - \omega_f)^2 + \varepsilon^2}.
\end{aligned}
\tag{2.33}
$$

The quantity outside of the squared modulus is the same as the calculated for the first-order contribution and by taking the $\varepsilon \to 0$ limit we will get the Dirac delta distribution from it. The term $i\varepsilon/2$ in the denominator should be kept as a damping term, which becomes important for those cases where $\omega_i = \omega_a$ (resonance). For simplicity ε is going to be redefined as $\varepsilon/2 \to \varepsilon$.

The transition rate correct to second order is

$$
\frac{1}{\tau} = \frac{2\pi}{\hbar^4}\sum_f \left|\sum_a \frac{\langle f|\mathscr{H}_I|a\rangle\,\langle a|\mathscr{H}_I|i\rangle}{(\omega_i - \omega_a + i\varepsilon)}\right|^2 \delta(\omega_i - \omega_f). \tag{2.34}
$$

Third order

Finally, for the third order term we must substitute the second-order expansion of $\exp(-i\mathscr{H}t/\hbar)$ (2.28) in (2.20), replacing t with t_1, t_1 with t_2, and t_2 with t_3 in the right-hand side of Eq. 2.20 to have

$$
\begin{aligned}
&\exp(-i\mathscr{H}t/\hbar) = \text{zero-order} + \text{first-order term} + \text{second-order term} \\
&+ \frac{i}{\hbar^3}\exp(-i\mathscr{H}_0 t/\hbar)\int_{-\infty}^{t}\exp(i\mathscr{H}_0 t_1/\hbar)\mathscr{H}_I\exp(\varepsilon t_1)\exp(-i\mathscr{H}_0 t_1/\hbar) \\
&\int_{-\infty}^{t_1}\exp(i\mathscr{H}_0 t_2/\hbar)\mathscr{H}_I\exp(\varepsilon t_2)\exp(-i\mathscr{H}_0 t_2/\hbar)\int_{-\infty}^{t_2}\exp(i\mathscr{H}_0 t_3/\hbar)\mathscr{H}_I \\
&\exp(\varepsilon t_3)\exp(-i\mathscr{H}_0 t_3/\hbar)dt_3 dt_2 dt_1 .
\end{aligned}
\tag{2.35}
$$

In order to obtain the contribution of the third-order term to the matrix element we are going to use the closure theorem again, but now the Identity is going to be inserted twice, between each pair of the $\mathscr{H}_I$ operators.

$$
\begin{aligned}
&\frac{i}{\hbar^3}\sum_{a,b}\langle f|\exp(-i\mathscr{H}_0 t/\hbar)\int_{-\infty}^{t_1}\int_{-\infty}^{t_2}\int_{-\infty}^{t_3}\exp(i\mathscr{H}_0 t/\hbar)\mathscr{H}_I|b\rangle\langle b|\exp(\varepsilon t_1) \\
&\exp(-i\mathscr{H}_0(t_1-t_2)/\hbar)\mathscr{H}_I|a\rangle\langle a|\exp(\varepsilon t_2)\exp(-i\mathscr{H}_0(t_2-t_3)/\hbar)\mathscr{H}_I \\
&\exp(\varepsilon t_3)\exp(-i\mathscr{H}_0 t_3/\hbar)|i\rangle\, dt_3 dt_2 dt_1 .
\end{aligned}
\tag{2.36}
$$

Again, we should take great care on whether the operator acts on a ket or a bra, and after performing these operations we get

$$
\begin{aligned}
&\sum_{a,b}\exp(-i\omega_f t/\hbar)\frac{\langle f|\mathscr{H}_I|b\rangle\langle b|\mathscr{H}_I|a\rangle\langle a|\mathscr{H}_I|i\rangle\,(i)}{\hbar^3}\int_{-\infty}^{t_1}\int_{-\infty}^{t_2}\int_{-\infty}^{t_3}\exp\Big(i\omega_f t_1 \\
&+\epsilon t_1 - i\omega_b(t_1-t_2) + \epsilon t_2 - i\omega_a(t_2-t_3) + \epsilon t_3 - i\omega_i t_3\Big)dt_3 dt_2 dt_1 \\
&= \sum_{a,b}\exp(-i\omega_f t/\hbar)\frac{\langle f|\mathscr{H}_I|b\rangle\langle b|\mathscr{H}_I|a\rangle\langle a|\mathscr{H}_I|i\rangle}{\hbar^3}\frac{i\exp(3\varepsilon t - i\omega_i t)}{(i[\omega_a-\omega_i]+\varepsilon)} \\
&\frac{1}{(i[\omega_b-\omega_i]+2\varepsilon)(i[\omega_f-\omega_i]+3\varepsilon)}.
\end{aligned}
\tag{2.37}
$$

Next, we substitute $3\varepsilon \to \varepsilon$ to get the expression for the transition probability (2.12) corrected to third-order

$$
\begin{aligned}
&\sum_f |\langle f|\exp(-i\mathscr{H}t/\hbar)|i\rangle|^2 \\
&= \sum_f\left|\sum_{a,b}\frac{\langle f|\mathscr{H}_I|b\rangle\langle b|\mathscr{H}_I|a\rangle\langle a|\mathscr{H}_I|i\rangle}{(\omega_i-\omega_a+i\varepsilon/3)(\omega_i-\omega_b+i2\varepsilon/3)}\right|^2\frac{\exp(2\varepsilon t)}{(\omega_i-\omega_f)^2+\varepsilon^2}.
\end{aligned}
\tag{2.38}
$$

The transition rate (2.13) is

$$\begin{aligned}\frac{1}{\tau} &= \frac{d}{dt}\sum_f |\langle f|\exp(-i\mathscr{H}t/\hbar)|i\rangle|^2 \\ &= \sum_f \left|\sum_{a,b}\frac{\langle f|\mathscr{H}_I|b\rangle\langle b|\mathscr{H}_I|a\rangle\langle a|\mathscr{H}_I|i\rangle}{(\omega_i-\omega_a+i\varepsilon/3)(\omega_i-\omega_b+i2\varepsilon/3)}\right|^2 \frac{2\exp(2\varepsilon t)}{(\omega_i-\omega_f)^2+\varepsilon^2}.\end{aligned} \tag{2.39}$$

If we take the limit as $\varepsilon \to 0$, keeping the damping terms, we have

$$\frac{1}{\tau} = \sum_f \frac{2\pi}{\hbar^2}\left|\sum_{a,b}\frac{\langle f|\mathscr{H}_I|b\rangle\langle b|\mathscr{H}_I|a\rangle\langle a|\mathscr{H}_I|i\rangle}{(\omega_i-\omega_a+i\varepsilon_1)(\omega_i-\omega_b+i\varepsilon_2)\hbar^2}\right|^2 \delta(\omega_i-\omega_f). \tag{2.40}$$

We can also express Eq. (2.40) in terms of the energy using the relation $E = \hbar\omega$:

$$\frac{1}{\tau} = \sum_f \frac{2\pi}{\hbar^2}\left|\sum_{a,b}\frac{\langle f|\mathscr{H}_I|b\rangle\langle b|\mathscr{H}_I|a\rangle\langle a|\mathscr{H}_I|i\rangle}{(E_i-E_a+i\varepsilon_1)(E_i-E_b+i\varepsilon_2)}\right|^2 \delta(E_i-E_f). \tag{2.41}$$

It is clear from Eq. 2.41 that energy must be conserved at the end of the process, due to the presence of the Diract delta distribution at the right side of the square modulus. Next, if we replace $\mathscr{H}_I$ with $\mathscr{H}_{er} + \mathscr{H}_{ep}$ we get

$$\begin{aligned}\langle a|\mathscr{H}_I|i\rangle &= \langle a|\mathscr{H}_{er}|i\rangle + \cancelto{0}{\langle a|\mathscr{H}_{ep}|i\rangle} \\ \langle b|\mathscr{H}_I|a\rangle &= \cancelto{0}{\langle b|\mathscr{H}_{er}|a\rangle} + \langle b|\mathscr{H}_{ep}|a\rangle \\ \langle f|\mathscr{H}_I|b\rangle &= \langle f|\mathscr{H}_{er}|b\rangle + \cancelto{0}{\langle f|\mathscr{H}_{ep}|b\rangle}.\end{aligned} \tag{2.42}$$

Substituting these matrix elements into Eq. 2.41 yields

$$\frac{1}{\tau} = \sum_f \frac{2\pi}{\hbar^2}\left|\sum_{a,b}\frac{\langle f|\mathscr{H}_{er}|b\rangle\langle b|\mathscr{H}_{ep}|a\rangle\langle a|\mathscr{H}_{er}|i\rangle}{(E_i-E_a+i\varepsilon_1)(E_i-E_b+i\varepsilon_2)}\right|^2 \delta(E_i-E_f). \tag{2.43}$$

The energy differences in the denominator can be evaluated with the eigenenergies given in (2.8) as

$$\begin{aligned}(E_i - E_a) &= \hbar\omega_I + E_v - E_c^a = \hbar\omega_I - \hbar\omega_{eh} \\ (E_i - E_b) &= \hbar\omega_I - \hbar\omega_{\vec{q}} + E_v - E_c^b = \hbar\omega_I - (\hbar\omega_{\vec{q}} + \hbar\omega_{eh}) \\ (E_i - E_f) &= \hbar\omega_I - (\hbar\omega_s + \hbar\omega_q)\end{aligned} \tag{2.44}$$

where $\hbar\omega_{eh}$ is the energy required to create the electron-hole pair, which is equal to the difference between the energy of the electron in the conduction and the valence bands. We can then rewrite Eq. 2.43 using the results of (2.44) and insert the result in Eq. (2.3) to get the cross-section:

$$\sigma = \frac{\hbar\omega_I}{I_0}\sum_f \frac{2\pi}{\hbar^2}\left|\sum_{a,b}\frac{\langle f|\mathscr{H}_{er}|b\rangle\langle b|\mathscr{H}_{ep}|a\rangle\langle a|\mathscr{H}_{er}|i\rangle}{(\hbar\omega_I - \hbar\omega_{eh} + i\varepsilon_1)(\hbar\omega_I - (\hbar\omega_{\vec{q}} + \hbar\omega_{eh}) + i\varepsilon_2)}\right|^2 \delta[\hbar\omega_I - (\hbar\omega_s + \hbar\omega_q)]. \tag{2.45}$$

Eq. 2.45 is our final expression for the cross section of a one-phonon Raman Stokes process, which is described as a third-order process in time-dependent perturbation theory. We could extend this procedure for scattering processes of higher orders, such as the scattering of electrons by two phonons, or one phonon and one defect, both of which are fourth-order processes. In that case, after doing all the calculation, we will get the expression for the cross section as

$$\sigma = \frac{\hbar\omega_I}{I_0}\sum_f \frac{2\pi}{\hbar^2}\left|\sum_{a,b,c}\frac{\langle f|\mathscr{H}_I|c\rangle\langle c|\mathscr{H}_I|b\rangle\langle b|\mathscr{H}_I|a\rangle\langle a|\mathscr{H}_I|i\rangle}{(E_i - E_a + i\varepsilon_1)(E_i - E_b + i\varepsilon_2)(E_i - E_c + i\varepsilon_3)}\right|^2 \delta(E_i - E_f). \tag{2.46}$$

2.1.4 Feynman diagrams for Raman scattering

In Secs. (2.1.2-2.1.3) we assumed a particular order of the events in the scattering process. However, one should take into account all possible sequences of events in order to calculate the transition rates correctly. Feynman diagrams are useful for keeping track of various processes that may occur in an inelastic scattering process that annihilates or creates an excitation [28]. The Feynman diagrams that describes one-phonon Raman Stokes scattering processes are represented in Fig. 2.3. The rules for drawing Feynman diagrams are [37]:

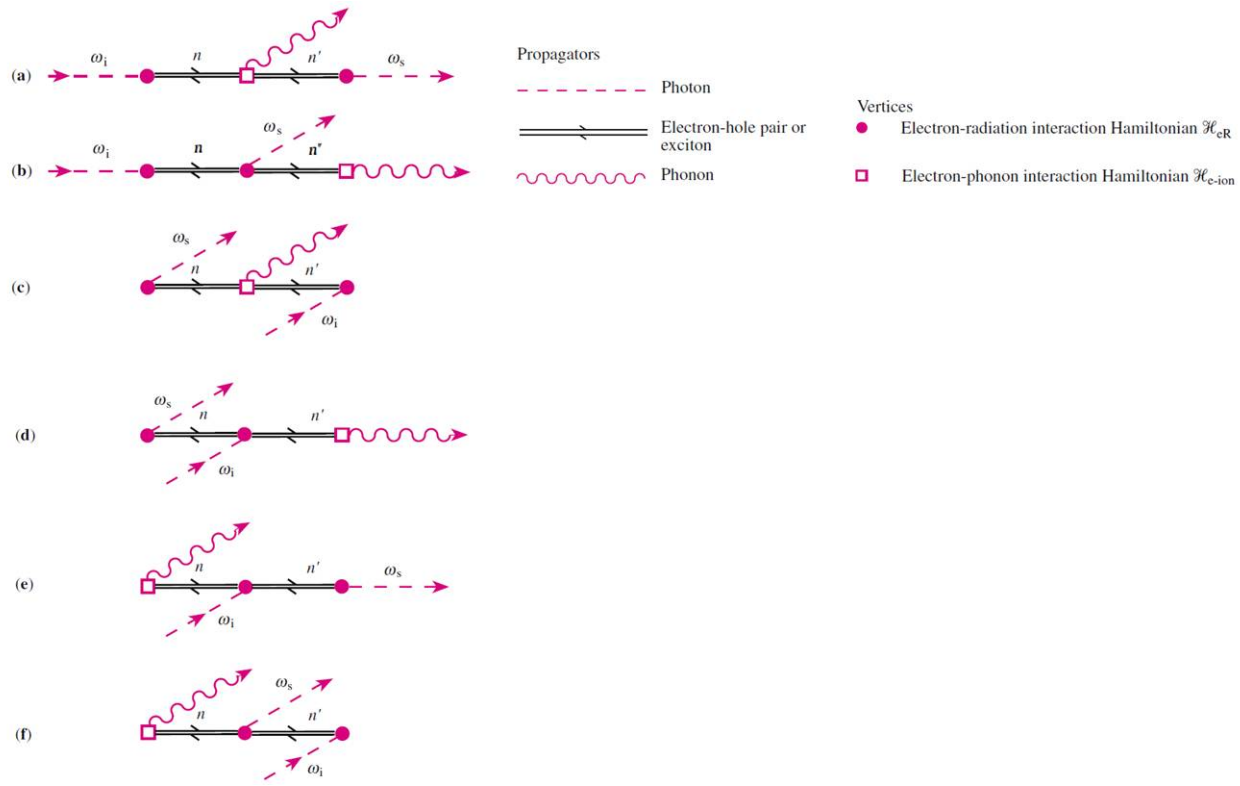

Figure 2.3: Feynman diagrams for the six possible processes that contribute to one-phonon Raman Stokes scattering. Figure adapted from [37].

- Excitations such as photons, phonons and electron-hole pairs are represented by lines(or propagators).These propagators can be labeled with properties of the excitations such as their wave vectors, frequencies, and polarizations.

- The interaction between two excitations is represented by an intersection of their propagators. This intersection is known as *vertex* and is sometimes highlighted by a symbol such as filled circle or an empty square which specifies the type of the interaction.

- Propagators are drawn with an arrow to indicate whether they are created or annihilated in an interaction. Arrows pointing toward a vertex represent excitations which are annihilated. Arrows pointing away from the vertex are created.

- When there are several interactions, they are always assumed to proceed sequentially from the left to the right as a function of time.

- Once a diagram has been drawn for a certain process, other possible process are derived by permuting the time order in which the vertices occur in the diagram.

The process described in previous sections is represented by Fig. 2.3 (*a*). Since there are three vertices representing the time ascending electron-radiation, electron-phonon and electron-radiation interactions, if we permute the time order of the events there will be six other possible process in total. The transition rate $1/\tau$ due to all six diagrams is obtained by adding the their individual contributions considering the order of the events:

$$
\begin{aligned}
\frac{1}{\tau} = \frac{2\pi}{\hbar}\Big| \sum_{a,b} & \frac{\langle f|\mathscr{H}_{er}(\omega_s)|b\rangle\langle b|\mathscr{H}_{ep}|a\rangle\langle a|\mathscr{H}_{er}(\omega_I)|i\rangle}{(\hbar\omega_I - \hbar\omega_{eh})(\hbar\omega_I - (\hbar\omega_{\vec{q}} + \hbar\omega_{eh}))} \\
& + \frac{\langle f|\mathscr{H}_{ep}|b\rangle\langle b|\mathscr{H}_{er}(\omega_s)|a\rangle\langle a|\mathscr{H}_{er}(\omega_I)|i\rangle}{(\hbar\omega_I - \hbar\omega_{eh})(\hbar\omega_I - (\hbar\omega_s + \hbar\omega_{eh}))} \\
& + \frac{\langle f|\mathscr{H}_{er}(\omega_I)|b\rangle\langle b|\mathscr{H}_{ep}|a\rangle\langle a|\mathscr{H}_{er}(\omega_s)|i\rangle}{(\hbar\omega_s - \hbar\omega_{eh})(-\hbar\omega_s - (\hbar\omega_{\vec{q}} + \hbar\omega_{eh}))} \\
& + \frac{\langle f|\mathscr{H}_{ep}|b\rangle\langle b|\mathscr{H}_{er}(\omega_I)|a\rangle\langle a|\mathscr{H}_{er}(\omega_s)|i\rangle}{(\hbar\omega_s - \hbar\omega_{eh})(-\hbar\omega_s + \hbar\omega_I - \hbar\omega_{eh})} \\
& + \frac{\langle f|\mathscr{H}_{ep}(\omega_s)|b\rangle\langle b|\mathscr{H}_{er}(\omega_I)|a\rangle\langle a|\mathscr{H}_{ep}|i\rangle}{(-\hbar\omega_{\vec{q}} - \hbar\omega_{eh})(-\hbar\omega_{\vec{q}} + (\hbar\omega_I - \hbar\omega_{eh}))} \\
& + \frac{\langle f|\mathscr{H}_{er}(\omega_I)|b\rangle\langle b|\mathscr{H}_{er}(\omega_s)|a\rangle\langle a|\mathscr{H}_{ep}|i\rangle}{(\hbar\omega_{\vec{q}} - \hbar\omega_{eh})(-\hbar\omega_{\vec{q}} - \hbar\omega_s - \hbar\omega_{eh})}\Big|^2 \\
& \delta(\hbar\omega_I - (\hbar\omega_s + \hbar\omega_q)).
\end{aligned}
\tag{2.47}
$$

When one ore more terms in the denominator of Eq. 2.47 vanishes, we have the phenomena of resonance which will be exploit in next Chapter.

Chapter 3

The G stretching mode in graphene

3.1 The G band

Chapter 2 gave us a broad understanding of the Raman process. From now on, we are going to apply this knowledge to interpret the Raman features of graphene spectrum. Figure 3.1 exhibits a typical spectrum of monolayer graphene. The two most intense features are the one-phonon first-order Raman G band at $\sim$ 1580 cm^{-1} and the two-phonon second-order $2D$ (G') band at $\sim$ 2700 cm^{-1}. Because the main results of this work are based on the analysis of the G band in the Raman spectra of double-layer graphene under high-pressure (Chapter 5), this Chapter is dedicated to this feature. It is important to point out that the Raman spectrum of the double layer graphene in this work is identical to that of a mono-layer (Fig. 3.1) since the two layers have no stacking order.

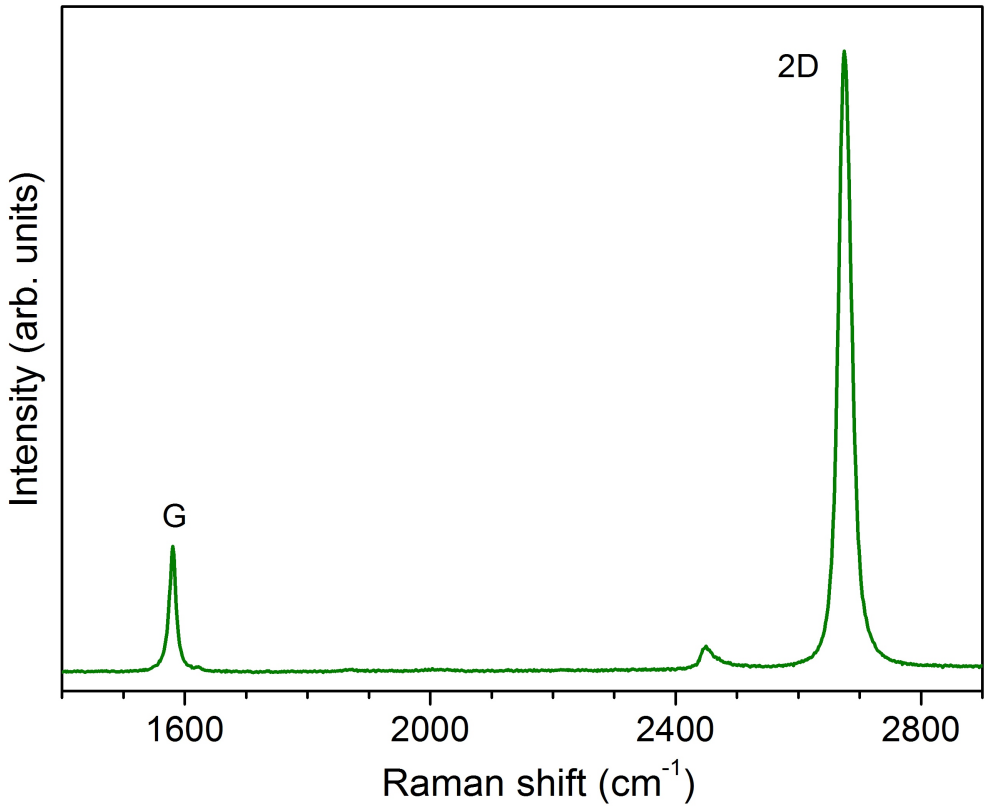

Figure 3.1: Raman spectrum of pristine mono-layer graphene using a 514.5 nm excitation laser line.

The process giving rise to the G band is described by third-order perturbation theory, as described in Sec. 2.1.2. The whole process is depicted in Fig. 3.2. It starts when the graphene system absorbs a photon with energy $E_I = \hbar\omega_I$ from the incident laser beam, creating an electron-hole pair, [Fig. 3.2(a)]. This is the first of three steps. Since the energy dispersion of the electrons is linear in the vicinity of K, there will always be resonant optical transitions between the valence (π) and conduction (π^*) bands. In order to keep momentum conservation, the sum of the electron and hole momenta should be equal to the incident photon momentum, $\vec{k_e} + \vec{k_h} = \vec{k}_{photon}$. However, since the incident photon momentum is much smaller than the electron momentum near K ($|\vec{k}_{photon}| \sim |\vec{k_e}| \times 10^{-4}$) we can assume that $\vec{k_e} \sim -\vec{k_h}$. This characterizes a vertical transition. The electron and hole are the small dark and white circles with wave vectors $\vec{k_0}$ and $-\vec{k_0}$, respectively, in Fig. 3.2 (a).

If we consider that the energy is zero around the Fermi level, the energy of the electrons and holes after the absorption of the incident photon are $E^c_{\vec{k_0}} = \hbar\omega_I/2$ and $E^v_{\vec{k_0}} = -\hbar\omega_I/2$, respectively, due to the symmetry of the electronic dispersion of the π electrons around the $K(K')$

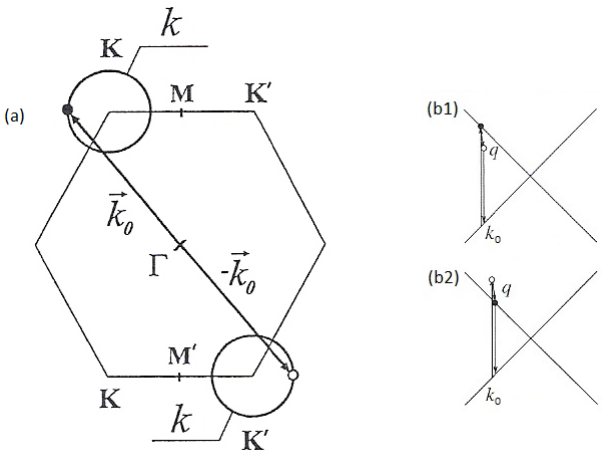

Figure 3.2: G Band scattering process.(a) Creation of the electron-hole pair. Figure adapted from [35]. (b1) Incident Resonance. Figure adapted from [28].(b2) Scattered Resonance. Figure adapted from [28].

point. The collection of all electrons and holes able to take part in this process form two circles (disregarding the trigonal warping effect) centered at the K and K' points respectively, with the radius given by $k = \hbar\omega_I/2A$ where $A = \sqrt{3}\gamma a/2$ is the slope of the π and π^* bands near the K and K' points [35].

In the second step of the process, the system in state $|a\rangle$ is scattered to a state $|b\rangle$ by the creation of a phonon with wave vector $\vec{q}_{phonon}$. The selection rule for this process is $\vec{q}_{phonon} \sim \vec{0}$. In the third (final) step, the electron then recombines with the hole by the emission of a photon. This process is represented by Fig. 3.2(b). Notice that the electronic transition between the valence and conduction bands can be in resonance with either the incident (b_1) or scattered (b_2) photon. In either case, one term in the denominator of Eq. 2.45 will diverge.

Figure 3.3 shows the bond-stretching vibration mode giving rise to the G band. This is a double-degenerated zone-center mode ($\vec{q}_{phonon} \sim 0$) with E_{2g} symmetry, occurring at the crossing point between the iTO and iLO branches (Gamma point) at $\sim 1580\,\mathrm{cm}^{-1}$ (see Fig. 1.10).

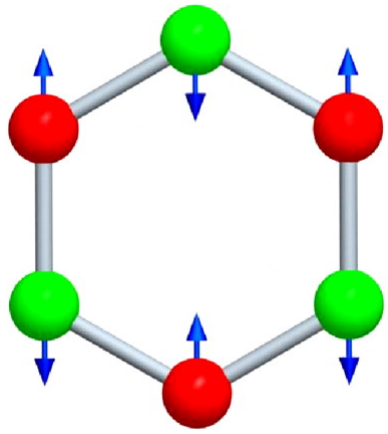

Figure 3.3: Bond stretching vibration mode giving rise to the G band in the Raman spectrum of graphene. Figure adapted from [38].

3.2 Perturbations to the G band

The strong covalent $C-C$ bonding and the small mass of the carbon atoms is the responsible for the relatively high Raman frequency of the G band in sp^2 carbons in comparison to other materials, and makes it possible to observe changes on its frequency and line shape under relatively weak perturbations [28]. The aim of this chapter is to study the effects of mechanical strain, a time-independent perturbation, and charge doping, a time-dependent perturbation, to the G band.

3.2.1 Time-independent perturbations: mechanical strain

In this section we are going to study the response of graphene's G band mode under mechanical strain, in particular to hydrostatic strain caused by a hydrostatic compression. We are going to develop the theory behind this phenomena and through some assumptions, obtain a numerical expression for the frequency-pressure rate $\partial\omega_G/\partial P$.

The Grüneisen parameter

The Grüneisen parameter λ_ι for a quasi-harmonic mode ι of frequency ω_ι is defined as [39]

$$\lambda_\iota = -\frac{\partial \ln \omega_\iota}{\partial \ln V} = \frac{1}{\beta}\frac{\partial \ln \omega_\iota}{\partial P} \text{with} \qquad \beta = \frac{1}{V}\left(\frac{\partial V}{\partial P}\right), \tag{3.1}$$

where β is the isothermal volume compressibility, and the derivatives are evaluated around $P = 0$. Essentially, λ is a measure of how the frequency ω scales with the volume. If λ is independent of the volume, from Eq. 3.1, we obtain

$$\frac{\omega(P)}{\omega(P_0)} = \left(\frac{V(P)}{V(P_0)}\right)^{-\lambda_v}, \tag{3.2}$$

where P_0 is the initial pressure. In the graphene case, its thickness can be neglected (since it is a one atom thick material) and the volume V can be replaced by the area A. Moreover, since we are only concerned about the ratio of areas, Eq. 3.2 can be rewritten as

$$\frac{\omega(P)}{\omega(P_0)} = \left(\frac{a^2(P)}{a^2(P_0)}\right)^{-\lambda_G} = \left(\frac{a(P)}{a(P_0)}\right)^{-2\lambda_G}, \tag{3.3}$$

where a is the lattice parameter of graphene [15]. It should be emphasized that Eq. 3.3 only holds for hydrostatic compression because, by representing the ratio of the areas as $a^2(P)/a^2(P_0)$, we are assuming that the strain is isotropic.

G band frequency under strain

Since the G band is a long wavelength ($\vec{k} \sim \vec{0}$) phonon mode, a phenomenological model can be used to analyze the effect of strain on it [38, 40]. We start by writing the equation of motion that describes the $C - C$ bond stretching mode, which gives rise to both, the optical in-plane transverse optic (iTO), and the longitudinal optical (LO) phonon modes.

$$m_i \ddot{\vec{u}}_i = \mathbb{K}^{(AB)}\left(\vec{u}_j - \vec{u}_i\right), \qquad (i, j = A, B) \tag{3.4}$$

where A and B are the two atoms in the unit cell, and $\mathbb{K}^{(AB)}$ is the force constant tensor that represents the interaction between them. We can reduce the degrees of freedom of this two body problem from 4 [the displacements are only in the $(x - y)$ plane] to 2 by introducing the relative displacement coordinate $\vec{u} = \vec{u}_i - \vec{u}_j$. With this substitution, Eq. 3.4 becomes [41]

$$m\ddot{\vec{u}} = -\mathbb{K}\vec{u}, \tag{3.5}$$

or, in terms of the x, y components

$$m\ddot{u}_\alpha = -\sum_\beta K_{\alpha\beta}u_\beta, \qquad (\alpha, \beta \epsilon x, y) \tag{3.6}$$

where m is the reduced mass of the two carbon atoms in the unit cell,(which happens to be equal to the mass of a single carbon atom), and $\mathbb{K}$ is the force constant tensor in the relative displacement coordinates. In the presence of strain, the components of the $\mathbb{K}$ tensor can be expanded in powers of the strain components , $\varepsilon_{\kappa\nu}$, as [38]

$$\begin{aligned} K_{\alpha\beta} &= K^0_{\alpha,\beta}\delta_{\alpha\beta} + \sum_{\kappa\nu}\frac{\partial K_{\alpha\beta}}{\partial \varepsilon_{\kappa\nu}}\varepsilon_{\kappa\nu} \qquad \text{or} \\ K_{\alpha\beta} &= K^0_{\alpha,\beta}\delta_{\alpha\beta} + \sum_{\kappa\nu} K_{\alpha\beta\kappa\nu}\varepsilon_{\kappa\nu}, \end{aligned} \tag{3.7}$$

where $\delta_{\alpha\beta}$ is the Kronecker delta, $K_{\alpha\beta\kappa\nu}$ is the fourth rank tensor that gives the change in the elastic constant $K_{\alpha\beta}$ due to the strain component $\varepsilon_{\kappa\nu}$. As studied in Sec. 1.3.1, the travelling wave $\exp(-i[\vec{k}\cdot\vec{R} - \omega t])\vec{u}_{\vec{k}}$ (with $\vec{R} = \vec{R}_i - \vec{R}_j$ and $\vec{k} = 0$ for this mode), is a solution to Eq. 3.5 leading $\ddot{\vec{u}} = -\omega^2\vec{u}$. By taking this result into account, and inserting (3.7) into (3.6), we have

$$m\omega^2 u_\alpha = m\omega_0^2 u_\alpha + \sum_{\beta,\kappa,\nu} K_{\alpha\beta\kappa\nu}\varepsilon_{\kappa\nu}u_\beta, \qquad (\alpha, \beta, \kappa, \nu \epsilon x, y) \tag{3.8}$$

where we have defined $K^0_{\alpha\alpha} = m\omega_0^2$, with ω_0 being the frequency of unstrained graphene. We can obtain the strain tensor $\varepsilon_{\kappa\nu}$ in an arbitrary coordinate system (x, y) by rotating the diagonal strain tensor in the (l, t) coordinates, where l stands for the phonon propagation direction (longitudinal) and t its perpendicular direction (transversal).

This operation is evaluated as

$$\begin{pmatrix} \cos\theta & \sin\theta \\ -\sin\theta & \cos\theta \end{pmatrix}\begin{pmatrix} \varepsilon_{tt} & 0 \\ 0 & \varepsilon_{ll} \end{pmatrix}\begin{pmatrix} \cos\theta & -\sin\theta \\ \sin\theta & \cos\theta \end{pmatrix} \tag{3.9}$$

where the angle θ is the angle between u_x and the iTO phonon and u_y and LO phonon [28]. Thus the strain tensor in the (x, y) basis can be written in terms of ε_{ll} and ε_{tt} as

$$\begin{pmatrix} \varepsilon_{xx} & \varepsilon_{xy} \\ \varepsilon_{yx} & \varepsilon_{yy} \end{pmatrix} = \begin{pmatrix} \varepsilon_{tt}\cos^2\theta + \varepsilon_{ll}\sin^2\theta & \sin\theta\cos\theta\,(\varepsilon_{ll} - \varepsilon_{tt}) \\ \sin\theta\cos\theta\,(\varepsilon_{ll} - \varepsilon_{tt}) & \varepsilon_{tt}\sin^2\theta + \varepsilon_{ll}\cos^2\theta \end{pmatrix}. \tag{3.10}$$

For $\alpha = x$, Eq. 3.8 becomes

$$\begin{aligned} m\omega^2 u_x = m\omega_0^2 u_x + \left(K_{xxxx}\varepsilon_{xx} + K_{xxxy}\varepsilon_{xy} + K_{xxyx}\varepsilon_{yx} + K_{xxyy}\varepsilon_{yy}\right) u_x \\ + \left(K_{xyxx}\varepsilon_{xx} + K_{xyxy}\varepsilon_{xy} + K_{xyyx}\varepsilon_{yx} + K_{xyyy}\varepsilon_{yy}\right) u_y. \end{aligned} \tag{3.11}$$

Next, can reduce the number of terms in (3.11) by symmetry considerations. Since both $K_{\alpha\beta}$ and $\varepsilon_{\kappa\nu}$ are components of second-rank symmetric tensors, they satisfy $K_{\alpha\beta} = K_{\beta\alpha}$ and $\varepsilon_{\kappa\nu} = \varepsilon_{\nu\kappa}$. It follows that:

$$K_{\alpha\beta\kappa\nu} = K_{\alpha\beta\nu\kappa} = K_{\beta\alpha\nu\kappa} = K_{\beta\alpha\kappa\nu}, \quad \text{and} \quad K_{\alpha\beta\kappa\nu} = K_{\kappa\nu\alpha\beta}, \tag{3.12}$$

where the latst condition comes from the fact that this fourth-rank tensor is symmetric for the interchange between the two pair of indices $(\alpha\beta)$ and $(\kappa\nu)$. We can also explore the hexagonal symmetry of graphene to restrict the number of independent components of $K_{\alpha\beta\kappa\nu}$ to a few, namely K_{xxxx} and K_{xxyy} in the two-dimensional motion and there are three different nonzero values that can be expressed in terms of these two components, namely $K_{xxxx} = K_{yyyy}$, K_{xxyy} and $K_{xyxy} = (K_{xxxx} - K_{xxyy})/2$ in this case [28, 42]. The oder $K_{\alpha\beta\kappa\nu}$ components vanish is because the $K_{\alpha\beta\kappa\nu}$ tensor is invariant under a $2\pi/3$ rotation [28]. Taking into account all these symmetry considerations, the $K_{\alpha\beta\kappa\nu}$ tensor can be expressed in the matrix form as

$$\begin{pmatrix} K_{xxxx} & K_{xxxy} & K_{xxyx} & K_{xxyy} \\ K_{xyxx} & K_{xyxy} & K_{xyyx} & K_{xyyy} \\ K_{yxxx} & K_{yxxy} & K_{yxyx} & K_{yxyy} \\ K_{yyxx} & K_{yyxy} & K_{yyyx} & K_{yyyy} \end{pmatrix} = \begin{pmatrix} K_{xxxx} & 0 & 0 & K_{xxyy} \\ 0 & (K_{xxxx} - K_{xxyy})/2 & (K_{xxxx} - K_{xxyy})/2 & 0 \\ 0 & (K_{xxxx} - K_{xxyy})/2 & (K_{xxxx} - K_{xxyy})/2 & 0 \\ K_{xxyy} & 0 & 0 & K_{xxxx} \end{pmatrix}. \tag{3.13}$$

Thus Eq. 3.11 becomes

$$
\begin{aligned}
&m\left(\omega^2-\omega_0^2\right)u_x+\left(K_{xxxx}\varepsilon_{xx}+K_{xxyy}\varepsilon_{yy}\right)u_x\\
&-\left[\left(K_{xxxx}-K_{xxyy}\right)\varepsilon_{xy}\right]u_y=0.
\end{aligned}
\tag{3.14}
$$

From now on we are going to use the short notation $xx = 1$, $yy = 2$, $zz = 3$, $yz = zy = 4$, $xz = zx = 5$ and $xy = yx = 6$, whenever we are dealing with four rank tensors. With this notation, K_{xxxx} and K_{xxyy} become K_{11} and K_{12}, respectively. Besides that , in order to get rid of the mass m in Eq. 3.14 we define the parameter $\bar{K}$, as $\bar{K}_{11} = K_{11}/m$. With these modifications we get

$$
\left[\Lambda-\left(\bar{K}_{11}\varepsilon_{xx}+\bar{K}_{12}\varepsilon_{yy}\right)\right]u_x-\left[\left(\bar{K}_{11}-\bar{K}_{12}\right)\varepsilon_{xy}\right]u_y=0,
\tag{3.15}
$$

with $\Lambda = (\omega^2-\omega_0^2)$. If we repeat the process to $\alpha = y$ in Eq. 3.8, we obtain the following system of equations

$$
\begin{pmatrix}
\Lambda-\left(\bar{K}_{11}\varepsilon_{xx}+\bar{K}_{12}\varepsilon_{yy}\right) & -\left(\bar{K}_{11}-\bar{K}_{12}\right)\varepsilon_{xy}\\
-\left(\bar{K}_{11}-\bar{K}_{12}\right)\varepsilon_{xy} & \Lambda-\left(\bar{K}_{11}\varepsilon_{xx}+\bar{K}_{12}\varepsilon_{yy}\right)
\end{pmatrix}
\begin{pmatrix}u_x\\u_y\end{pmatrix}=\begin{pmatrix}0\\0\end{pmatrix}
\tag{3.16}
$$

In order to get the nontrivial solution $(u_x, u_y)^t \neq (0,0)^t$, the determinant of the matrix of Eq. 3.16 should be zero. To achieve this condition,we must solve the secular equation

$$
\begin{vmatrix}
\Lambda-\left(\bar{K}_{11}\varepsilon_{xx}+\bar{K}_{12}\varepsilon_{yy}\right) & -\left(\bar{K}_{11}-\bar{K}_{12}\right)\varepsilon_{xy}\\
-\left(\bar{K}_{11}-\bar{K}_{12}\right)\varepsilon_{xy} & \Lambda-\left(\bar{K}_{11}\varepsilon_{xx}+\bar{K}_{12}\varepsilon_{yy}\right)
\end{vmatrix}=0,
\tag{3.17}
$$

with the $\varepsilon_{\kappa\nu}$ given by Eq. 3.10. After a long evaluation , the following condition is extracted from (3.17)

$$
\Lambda=\left(\omega^2-\omega_0^2\right)=\frac{(\bar{K}_{11}+\bar{K}_{12})(e_{ll}+e_{tt})\pm(\bar{K}_{11}-\bar{K}_{12})(e_{ll}-e_{tt})}{2}.
\tag{3.18}
$$

Notice that all $\sin\theta$ and $\cos\theta$ terms disappeared during the calculation, a direct consequence of the in-plane isotropy of the force constants in the graphene lattice [28].

If we consider that the strained and unstrained frequencies are similar (small frequency deviation limit), we can use the approximation $(\omega^2-\omega_0^2) = (\omega+\omega_0)(\omega-\omega_0) \sim 2\omega_0\Delta\omega$, with

$\Delta\omega \equiv (\omega - \omega_0)$. Within this approximation, Eq. (3.18) can be expressed in terms of the frequency change as

$$\frac{\Delta\omega}{\omega_0} = \frac{\bar{K}_{11} + \bar{K}_{12}}{4\omega_0^2}(e_{ll} + e_{tt}) \pm \frac{\bar{K}_{11} - \bar{K}_{12}}{4\omega_0^2}(e_{ll} - e_{tt}). \tag{3.19}$$

Next, the hydrostatic and shear components of the strain are defined as

$$\varepsilon_h = \frac{e_{ll} + e_{tt}}{2} \tag{3.20}$$

and

$$\varepsilon_s = \frac{e_{ll} - e_{tt}}{2}, \tag{3.21}$$

respectively. The Grüneisen parameter defined in Sec. 3.2.1 can now be expressed in terms of the hydrostatic strain (Eq. 3.20) as [43]

$$\lambda = -\frac{1}{2\omega_0}\frac{\partial\omega}{\partial\varepsilon_h}. \tag{3.22}$$

By taking the result of the partial derivative of ω as a function of ε_h in Eq. 3.19, (3.22) becomes

$$\lambda = -\frac{\bar{K}_{11} + \bar{K}_{12}}{4\omega_0^2}. \tag{3.23}$$

In a similar way, we can also introduce the β parameter as

$$\lambda = -\frac{1}{\omega_0}\frac{\partial\omega}{\partial\varepsilon_s}. \tag{3.24}$$

With these definitions, Eq. 3.19 can be expressed in a more useful form as

$$\omega = \omega_0 - 2\lambda\omega_0 e_h \pm \beta e_s. \tag{3.25}$$

For a hydrostatic compression ($e_{ll} = e_{tt} = e_h$ and $e_s = 0$) we can express the frequency ω in terms of the hydrostatic strain as

$$\omega = \omega_0 - 2\lambda\omega_0 e_h. \tag{3.26}$$

As a final step, in order to obtain the frequency as function of the pressure [$\omega(P)$] we must express e_h in terms of the stress on the graphene's lattice which, in turn, can be obtained from the strain. The connection between strain and stress is made via elastic constants as shown in next section.

A Numerical Value for the Frequency Slope of G Band Frequency with Pressure

From the elasticity theory, the components of the strain tensor e_{kv} can be obtained by

$$e_{ij} = \sum_{k,l} \gamma_{ijkl}\sigma_{kl}, \tag{3.27}$$

where γ_{ijkl} is a component of the elastic compliance tensor (or just the elastic tensor) and σ_{kl} is a component of the stress tensor. Equation 3.27 is a generalization of Hook's law applied to all materials within the elastic regime (harmonic approximation). It says that each displacement (strain) component is linearly related to each force (stress) component.

For hydrostatic compression in which the material is subjected to a pressure P, the hydrostatic stress follows the condition

$$\sigma_{ij} = -P\delta_{ij}, \tag{3.28}$$

with δ_{ij} being a Kronecker delta. This is the key relation that associates the hydrostatic strain with P. Since graphene is isotropic, we are going to express the hydrostatic strain (3.20) as $e_h = (e_{xx} + e_{yy})/2$. Using Eq. 3.27, we can express e_{xx} in terms of the stress σ_{ij}, as:

$$e_{xx} = \gamma_{xxxx}\sigma_{xx} + \gamma_{xxxy}\sigma_{xy} + \gamma_{xxxz}\sigma_{xz} + ... + \gamma_{xxzz}\sigma_{zz}. \tag{3.29}$$

If the medium is hydrostatic, only the diagonal components of the stress tensor are non null, that is, the σ_{ii} components with $i \in x, y, z$. Therefore, for a hydrostatic case, substituting Eq. 3.28 into Eq. 3.29 yields

$$\begin{aligned} e_{xx} &= -\left(\gamma_{xxxx} + \gamma_{xxyy} + \gamma_{xxzz}\right) P \\ &= -\left(\gamma_{11} + \gamma_{12} + \gamma_{13}\right) P, \end{aligned} \tag{3.30}$$

where in the last line we have recalled the condensed notation for fourth rank tensors. We can proceed in the same way to obtain e_{yy} on the form

$$e_{yy} = -\left(\gamma_{21} + \gamma_{22} + \gamma_{23}\right) P. \tag{3.31}$$

By taking into account symmetry considerations, $\gamma_{12} = \gamma_{21}$ [γ_{ijkl} is symmetric for the interchange of the two sets of two indices (ij) and (kl)], $\gamma_{11} = \gamma_{22}$ and $\gamma_{13} = \gamma_{23}$ (graphene is isotropic) we obtain

$$e_h = \frac{e_{xx} + e_{yy}}{2} = -(\gamma_{11} + \gamma_{12} + \gamma_{13})\, P. \tag{3.32}$$

Substitution of Eq. 3.32 in (3.26) gives the frequency ω as a function of P on the form

$$\omega(P) = \omega_0 + 2\lambda\omega_0 (\gamma_{11} + \gamma_{12} + \gamma_{13})\, P, \tag{3.33}$$

if we consider the effect of compression along the z axis on the in-plane displacements given by γ_{13}, or

$$\omega(P) = \omega_0 + 2\lambda\omega_0 (\gamma_{11} + \gamma_{12})\, P, \tag{3.34}$$

if we neglect this contribution. The latter is going to be assumed as a good approximation for the graphene case.

We are interested on the G band analysis, which is related to the zone-center bond-stretching mode with E_2g symmetry. Therefore, to obtain a numerical expression for the expected G Band's frequency shift rate with pressure ($\partial\omega_G/\partial P$) we need the values of the Grüneisen parameter λ for the G mode and also the elastic constants γ_{11}, γ_{12}. Several works have determined these parameters either experimentally or theoretically for graphene and graphite [43, 42, 44, 38, 45, 46]. For the G mode, the values of λ range from 1.8 to 2.4 [43]. The value chosen is 1.8 and it was determined experimentaly from a biaxially strained graphene bubble [43]. This value was chosen for two reasons: (i) in this experiment, graphene was subjected to a biaxial strain, which is closer to the situation of hydrostatic strain when compared to uniaxial strain, (ii) there was no graphene-substrate over the bubble. The values for γ_{11} γ_{12} were taken from Reference [46] as 10^{-3} GPa^{-1} and $-0.12x10^{-3}$ GPa^{-1}, respectively.

Inserting the aforementioned values in Eq. 3.34, and adopting the G band frequency of unstrained graphene as 1582cm^{-1}, we get $\partial\omega_G/\partial P = 5$cm^{-1}GPa^{-1}, which is in close agreement to the pressure slope of ~ 5cm^{-1}GPa^{-1} and $(5.6 - 5.9)$ cm^{-1}GPa^{-1} obtained experimentally for an unsupported mixture of graphene flakes of different thicknesses and for single layer graphene, respectively [14].

3.2.2 Time-Dependent Perturbations: Charge Doping

In this section we are going to study the effect of charge doping on the G band frequency. The subject will be addressed through different approaches: (i) a more qualitative one via Khon anomaly and, (ii) a more quantitative one through the results of time-dependent perturbation theory. The latter approach shows that the standard approximation to treat interactions between electrons and phonons, the so called adiabatic Born-Oppenheimer approximation (ABO), fails when applied to doped graphene. The outcome of both approaches is a blueshift in ω_G with increasing doping, which is confirmed by experimental results [47, 48].

Kohn anomaly in doped graphene

The effect of charge doping on graphene can be probed experimentally through the fabrication of field-effect transistors (FET) based on mono- or few-layer graphene [49, 50, 51, 48]. By tuning the FET gate voltage (V_g) it is possible to dope graphene by adding an extra surface electron or hole charge. In a FET-based experiment, graphene can be doped up to a charge concentration of $3 \times 10^{13}\text{cm}^{-2}$ [49, 50, 51], which corresponds , in the monolayer case, to a 0.2% valence charge variation. The resulting chemical-bond modification could induce a variation of bond-lengths and phonon-frequencies of the same order, which can be probed experimentally.

As studied in Sec. 1.4.3, the Kohn anomaly is the frequency softening of a phonon mode of wave vector $\vec{q}$ that is able to connect two states $\vec{k}_1$ and $\vec{k}_2$, both at the Fermi surface, such that $\vec{q} = \vec{k}_2 - \vec{k}_1 + \vec{K}_L$, where $\vec{K}_L$ is a reciprocal lattice vector. In graphene, Khon anomalies can occur for phonon modes at the Gamma point ($\vec{q} = 0$), which includes the E_{2g} mode giving rise to the G band. The presence of Kohn anomalies in graphene is considerably enhanced, leading to a variation on the optical phonon-frequencies which is much larger than the 0.2% expected in conventional systems [52]. By doping graphene, the change in the Fermi surface moves the Khon anomaly away from $\vec{q} = \Gamma$. As a consequence, we can expect a stiffening of the G mode with doping [47]. This is indeed observed experimentally [47, 48] and the calculation for the variations on ω_G in doped graphene is carried out in the next Section.

Breakdown of the adiabatic Born-Oppenheimer (ABO) approximation in graphene

The adiabatic Born-Oppenheimer approximation (ABO) has been the standard ansatz to describe the interaction between electrons and nuclei or lattice vibrations since the early days of quantum mechanics [53, 54]. This approximation assumes that the lighter electrons adjust adiabatically to the motion of heavier nuclei, or heavier ions in case of lattice vibrations, remaining, at any time, in their instantaneous ground state. ABO is well justified when the energy gap between ground and excited electronic states is larger then the energy scale of the ion motion. The E_{2g} phonon is a dynamical perturbation described by a time-dependent lattice displacement $\vec{u} = \vec{u}_0 \cos(\omega_G t)$ oscillating at the G Band frequency. Within ABO, it is assumed that at any given moment t, the electrons are in the adiabatic ground state of the instantaneous band structure. However, the period of the G Band oscillation is $\sim$ 3 fs, which is much smaller than typical electron-momentum relaxation times τ_m (owing to impurity, electron-electron, and electron-phonon scattering with non-zero momentum phonons). In fact, τ_m of a few hundred femtoseconds is deduced from the electron mobility in graphene, and similar values have been experimentally extracted from ultrafast spectroscopy in graphite [47]. As a consequence, the excited electrons do not have enough time to relax their momenta and reach the instantaneous adiabatic ground state, as assumed in ABO. Therefore doped graphene is a rare example where this approximation fails [52].

To associate the changes in the G mode frequency with doping, we first need to know graphene's electronic structure in the presence of the E_{2g} phonon mode. In graphene, the electronic bands near the high-symmetry $K(K')$ points are well described by a Dirac-like dispersion $E(\vec{k}, \pi^*) = \hbar v_F |\vec{k}|$ for the π^* anti-bonding energy band, and $E(\vec{k}, \pi) = -\hbar v_F |\vec{k}|$ the π bonding energy band. Here, $\vec{k}$ is the electron momentum measured from the K point, and v_F is the Fermi velocity ($\hbar v_F = 5.52$eVÅ, as obtained from density functional theory DFT [31]). The Dirac point is defined by the crossing of these conic bands and coincides with K, as in Fig. 3.4 (a). The E_{2g} phonon in graphene consists of an in-plane displacement of the carbon atoms in the unit cell by a vector $\pm\vec{u}/\sqrt{2}$, as in Fig. 3.4 (d). The periodic motion of the atoms in real-space is mirrored into an identical motion of the Dirac-points in reciprocal space. The bands are still described by a cone, with the Dirac points shifted from K by a vector $\vec{s}$, as illustarted in Figs. 3.4 (b,c). By considering the effects of electron-phonon interactions, DFT calculations predict that the dependence of the electronic bands on $\vec{u}$ can be described as:

$$E(\vec{k}, \pi^*, \vec{u}) = \pm\hbar v_F |\vec{k} - \vec{s}(\vec{u})| \tag{3.35}$$

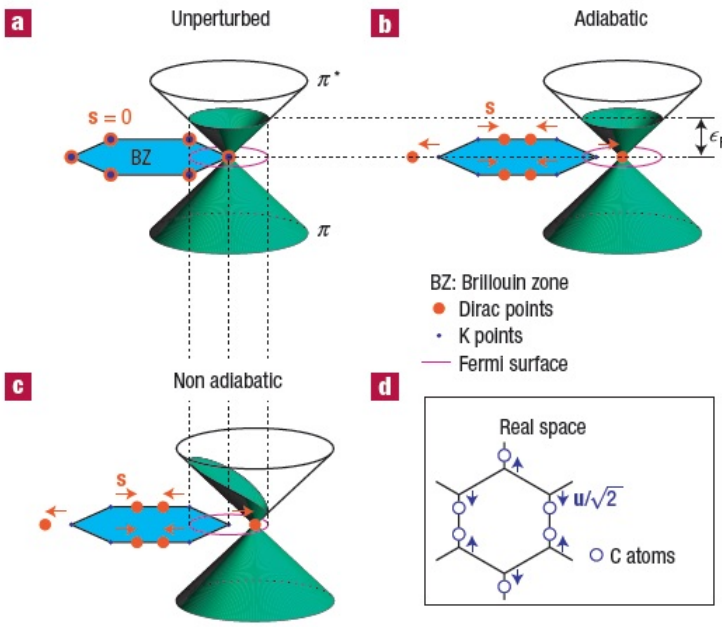

Figure 3.4: Schematic electronic dispersion (π and π^*) near the K point in first Brilloun Zone of graphene. The occupied electronic states are shown in green. (a) Electronic bands of the static crystal lattice, not considering lattice vibrations. The Dirac point is at K, the electronic states are filled up to the Fermi energy ε_F, and the Fermi surface is a circle centered at K.(b) Bands in the presence of an E_{2g} mode within ABO. The Dirac points are displaced from K by $\pm\vec{s}$. The electrons remain in the instantaneous ground state: the bands are filled up to ε_F, and the Fermi surface follows the Dirac-point displacement. The total energy does not depend on $\vec{s}$. (c) Bands in the presence of an E_{2g} mode in the non-adiabatic case. The electrons do not have time to relax their momenta to reach the instantaneous adiabatic ground sate. In the absence of scattering, the electron momentum is conserved and a state with momentum $\vec{k}$ is occupied if the same $\vec{k}$ is occupied in the unperturbed case. Therefore the Fermi surface does not follow the Dirac-cone displacement. The total energy increases with s^2, resulting in the E_{2g} phonon stiffening.(d) Atomic displacement of carbon atoms in real space for the E_{2g} mode. The atoms are displaced from their equilibrium positions by $\pm\vec{u}/2$. Figure taken from [47].

with $\vec{s}\cdot\vec{u} = 0$. Equation 3.35 well reproduces the modification on the electronic band structure of graphene owing to a static displacement of the atoms according to the G phonon pattern.

Next, with the knowledge of the electronic bands we can determinate the G phonon frequency as a function of the Fermi energy, ϵ_F. In particular,

$$\hbar\Delta\omega = \hbar\omega - \hbar\omega_0 = \frac{\hbar}{2M\omega_0}\frac{d^2\Delta E}{(du)^2} \tag{3.36}$$

where M is the carbon atom mass, ω_0 is the G phonon frequency of undoped graphene ($\Delta\omega \ll \omega_0$) and ΔE is the variation of the electronic energy with ϵ_F. Within ABO, $\Delta E(\vec{u})$ is computed assuming that the electrons are supposed to be in the ground state at any time, which means that the bands are filled up to ϵ_F as in Fig. 3.4 (b). Therefore the adiabatic ΔE is

$$\Delta E(u) = \frac{4A}{(2\pi^2)} \int_{E(\vec{k},\pi^*,\vec{u})<\epsilon_F} E(\vec{k},\pi^*,\vec{u}) d^2k, \tag{3.37}$$

considering $\epsilon_F > 0$ (n doping). The factor $A/(2\pi^2)$ accounts for the transformation of the summand into an integral in reciprocal space, A being the unit cell area, with the fact 4 accounting for spin and K point degeneracy. Combining Eqs. 3.35 and 3.37 we find that ΔE does not depend on $\vec{u}$ and $\hbar\Delta\omega = 0$. Therefore, as expected, within ABO the G band frequency is independent of the Fermi energy, which is in contrast with experiments. The departure from the adiabatic ground state can be accounted in the calculation of ΔE by filling the perturbed bands $E(\vec{k},\pi^*,\vec{u})$ with the occupations of the unperturbed bands $E(\vec{k},\pi^*,\vec{u}=\vec{0})$ as in Fig. 3.4 (c):

$$\Delta E(u) = \frac{4A}{(2\pi^2)} \int_{E(\vec{k},\pi^*,\vec{u}=\vec{0})<\epsilon_F} E(\vec{k},\pi^*,\vec{u}) d^2k + O(u^3). \tag{3.38}$$

Equation 3.38 is valid in the limit $\epsilon_F \gg \hbar\omega_0/2$, and can be rigorously derived using time-dependent perturbation theory. Now the adiabatic energy ΔE depends on $\vec{u}$. By combining Eqs. 3.35 and 3.38, and performing the integral, we get

$$\hbar\Delta\omega = \alpha|\epsilon_F|, \tag{3.39}$$

with $\alpha = 4.39 \times 10^{-3}$. The result of Eq. 3.39 can be extended to any temperature and this is performed in Reference [47]. By comparing the adiabatic and non-adiabatic calculations, we conclude that the stiffening of the E_{2g} mode with $|\epsilon_F|$ is due to the departure of the electron population from the adiabatic ground state.

A powerful analogy can be obtained by considering what happens to a filled glass when shaken horizontally [47]. The liquid gravitational energy and its level mimic the electronic energy ΔE and ε_F, respectively. The shaking frequency mimics the phonon frequency, and the relaxation time of the liquid surface mimics the electron relaxation time. If the motion of the glass is slow, the liquid surface remains flat and its gravitation energy is independent of the glass horizontal position. If the motion of the glass is rapid, the liquid surface is not flat anymore and its gravitational energy increases with the displacement of the glass. To extend the analogy, a conical glass (such as a Martini glass) should be used. In this case, the liquid surface increases with the liquid level and, the higher the liquid level, the larger the difference between the gravitational energies in the fast- and slow-shaken glasses. Furthermore, the lower the liquid level, the closest the liquid surface will be from a flat profile, regardless of the shaking frequency. Indeed, in graphene, the higher the Fermi level, the larger the difference between the non-adiabatic and the adiabatic values of ΔE. This causes the stiffening of the phonon frequency with ε_F [47].

It is also possible to establish a qualitative analysis regarding the G band's full width at half-maximum, Γ_G. Since the Raman process of G Band probes $\vec{q} = 0$ phonons, the broadening in energy of this band indicates a decrease in the lifetime of the phonon according to the uncertainty principle ($\Delta E \Delta t \sim \hbar$). As seen in Sec. (1.4.3), the phonon decay processes is mediated by the creation of an electron-hole pair. Therefore, if ε_F is increased by an amount larger than half of the phonon energy, the creation of the electron-hole pair will be forbidden by the Pauli exclusion principle. Consequently, the lifetime of the phonon is increased resulting in a decrease of Γ_G.

Chapter 4

Sample fabrication: CVD growth and transfer

The samples used in the high-pressure Raman experiment consist of graphene on a polytetrafluoroethylene (PTFE, commonly referred as Teflon) filter membrane substrate. The graphene samples were grown on copper by the Chemical Vapor Deposition (CVD) technique and then transferred onto the PTFE membranes through a lamination technique. The synthesis and transfer work were performed under supervision of professor Jing Kong, at the Nanomaterials and Electronics Group in the Electrical Engineering and Computer Science (EECS) Department, Massachusetts Institute of Technology (MIT), during a six month exchange program from September 2011 to Feburary 2012.

4.0.3 CVD growth

The chemical vapor deposition technique consists in a chemical reaction catalyzed by surface in which the reactant adsorbs on the catalyst surface, reacting on it and producing a new surface [55]. The catalysts utilized to synthesize graphene are usually transition metals, including nickle, copper and ruthenium [56, 57, 58]. In this work, copper was utilized. In all these works, carbon species such as methane or ethylene react under high temperatures $(900 - 1100)^{\circ}C$ on thin foils/films. The growth mechanism of graphene on a catalyst is possibly influenced by many factors such as the limit of solubility of carbon on the metal, the metal's crystalline struc-

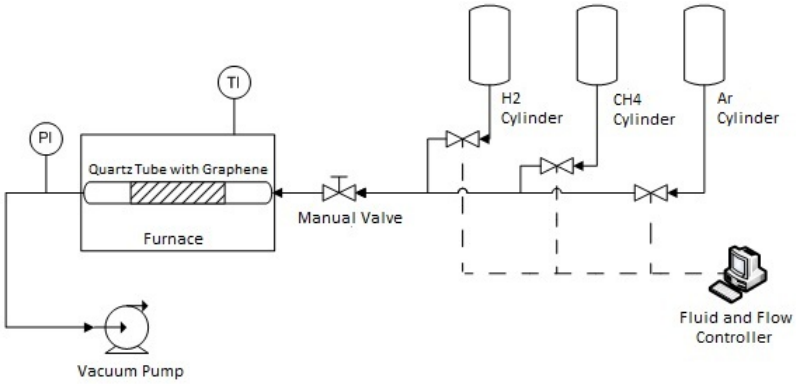

Figure 4.1: Fluxogram of LPCVD graphene synthesis.

ture, lattice parameters, and thermodynamic parameters such as the temperature and pressure of the system. When it comes to synthesize large area graphene, low pressure CVD (LPCVD) have been broadly utilized since it was first reported in 2009 [56], and it was adopted in this work as well.

The synthesis process works as follows. Initially a thin high-purity copper foil is carefully cut to be used as the growth substrate. The foil was carefully introduced inside the central region of a quartz tube, and great care was taken in to avoid the copper foil to be bent or stressed, keeping it flat. Such care was necessary to avoid gradients on the copper foil that could affect the kinetics of the surface reaction, which would certainly reflect on the final quality of the sample. The tube was inserted in a tub furnace and the input and output connections to the gas lines were plugged as illustrated in Fig. 4.1. The gas output line was directly connected to a vacuum pump. The valve between the gas output line and the vacuum pump was opened until the pressure (measured with the aid of a pressure transducer located at the output of the tube) reached 50 mTorr. The furnace allowed for programming the temperature as a function of time. The furnace was then closed and the synthesis process was able to start.

The graphene synthesis could be divided into four stages. In the first stage the substrate was subject to a 20 minutes temperature ramp from room temperature to 1000°C under a constant flow of 10 sccm (standard cubic centimeter per minute) of hydrogen. In the second stage, the temperature was kept at 1000°C and the flow of hydrogen was kept constant at the same rate of 10 sccm for 30 minutes. Stage 3 corresponds to the chemical synthesis. With the temperature and hydrogen flow kept constant at 1000°C and 10 sccm, respectively, a methane flow of 20 sccm was introduced to the gas flux, and the reaction took place on the copper surface for 30 minutes. In the fourth and final stage, the furnace was coled from 1000°C to room temperature at

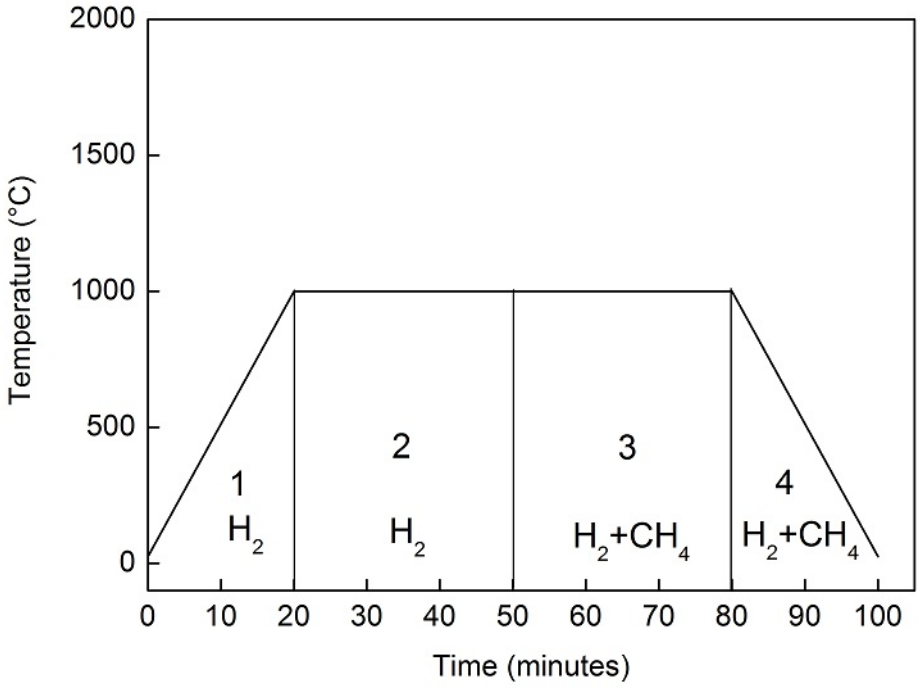

Figure 4.2: Stages of the process of LPCVD Graphene Synthesis.

a constant flow of hydrogen and methane at 10 sccm and 20 sccm, respectively, for 20 minutes. The four stages are represented in Fig. 4.2. The cooling was performed in two steps: first, the furnace was partially opened (turning it off automatically) and the system was cooled to 760°C; below this temperature, the furnace was completely opened and the system was cooled with the aid of a vent placed directly in front of the opened furnace. At the end of the process, the valve between the output gas line and the vacuum pump was closed and the connection to the output gas was loosen so that the pressure was relieved inside the tube. The methane flow was drop to zero, and an argon flow of 900 sccm was introduced to the system. After 30 s the tube was removed from the furnace, the connections to the gas lines were released, and the argon and hydrogen flow were drop to zero.

The final result, after removing the copper foil carefully from the quartz tube, was graphene grown on both sides of the copper surface. A first evidence for the presence of graphene was that the copper foil became more opaque. The samples were then stored in a vacuum environment.

4.0.4 Direct transfer of graphene onto PTFE

Once the sample was grown on copper, the next step would be to transfer the graphene layers to the Teflon substrate. The technique to perform that specific transfer, as well as to other flexible

substrates, was developed by the author and collaborators and it is published in Ref. [59]. The target substrate was a polytetrafluoroethylene (PTFE, commonly referred to as Teflon) filter membrane with a $0.2\mu m$ pore size.

The process started by cleaning the substrate with isopropanol and blow-drying it with a nitrogen gun. The graphene/copper/graphene (G/Cu/G) stack (recall that graphene grows on both sides of the copper foil) was cut to the desired graphene size and pressed against the target substrate, the Teflon membrane, to provide initial graphene-substrate contact. A protective sheet of weighing paper was put on top of the Teflon/G/Cu/G and this stack was sandwiched between two PET films, as shown in Fig. 4.3 (a), and put into a 330-SCL hot/cold laminator machine, as shown in Fig. 4.3 (b).

The PET films were used to prevent the copper foil from directly contacting the rollers in the lamination machine and to lend mechanical robustness to the stack. The protective weighing paper was used to prevent the copper foil from adhering to the PET films, which become viscoelastic when the laminator is heated to temperatures above 70°C, PET's glass transition temperature t_g. The temperature was set to be above Teflon's t_g, which is 115°C. The laminator machine provided the pressure necessary to mold the substrate to the morphology of the G/Cu/G. After lamination, proper adhesion was verified by visually checking for gaps between the Teflon membrane and graphene/copper foil. If gaps were found, the lamination procedure was repeated. After lamination, the Teflon/G/Cu/G stack was placed in a copper etchant solution ($FeCl_3$-based) for 30 min, as shown in Fig. 4.3 (c). This solution etched the copper substrate, carrying one of the graphene layers (the one which was not in contact with Teflon) with it. Finally, the samples were rinsed in deionized water and blow-dried with a nitrogen gun. The final result is graphene transfered to Teflon as shown in Fig. 4.3(d). Interestingly, graphene can be easily visualized on this substrate.

In order to produce a second layer atop the first, the whole process was repeated, with the exception that the target substrate was now Grafene/Teflon instead of Teflon. At the end of the process a double transferred graphene on Teflon sample (G/G/Teflon) was obtained with a graphene area of (2×2) cm.

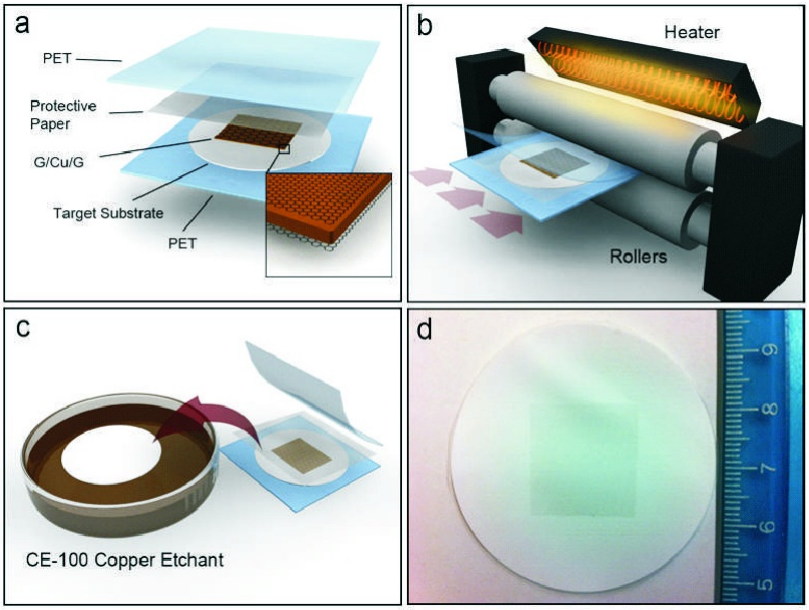

Figure 4.3: Schematic diagram of the direct transfer of graphene to Teflon via lamination. (a) Copper foil with CVD graphene grown on both sides (G/Cu/G) is placed in between the Teflon and the protective paper. This stack is then put between two PET films. (b) The PET/Teflon/(G/Cu/G)/paper/PET sandwich is inserted into the hot/cold lamination machine. (c) The PET films and the protective paper are then removed and the remaining Teflon/ (G/Cu/G) stack is placed on a copper etchant solution for 30 min. (d) The graphene/substrate is rinsed in deionized water and blow-dried with nitrogen. In this picture, the ruler is scaled in centimeters. Figure from [59].

Chapter 5

High Pressure Raman of Graphene

5.1 Experimental details

The high pressure Raman spectroscopy of graphene experiments were performed with a pneumatic pressurized diamond anvil cell (DAC) at the Physics Department of Federal University of Ceará under supervision of Professors Alexandre Paschoal, Paulo de Tarso and Antonio Gomes and Professor Nadia Ferreira from the Federal Institute of Ceará at Tianguá.

5.1.1 The diamond anvil cell (DAC)

Up to three decades ago, the study of materials subjected to high pressure and/or extreme temperature conditions was performed by means of shocking waves experiments. However, this technique is extremely complicated because the materials properties must be measured in a synchronized fashion under a short period of time. The diamond anvil cell (DAC) changed this scenario by making it possible to perform such experiments under static conditions (constant pressure and temperature) with an even higher operating range, thus allowing for the determination of an equation of state for the studied material. With a DAC, it is possible to reach pressures up to $\sim 10^2$ GPa (1GPa = 10^4 atm) and temperatures up to $\sim 10^{3^\circ}$C , which are similar conditions as found in the center of Earth. Another advantage of the usage of DACs is the small

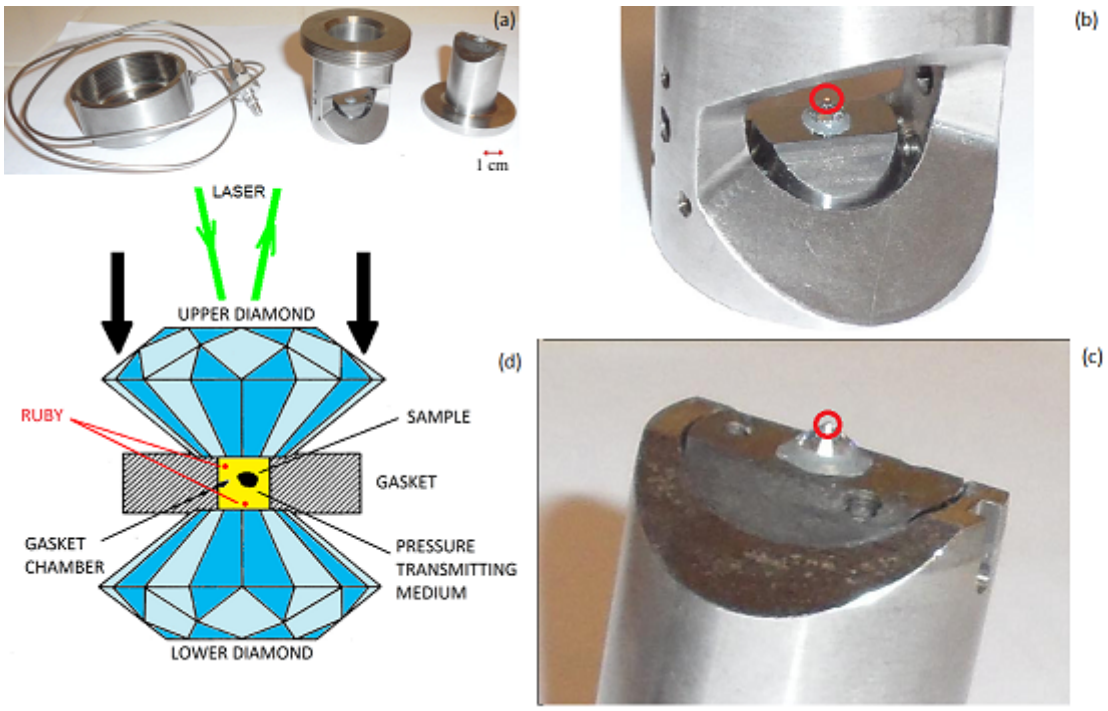

Figure 5.1: The diamond anvill cell (DAC). In (a) a pneumatic pressurized DAC is shown with the diamonds featured in (b) and (c). In (d) the mechanism behind the operation of the DAC is represented.

amount of sample needed for the experiment.

The mechanism behind the operation of the DAC is the approximation of two conical polished diamonds with extremities cut (culet) to form flat planes with diameters around $300-600\,\mu$m as illustrated in Fig. 5.1. Due to the small compression area, extreme pressures can be generated with the application of moderate forces. Diamonds are widely known for their hardness and transparency to visible light (as well as to X-rays) which justifies their use in these experiments. The way the compression is performed depends on the DAC type. In Fig. 5.1 it is shown a pneumatically pressurized DAC whose diamonds are displaced by a piston displaced by a pneumatic membrane inflated by a lateral gas inlet [60].

The cell consists of two parts, each one containing a diamond as shown in Fig. 5.1 (a), (b) and (c). The two parts snap together, and the system is connected by a threaded fitting to the gas inlet/outlet line. Once the diamonds are aligned in parallel, a thin steel plate (gasket) with thickness around $100\,\mu$m is inserted between them. The gasket can be sometimes previously compressed (indented) in order to minimize the plastic deformation during the experiment. After indention, a hole with a diameter around $1/3$ of the diamond culet is drilled in the region of compression. A compression chamber is then created, and the sample, together with the

pressure transmitting media (PTM), can be both inserted as represented in Fig. 5.1.

Together with the diamond culets, the gasket is at the heart of a diamond anvil cell. There is a wide variety of materials for composing the gaskets, and a suitable choice must be made for each specific high-pressure experiment. The way the gasket works has been analyzed theoretically, using a (completely different context) minting coins model [61]. The part of the gasket between the culets undergoes plastic deformation as the diamonds advance, and is extruded. The stress within the metal decreases linearly in the direction of extrusion, and the gradient of stress increases as the gasket becomes thinner. Extrusion may be entirely outwards, or may be inwards so as to collapse the sample hole. In the latter case there is a neutral ring of metal that does not move, separating the outer part (which extrudes outwards) from the inner (which extrudes inwards). If the extrusion is completely performed outwards, the sample hole necessarily enlarges, and pressurization occurs because of a large advance of the diamonds. This happens if the gasket is too thick for the pressure range, being a highly undesirable situation. The sample hole becomes barrel-shaped and any initial asymmetry as a non-central hole or non parallel culets becomes exaggerated. If the gasket is made thinner, the stress rises more quickly from the edge inwards. In this case, it reaches a pressure value at the neutral ring which is greater than the sample pressure, falling inward to the sample hole. Consequently, inwards extrusion takes place, and the hole gets smaller as the pressure is increased. This means that the diamonds do not have to advance so much for pressurization. It also means that the hole is stable, and initial asymmetry is much less dangerous in this case. Therefore, the DAC should be operated in this régime [61].

In order to calibrate the pressure inside the chamber, small pieces of ruby are inserted inside of it. The ruby calibration method (Cr^{3+} doped Al_2O_3) is the widest method used in high pressure studies. The calibration via ruby fluorescence is based on X-ray diffraction analysis of a metal (Cu, Mo, Pd e Ag) with a well established equation of state, so that its molar volume can be accurately determined via comparative X-Ray diffraction measurements [62]. NaCl was also used as a standard sample, due to its well-established equation of state [63, 64]. The advantage of the ruby calibration method is that is can be quickly and easily performed in any laboratory equipped with a monochromatic light source and a spectrometer.

Under visible light excitation, ruby emits fluorescence in the characteristic frequencies R_1 and R_2 as can be observed in Fig. 5.2. The evolution of the R_1 frequency with increasing pressure is well established, and its calibration curve is almost linear in the range $0 - 10$ GPa. There-

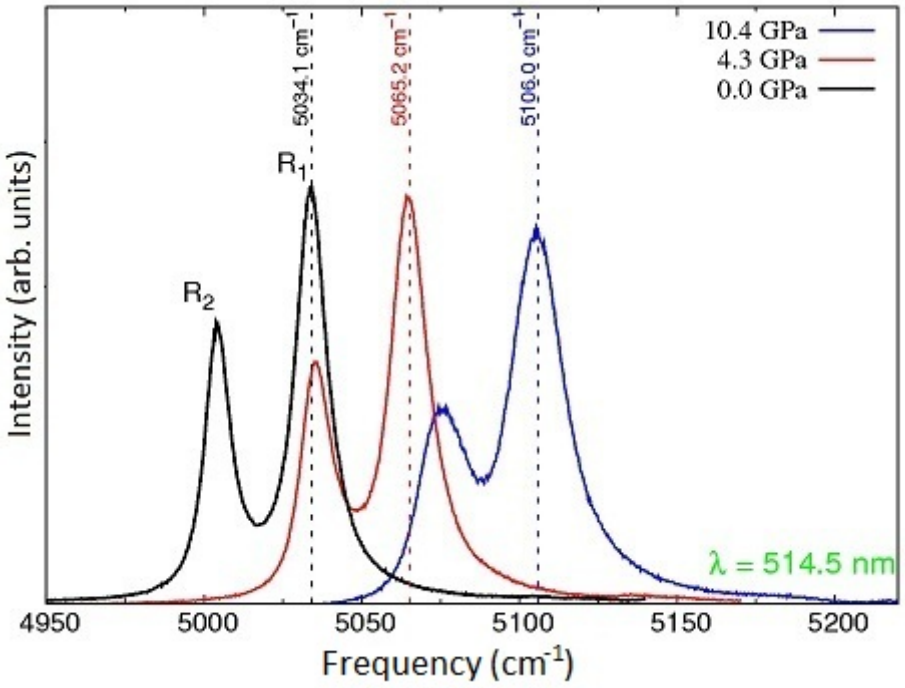

Figure 5.2: Frequency (in units of cm^{-1}) of the fluorescence ruby lines at different pressures. The peak positions are measured relative to the excitation light source, which in this case was a 514.5 nm laser line. Figure adapted from [60].

fore the pressure (in units of GPa) can be related to the R_1 frequency. Apart from acting as a pressure sensor, the R_1 frequency also indicates when the pressure becomes non-uniform (or non-hydrostatic) inside the chamber.

Since the maximum pressure reached in this experiment was 12.5 GPa, the calibration developed by Mao et al. [65] was adopted, as it holds up to 80 GPa. It is given by the expression

$$P(\text{GPa}) = \frac{A}{B}\left[\left(1 + \frac{\Delta\lambda}{\lambda_0}\right)^B - 1\right], \tag{5.1}$$

where A and B are 1904 and 7665, respectively, $\lambda_0 = 694,2$ nm is the wavelength of the R_1 fluorescence line at $P = 1$ bar, and $\Delta\lambda = (\lambda(P) - \lambda(P_0))$ is the displacement of ruby line with pressure.

In the régime close to 10 GPa, Eq. 5.1 is generally approximated to a linear expression through a binomial expansion, and the result is

$$P(GPa) = \frac{\Delta\omega(\mathrm{cm}^{-1})}{7.565}, \tag{5.2}$$

where $\Delta\omega$ is the difference between the R_1 frequency at some pressure P, and R_1 frequency obtained at the initial pressure of the experiment. The binomial expansion was performed for $\Delta\lambda/\lambda_0 \to 0$ within the definition $\omega = \lambda^{-1}$, the identity $\delta\lambda = (-1)\omega^{-2}\delta\omega$ was used.

It is known that every matter, even less dense gases such as hydrogen, helium, and neon exhibit a phase transition to solid state when compressed. This solid state phase can generate non uniform stress components inside the chamber [60]. The loss of the hydrostatic condition is generally associated to the superposition of the R_1 and R_2 lines, as well as to their considerable broadening [66].

5.1.2 The high-pressure Raman setup

The G/G/Teflon sample was initially cut into a strip of dimensions $\sim (0.5 \times 2)$ cm. The DAC used in this experiment is the pneumatically pressurized type shown in Fig. 5.1. The steel gasket (thickness of $\sim 300\ \mu$m) was carefully placed on top of one of the DAC's parts [Fig.5.1 (c)] so that its hole (with diameter approximately equal to $100\ \mu$m) was positioned above the center of the diamond's culet underneath. The strip with the transferred graphene was then positioned on top of the gasket in such a way that the sample was completely covering the gasket hole. After that, the two parts of the DAC were carefully snap together, resulting in the G/G/Teflon/gasket sandwiched between the two diamonds. The inlet/outlet line was then connected to the system.

The DAC operates as follows: a gas cylinder with Argon is connected to a controller which regulates the gas flux that enters or leaves the DAC pneumatic membrane. The inlet/outlet line is then connected to the controller. Now the pressure is increased or decreased inside the gasket hole by manipulating the valves of the controller, admitting or purging the gas inside of the pneumatic membrane. The inlet/outlet line was then connected to the controller, and the pressure was raised up to 4 bar so that the diamond could begin to deform the gasket. This would make the G/G/Teflon sample (that was sandwiched between the diamond and the gasket) to be cut and fall inside of the gasket hole. Afterward, the pressure was released back to the atmospheric level. The inlet/outlet line was disconnected first from the controller and second from the two snapped parts of the DAC. The two parts were then separated, the pressure transmitter medium (PTM) and the ruby were added to the gasket hole with the G/G/Teflon

inside of it. The two parts were than snapped together again, and all procedures repeated. The sample was finally loaded into the DAC, and the experiment was ready to begin.

The confocal Raman spectra were acquired using an alpha 300 system microscope (WITec, Ulm, Germany) equipped with a highly linear (0.02%) piezo-driven stage, and an objective lens from Nikon (20 ×, $NA = 0.40$). Two laser lines were used: (i) A Nd:YAG polarized laser ($\lambda = 532$ nm), (ii) an Argon laser ($\lambda = 488$ nm). The incident laser focused with a diffraction-limited spot size ($0.61\lambda/NA$) and the Raman signal was detected by a high sensitivity, back illuminated spectroscopic CCD located behind a 600 g/mm grating. The spectrometer used was an ultra-high throughput Witec UHTS 300 with up to 70% throughput, designed specifically for Raman microscopy.

For each pressure level, the fluorescence spectrum of ruby and the Raman spectrum of the sample were acquired for both 488 nm and 532 nm incident laser lines. The measurements were performed with powers of 10.1mW and 3mW for the 532 nm and 488 nm lasers, respectively. The integration time and number of accumulations were in average 60s and 3, respectively, for the 532 nm laser, and 90 s and 3 for the 488 nm laser. For each measurement, the spectrum of the ambient Hg light was also acquired. The correction for each spectrum (due to the possibility of displacement of the diffracting grating) was done by comparing the frequencies of the Hg light taken at the respective pressure P and at the initial pressure P_0. The calibration of all spectra at P_0 were performed by taking the Rayleigh line as reference.

It is important to point out that water undergoes a phase transition at ambient temperature from liquid water to Ice VI at $\sim$ 1 GPa and another one from Ice VI to Ice VII at $\sim$ 2 GPa [67]. However, measurements of the separation between the R_1 and R_2 ($R_1 - R_2$) fluorescence ruby lines and the shape and full width at half maximum of the R_1 line (Γ_{R_1}) indicate that these parameters do not vary appreciably throughout the experiment, which means that one can guarantee quasi-hydrostatic conditions up to the final pressure of 12.5 GPa. This observation is supported by the results of high-pressure experiments using water from Piermarini et. al [63] which could not detect effects due to localized nonhydrostatic stresses or to pressure gradients across their sample up to 20 GPa and from Olinger et. al [68] which found that H_2O supported a localized nonhydrostatic stress of only 0.6 GPa at 9.2 GPa and virtually no pressure gradient up to 10 GPa.

5.2 Results

In this section, we report the results obtained from the Raman spectrum of graphene supported by Teflon substrates at high-pressure conditions (up to 12.5 GPa). Figure 5.3 shows the evolution of the G band spectrum of a double-layer graphene obtained with two distinct laser lines, namely, 532 nm (green symbols), and 488 nm (blue symbols). All spectra were obtained using water as the pressure transmitter medium (PTM). The solid lines are the Lorentzian fit of the experimental data. Due to the superposition of the D and 2D band with the first- and second-order bond-stretching peaks from diamond, respectively, the G Band was the only observable Raman feature from graphene as can be seen in Fig. 5.4. All intensities in Fig. 5.3 were normalized to show the same value. As, expected, the G band frequency undergoes a blueshift with increasing pressure for both, 488 nm and 532 nm incident laser lines. Recalling that both, hydrostatic strain (Sec. 3.2.1) and doping effects (Sec. 3.2.2), cause a frequency blue-shift of the G band. The determination of these contributions separately could be obtained by analyzing the correlation between the G and 2D band frequencies (ω_G and ω_{2D}, respectively), as explained in Ref. [69]. However, a precise contribution of these effects is very difficult to be determined since it was not possible to observe the 2D band frequency variation with pressure.

Figure 5.5a shows the plot of ω_G as a function of the pressure P. From this figure it is clear that ω_G values obtained from the two different laser lines start to split from each other around 5 GPa. This result can be better visualized in Fig. 5.5b which shows the difference $\Delta\omega$ between the G band frequencies obtained with the 488 and 532 nm laser lines as a function of P. Between 5 and 9 GPa, the frequency difference is $\sim 3\text{cm}^{-1}$, becoming $\sim 7\text{cm}^{-1}$ for pressures above 9 GPa. This dispersion behavior is reversible upon pressure release, as shown in Fig. 5.5a.

It is interesting to notice the behavior of the $\omega_G \times P$ plots for the data obtained from the different laser lines. Both curves show a linear behavior until 6.0 GPa approximately, after which they both saturate until 9 GPa. At 9.5 GPa there is an abrupt increase in frequency followed by a saturation near the highest pressure. Another remarkable effect shown in Fig. 5.3 is the G band broadening when the pressure increases above 2GPa. This effect is clearly seen in Fig. 5.5c, which shows the plot of the G band's full-width at half-maximum (Γ_G) as a function of pressure. The plot also shows that, for pressures above 6 Gpa, the Γ_G increment is smaller for the blue laser (488 nm) when compared to the green (532 nm). Figure 5.5d exhibits the difference in Γ_G ($\Delta\Gamma_G$) between the data obtained with the 532 nm and 488 laser lines. The variation of Γ_G is partially reversible, with Γ_G reducing upon pressure release for both laser lines, but not

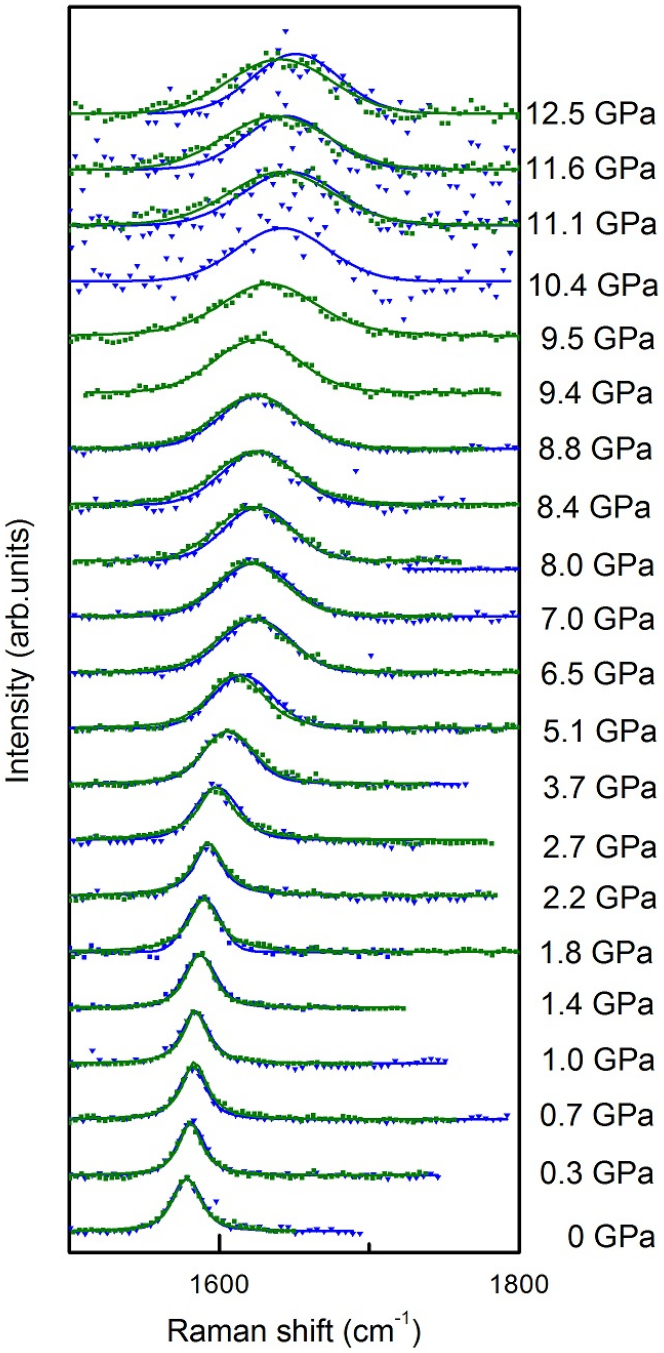

Figure 5.3: Spectra of a double-layer graphene obtained using two different laser lines: 532 nm (green symbols), and 488 nm (blues symbols). The spectra were obtained at different pressure values (indicated at the right), and water was used as PTM. All intensities were normalized to G band amplitude.

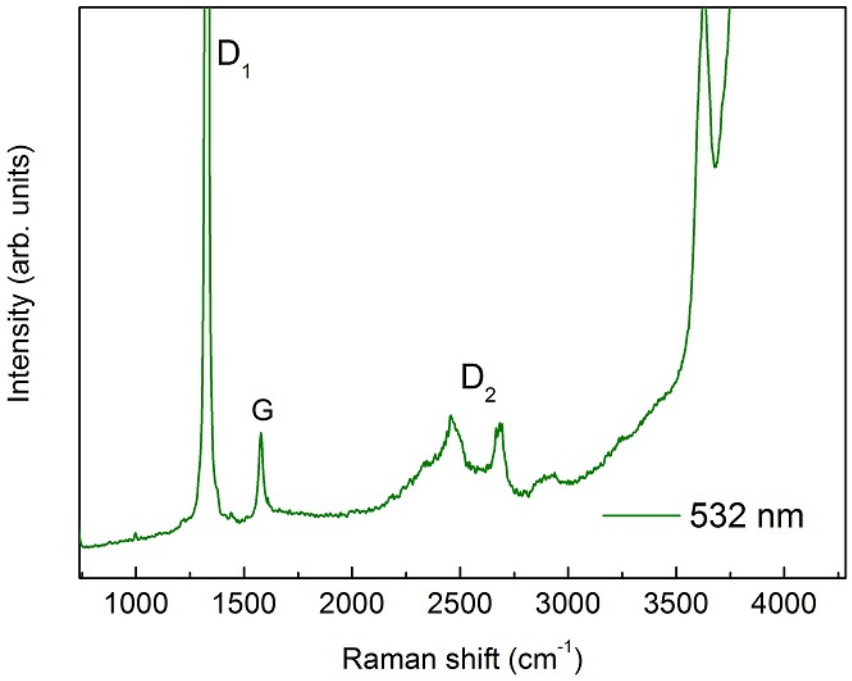

Figure 5.4: Spectrum of a double-layer graphene at ambient pressure inside the DAC using water as the PTM obtained with a 532 nm laser line. The G band is the only observable Raman feature of graphene since the D and 2D bands are superposed by the first (D_1) and second-order (D_2) diamond peaks.

completely returning to their original values. Moreover, Γ_G is smaller for the blue laser when compared to the green laser all over the pressure dropping trajectory.

Figure 5.6a shows the Raman spectrum of the double-layer graphene over the Teflon substrate (top spectrum), and the Raman spectrum obtained from the bare Teflon substrate (bottom spectrum). For the sake of comparison, two peaks of Teflon named as T_1 and T_2 in Fig. 5.6a , had their normalized frequencies [frequency(P) − frequency(P_0)] plotted as a function of pressure along with the normalized frequencies of the G band in Figs. 5.6b, 5.6c. Contrasting with graphene, no dispersion behavior with the excitation laser wavelength, or saturation plateaus were observed for both Teflon bands.

It was also observed the rise of a new band at $\sim$ 620cm^{-1} around 1 GPa and above as shown in Fig. 5.7a. After pressure release, this band disappears. Its frequency is plotted as a function of pressure for both laser lines in Fig. 5.7b, in which one can note an initial linear behavior up to 5 Gpa, followed by a saturation plateau occurring up to 9 GPa, which is a similar behavior as observed for the double graphene layer. At 9.5 GPa, an abrupt increase in frequency occurs, after which the frequency increases linearly with pressure for both laser lines. No systematic

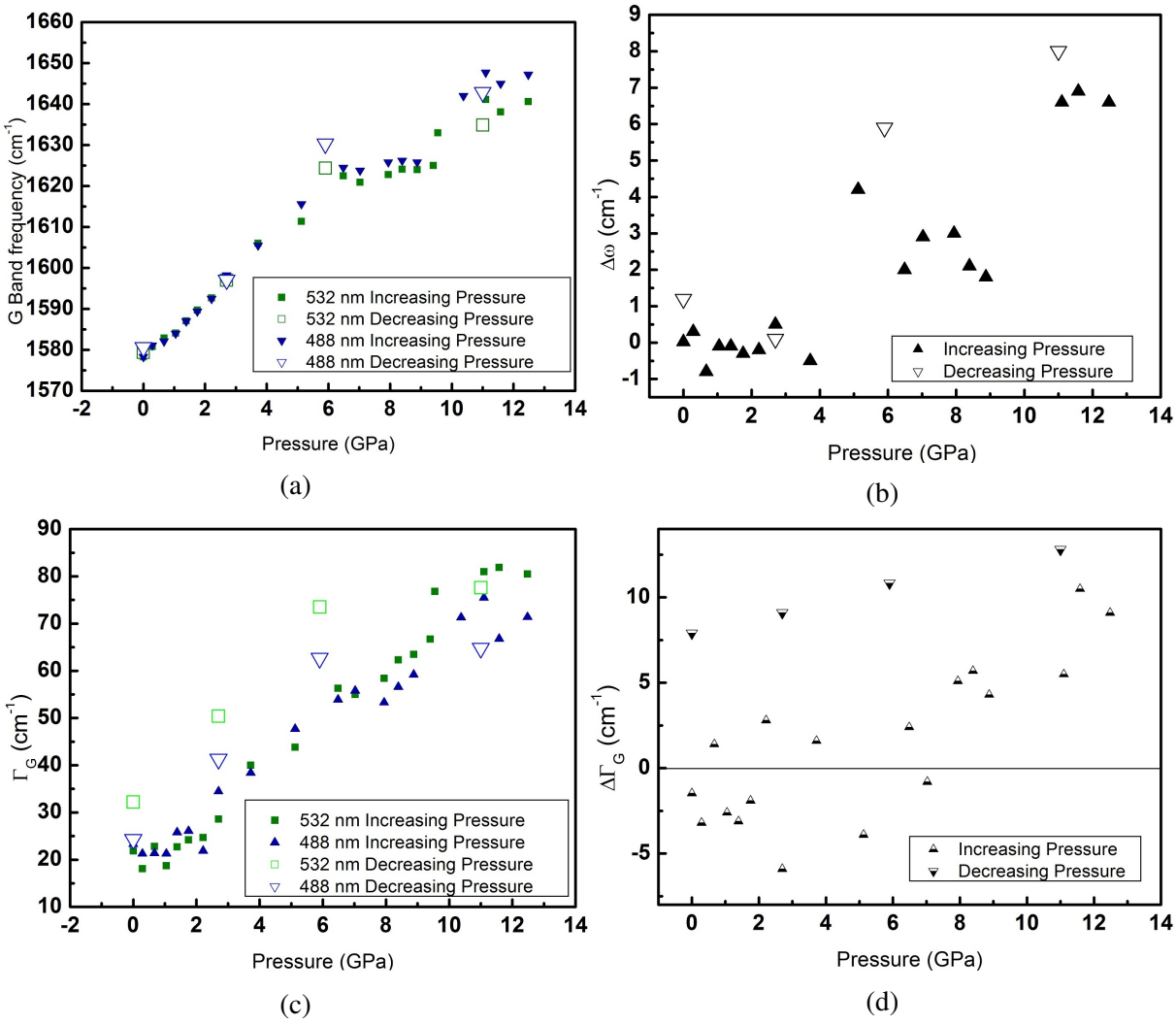

Figure 5.5: Evolution of G band parameters along a cyclic pressure run for both 488 and 532 nm laser lines. (a) The G band frequency, ω_G.(b) The difference between the values of ω_G obtained with the 488 and 532 nm laser lines. (c) Full width at half maximum, Γ_G.(d) Difference between the values of Γ_G obtained with the 532 nm and 488 laser lines.

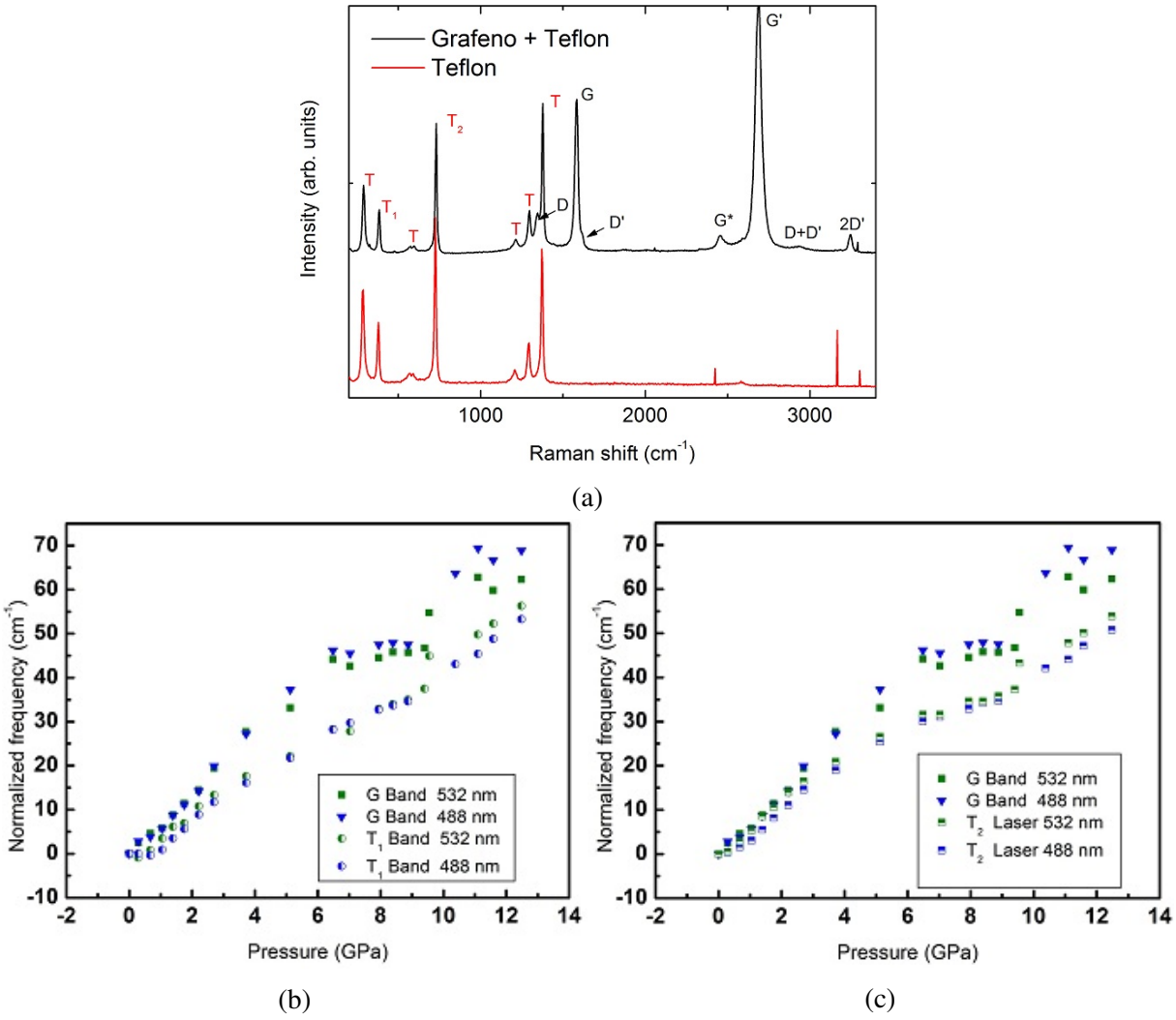

Figure 5.6: (a) Raman spectrum of the double-layer graphene over the Teflon substrate (top spectrum), and Raman spectrum obtained from the bare Teflon substrate (bottom spectrum). Two Teflon peaks named as T_1 and T_2 are identified. In (b) and (c) the normalized frequency, that is $\omega(P) - \omega(P_0)$, of the G band is compared to the normalized frequencies of the T_1 and T_2 bands, respectively.

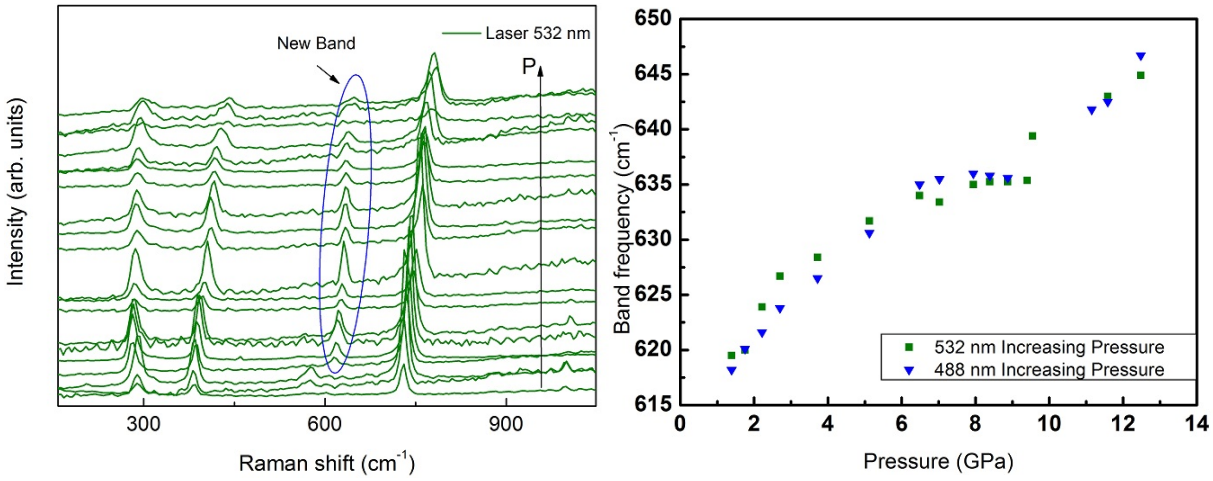

(a) (b)

Figure 5.7: (a) Raman spectra of the double layer graphene obtained at different values of pressure (increasing from bottom to top), and using the 532 nm laser line. The blue ellipse highlights the rise of a new at $\sim 620\text{cm}^{-1}$ for prassures above 1Gpa. (b) Frequency of the new band as a function of pressure for both 488 and 532 laser lines.

dispersive behavior with laser wavelength is observed.

5.3 Discussion

The main results observed in the last section are summarized as follows:

- Reversible dispersion of G peak with excitation laser wavelength starting at approx. 5 GPa.
- Increase in Γ_G with excitation laser wavelength at approx. 6 GPa.
- Change of régime of the $\omega_G \times P$ curve starting at approx. 6 GPa.
- Reversible broadening of Γ_G starting at 2 GPa.
- The rise of a new band at $\sim 620\text{cm}^{-1}$ at 1 GPa.

The first three results are consistent with a phase transition to a mixed $sp^2 - sp^3$ phase around $5 - 6$ GPa. Since the G band is associated with the in-plane bond stretching mode with E_{2g} symmetry, the fact that this peak is still measurable after that pressure range means that sp^2 carbons are still present in the system, otherwise there would be no G band scattering signal.

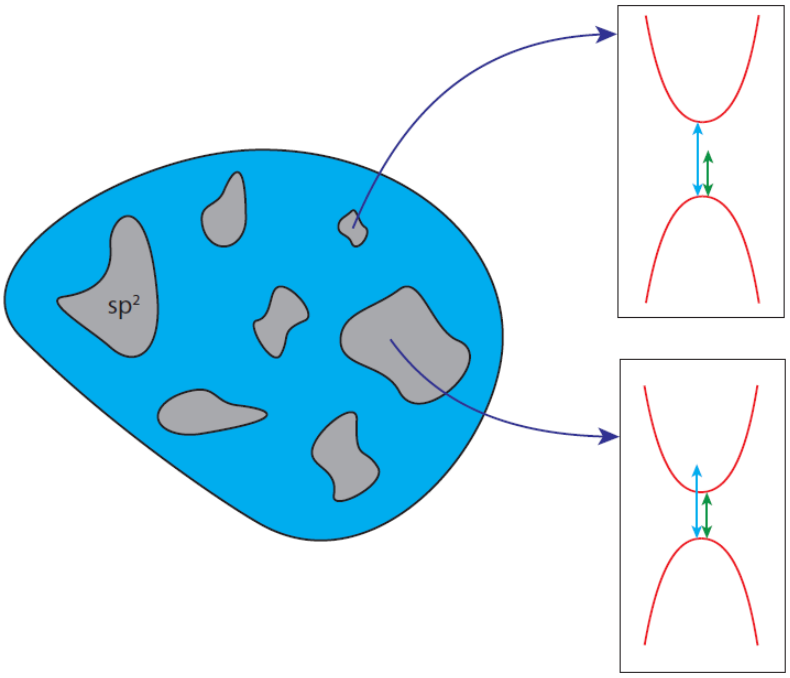

Figure 5.8: A mixed $sp^2 - sp^3$ system where sp^2 clusters (in gray) are inserted in a sp^3 matrix (in blue). The sp^2 clusters exhibit different band gaps and the smaller the cluster is, the wider is the band gap. Wider band gaps will become resonant with incident lasers with higher excitation energies (blue laser) and smaller band gaps will become resonant with incident lasers with lower excitation energies (green laser).

The G band dispersion with the laser wavelength, blueshifting for shorter wavelengths, is a strong indication of the presence of sp^3 carbon. The G peak does not disperse in graphite, nanographite, graphene or glassy carbon [70]. This band only disperses if the sample has the simultaneous presence of sp^2 and sp^3 clusters. In this case, the dispersion is proportional to the degree of disorder [70]. The reason for this behavior lies within the fact that there is a range of configurations with different band gaps and different phonon modes in the system due to the different domains with different fractions of sp^3 carbon as illustrated in Fig. 5.8. The presence of sp^3 clusters breaks the original translational symmetry of the graphene system, opening a band gap. The dispersion arises from a resonant selection of sp^2 clusters with wider π band gaps, corresponding to higher vibration frequencies [70].

However, to the best of the author's knowledge, there is no reference in the literature addressing why a wider band gap is associated to a higher vibration frequency in graphene. A possible explanation can be obtained by considering the breakdown on the Khon anomaly due to a gap opening in the electronic dispersion. As seen in Sec. 1.4.3, the phonon can decay into an electron-hole pair due to the electron-phonon (e-p) interaction. This interaction modifies the

phonon energy, which can be written as:

$$\hbar\omega = \hbar\omega_0 + \hbar\omega_p, \tag{5.3}$$

where $\hbar\omega_0$ is the unperturbed phonon frequency without considering the e-p interaction and $\hbar\omega_p$ is the quantum correction to the phonon frequency due this interaction. The latter term is given by second-order perturbation theory [28]

$$\hbar\omega_p = 2\sum_{\vec{k}} \frac{|\langle eh(\vec{k})|\mathscr{H}_{ep}|\omega\rangle|^2}{\hbar\omega_0 - E_e - E_h + i\Gamma} \times [f(E_h(\vec{k}) - E_F) - f(E_e(\vec{k}) - E_F)]. \tag{5.4}$$

In Eq. 5.4 the factor 2 comes from spin degeneracy, the term $\langle eh(\vec{k})|\mathscr{H}_{ep}|\omega\rangle$ is the matrix element for creating an electron hole pair with momentum $\vec{k}$ by the e-p interaction with a $\vec{q} = 0$ phonon, E_e (E_h) are the electron (hole) energy and Γ is the decay width. Due to the linear dispersion of graphene near the K point, the E_{2g} phonon with energy $\hbar\omega_q$, can resonantly decay into an electron-hole pair with energy $E_e - E_h$, as illustrated in Fig. 5.9 (a). In this process, the term in the denominator in Eq. 5.4 vanishes (except for the damping term Γ), and the correction term $\hbar\omega_p$ due to the e-p interaction is appreciable, giving rise to a strong softening of the E_{2g} phonon as shown by the black curve in Fig. 5.9 (b). This resonant decay of the phonon into an electron-hole pair gives rise to the Khon anomaly for the E_{2g} mode in graphene. However, when there is a gap opening, the contribution of the $\hbar\omega_p$ term to the phonon frequencies becomes less important since the electron-hole pair energy will become greater than the E_{2g} phonon energy in Eq. 5.4. And the wider the band gap is [Figs. 5.9 (c) and (d)], the greater this difference will be and the smaller the correction $\hbar\omega_p$ to the E_{2g} phonon will be, as can be seen in Fig. 5.9 (b).

The increase of Γ_G with the excitation laser wavelength can also be assigned to the formation of sp^3 bonds [70]. The reason is similar to that of ω_G dispersion: the sp^2 clusters with wider band gaps are selected by resonance for shorter laser wavelengths (higher excitation energies). However, again, it was not found any reference in the literature for the explanation for this phenomena. A possibility lies in the fact that, as seen in Sec. 1.4.3, the phonon decays into an electron-hole pair. Therefore, if ε_F is increased by a band gap which is wider that the phonon energy ($\hbar\omega_G$), the creation of the electron-hole pair will be forbidden due to the lack of states with half of the phonon energy ($\pm\hbar\omega_G/2$) and, according to the Uncertainty principle $\Delta E\Delta t \sim \hbar$, the lifetime of the phonon is increased, resulting in a decrease of Γ_G.

The change of régime of the $\omega_G \times P$ curve is an indication for the occurrence of phase transition. As seen in Sec. 3.2.1, the $\omega_G \times P$ curve has a contribution from mechanical strain. Therefore

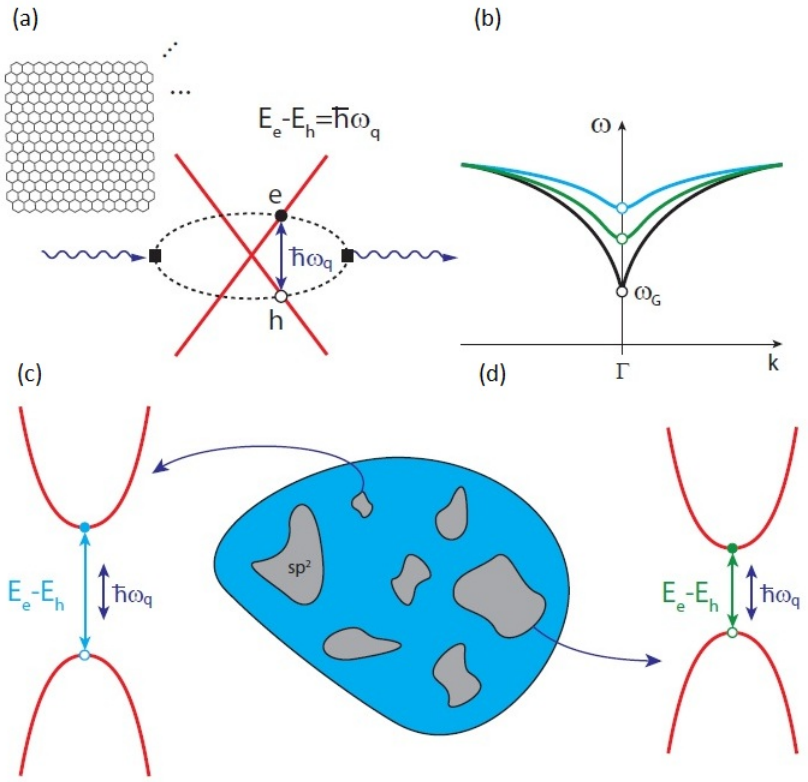

Figure 5.9: Illustration of the breakdown of the Khon anomaly in graphene due to a gap opening. (a) For the infinite graphene sheet, the electronic dispersion is linear close to the K point and the E_{2g} phonon with energy $\hbar\omega_q$, can resonantly decay into an electron-hole pair, with energy $E_e - E_h$. This strong e-p interaction gives rise to the anomalous softening of the E_{2g} phonon mode according to Eq. 5.4 and is represented by the black curve of the phonon dispersion of graphene in (b). (c)-(d) For finite size sp^2 clusters, the electronic dispersion exhibit band gaps and the correction to the E_{2g} phonon frequency due to the e-p interaction will be less significant. The wider the band gap is, the greater the difference between the energy of the electron-hole pair and the E_{2g} phonon will be. And according to Eq. 5.4, this will result in a smaller correction to the E_{2g} phonon frequency, as can be seen in the dispersion curves in (b) for the blue and green lasers.

if the elastic properties of the system are changed due to the formation of sp^3 bonds, this will affect the strain response of the system upon compression, thereby reflecting on the $\omega_G \times P$ curve. Even though the G band is associated with the displacement of carbon atoms in sp^2 clusters, the fact that these clusters are surrounded by sp^3 regions could change their strain response. From Eq. 3.27 the strain e_{ij} is evaluated as

$$e_{ij} = \sum_{k,l} \gamma_{ijkl}\sigma_{kl}.$$

If small bond length variations and distortions are neglected in these sp^2 clusters, the components of the elastic tensor γ_{ijkl} can be regarded as unaltered. However, the stress components σ_{kl} are no longer related to the hydrostatic pressure P because the system is no longer homogeneous and the stress within the material is now represented by a local stress field. Due to the strong covalent bonds of sp^3 structures, it is reasonable to assume that they possibly act as a stress screening for the sp^2 clusters. As a result, the sp^2 clusters are subjected to stress levels which are lower than the pressure of the system, and therefore a lower value for $\partial\omega_G/\partial P$ is expected. Indeed, a drastic reduction of $\partial\omega_G/\partial P$ is observed in Fig. 5.5a, being close to zero from $6-10$ GPa, followed by a rapid increase, and reaching zero level again for the last pressure measurements.

The broadening of Γ_G is consistent with the existence of a $sp^2 - sp^3$ phase because the reduction of the sp^2 area is accompanied by a relaxation of the $\vec{q} = 0$ rule according to the Uncertainty Principle $\Delta\vec{q}\Delta\vec{x}$. However the onset of this broadening starts at approximately 2 GPa, a much lower pressure than the transition threshold of $5 - 6$ GPa. There are at least two explanations for that observation. One explanation is that 2 GPa is the pressure of phase transition of water from Ice VI to Ice VII [67], therefore the broadening in Γ_G could be assigned to the presence of shear components in the medium. This can be understood by analyzing Eq. 3.25:

$$\omega = \omega_0 - 2\lambda\omega_0 e_h \pm \beta e_s,$$

where e_h and e_s are the hydrostatic and shear components of the strain, respectively. When the strain is not hydrostatic, both components contributes to the ω displacement, and the second term is the responsible for G band splitting. It is possible that a strain field is created in the graphene sample, with different regions being subjected to different shear components, therefore having different degrees of splitting. As a result, an overall broadening of the G band would be observed instead of a single split. However, it must be emphasized that these non- hydrostatic components must be small since water is quasi-hydrostatic up to 10 GPa.

Another possibility is that when water solidifies, it adheres to the graphene surface, and the closer contact may favor the formation of chemical bonds between OH groups (from water) and the carbon atoms of graphene. The crystal structure of Ice VII would allow only specific sites to be capable to react with graphene. The number of these sites would increase as the pressure is increased, and the distance between the water molecules and the carbon atoms is reduced. Each covalent bond formed between a carbon atom and an OH group would act as a point defect. If the number of point defects is increased, phonon confinement takes place. This is analogous to reducing the size of the sp^2 cluster, with the difference that some phonons are limited by the distance between point defects. This would relax the $\vec{q} = 0$ Raman selection rule, resulting in a increase of Γ_G. Moreover, the presence of point defects would increase the intensity of the $D^{'}$ Band ($\sim 1620\text{cm}^{-1}$ at ambient pressure). The $D^{'}$ peak is given by a double resonance intravalley process, that is, connecting two electron states belonging to the same Dirac cone around K or $K^{'}$ [17]. Since it is a one phonon process, it needs an elastic scattering by a defect for momentum conservation. Thus, the $D^{'}$ band is activated by the presence of defects, and the observed broadening of G band could actually have a contribution from the superposition of the G and $D^{'}$ bands. In fact, Hanfland et al. [3] observed an abrupt broadening of G band in graphite about 10 GPa, which they attributed to the formation of sp^3 bonds upon approaching the phase transition at 14 GPa.

Thus far, there are strong evidences for the formation of a mixeds $sp^2 - sp^3$ structures. But nothing has been said about the nature of the sp^3 configurations. We propose that the sp^3 structure formed is the diamondol [18]. The fact that the transitions were observed using a water PTM gives the main motivation for the diamondol hypothesis, since previous works using different PTM [15, 13, 14, 11, 12] did not report any phase transition at such lower pressures. Reference [18] propose two mechanisms for the formation of diamondol from water

$$C_N + 1/2\ H_2O + 1/4O2 \rightarrow C_NOH$$

$$C_N + H_2O \rightarrow C_NOH + 1/2H_2,$$

where C_N indicate the N carbon atoms of a few-layer graphene unit cell, and C_NOH indicate the unit cell of the resulting hydroxylated-diamondized structure. In our case (double layer graphene) $N = 4$, even though the two carbon layers do not present AA or AB stacking. In fact, the lack of AA or AB stacking is not a deterrent to the diamondol formation, since it can be formed independently of the relative orientation of the graphene layers [18].

Our hypothesis is that diamondol was synthesized at the pressure threshold of $5 - 6$ GPa, and above 9.5 GPa it gets detached from the Teflon substrate allowing the hydroxyl (OH) groups

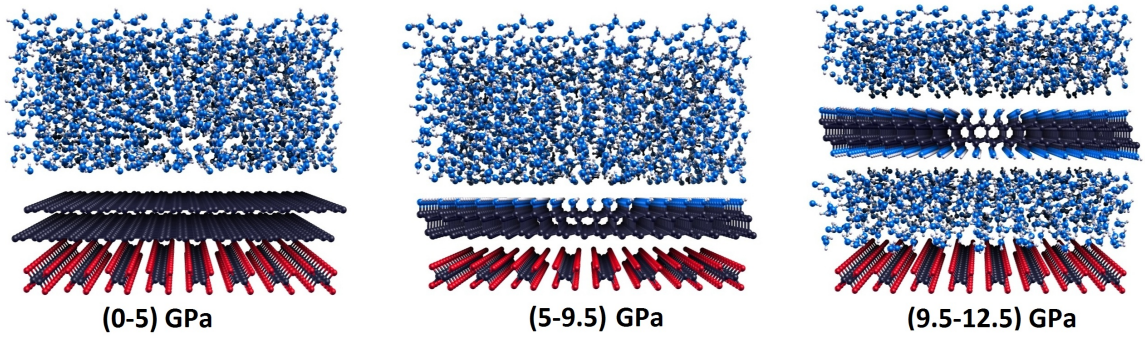

Figure 5.10: Representation of the different stages of the system during the high-pressure experiment. From 0 – 5 GPa, the system consists in the double layer graphene sitting on a Teflon substrate being compressed by the water PTM. At 5 – 6 GPa diamondol is synthesized and at 9.5 GPa, it detaches from the Teflon substrate resulting in a hydroxylation of the bottom layer.

to covalently bond to the carbon atoms of the bottom layer, which are extremely reactive due to the presence of dangling bonds. This process is illustrated in Fig. 5.10. This hypothesis is consistent with the content of sp^3 carbon inferred from the experimental data. The $\Delta\omega$ and $\Delta\Gamma$ quantities are proportional to the disorder degree of the system [70]. Since the starting point of our system is pure sp^2 hybridized atoms, the origin of the disorder can be assigned to the formation of sp^3 sites, therefore an increase of both $\Delta\omega$ and $\Delta\Gamma$ indicates an increase of the sp^3 content of the system. From Figs. 5.5b and 5.5d, the values for $\Delta\omega$ and $\Delta\Gamma$ at the pressure range of 9.5 – 12.5 GPa are greater than in the 5 – 9 GPa range, indicating a higher content of sp^3 carbon. In fact, diamondol would find itself in between the two hard surfaces of ice and Teflon. In this case, as the pressure is increased, the interactions between the diamondol surface and ice tend to be comparable or stronger (due to hydrogen bonding) to that between the diamondol and Teflon (Van deer Walls). Adding the contribution of non hydrostatic stress components to this factor , it is physically sound to suppose that diamondol should not be preferably adhered to Teflon with increasing pressure. This approach is in accordance with Proctor et al. [15] and Filintoglou et al. [14] who attributed some features observed in their experiments to the debonding and poor adherence of graphene on SiO_2 substrate with increasing pressure, and to the debonding of graphene upon solidification of the PTM, respectively. As a matter of fact, after the DAC opening the water inside the gasket hole evaporates. And in our case, we observed darker regions with varying intensity (Fig. 5.11a), in contrast with the homogeneous gray tone of the sample before the experiment [Fig. 4.3 (d)]. The Raman spectra confirm that the darker regions are actually graphene (Fig. 5.11b), indicating that the graphene (or the diamondol) have been detached from the Teflon substrate at some stage of the experiment being accumulated in the darker regions after the water evaporate.

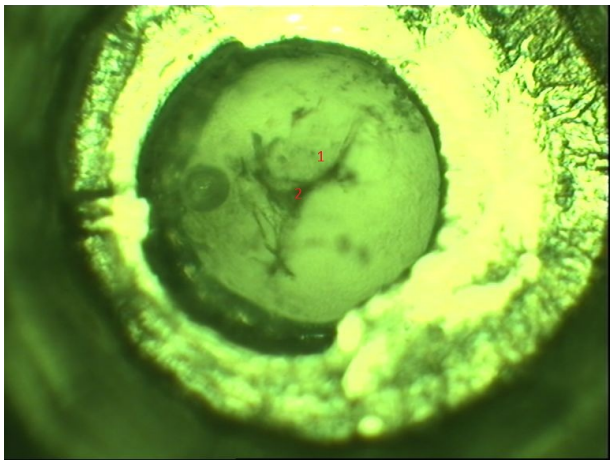

(a)

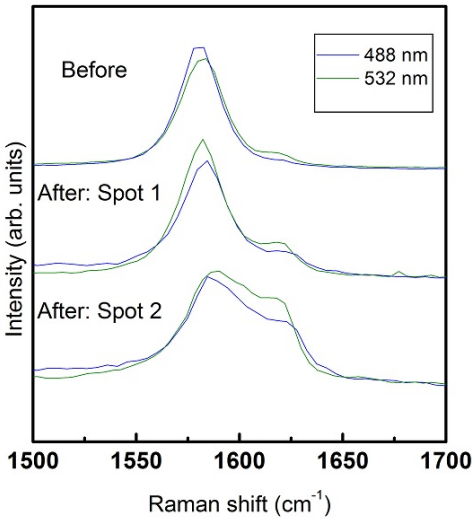

(b)

Figure 5.11: In (a): Image of the sample at ambient pressure after pressure run out of the DAC. Two different regions of the sample are highlighted: Spot 1 and Spot 2. In (b) :Comparison of the Raman spectra of graphene before and after the high pressure run out of the DAC. The spectra after the high pressure run were acquired at Spot 1 and Spot 2. All intensities were normalized to the same arbitrary value.

One can raise the question of whether the presence of sp^3 carbon could be generated by a amorphization process due to laser heating. However, this hypothesis can be discarded because the ω_G dispersion is reversible upon pressure release, as shown in Figs. 5.5a and 5.11b. The later compares the G band spectra of the samples obtained before and after the high-pressure experiment takes place, at ambient pressure out of the DAC. The results reported in Ref. [18] also point to a reversible formation of diamondol.

To further test the diamondol hypothesis, mono and double layer CVD graphene on Teflon substrates were compressed with a DAC using water and Nujol (mineral oil) as the PTMs, respectively. The same experimental procedures detailed in Sec. 5.1.2 were repeated in both cases. The results are exhibited in Figs. 5.12 and 5.13. We did not observe a systematic frequency dispersion for the G band with excitation laser wavelength, neither for the monolayer in water (mono/H_2O), (Figs. 5.12a and 5.12b) nor to the double layer in Nujol (double/oil) (Figs. 5.12c and 5.12d). Moreover, it was not observed any net decrease in Γ_G for the 488 nm laser line when compared to the 532 nm in both cases (Figs. 5.13a and 5.13b for the mono/water, and Figs. 5.13c and 5.13d for the double layer/Nujol).

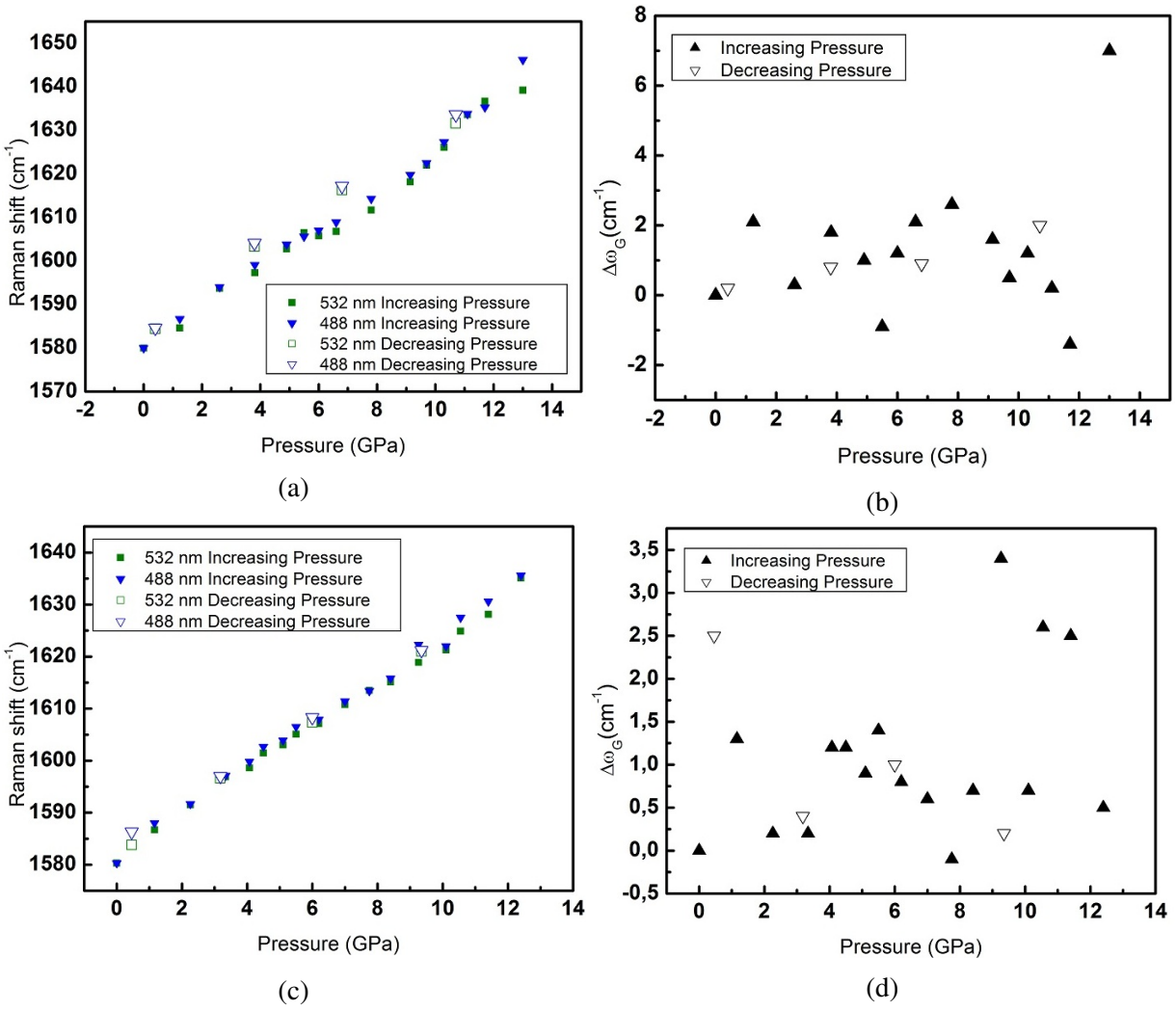

Figure 5.12: Plots of G band frequency (ω_G) and G band dispersion ($\Delta\omega_G$) as a function of pressure for two different systems. In (a) and (b): mono-layer graphene on Teflon with water as the PTM. In (c) and (d): double- layer graphene on Teflon with mineral oil (Nujol) as the PTM.

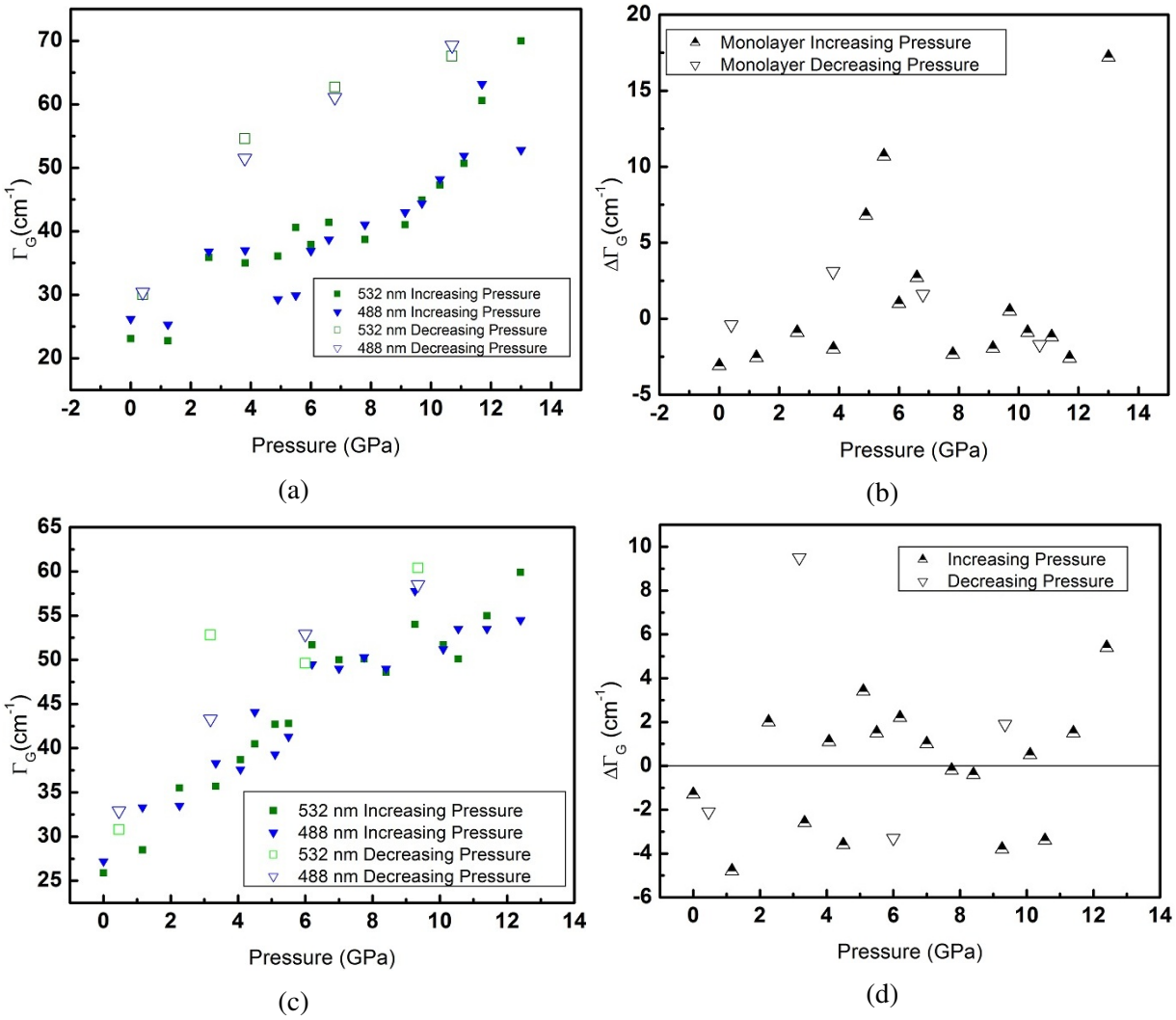

Figure 5.13: Plots of G band full width at half maximum (Γ_G) and Γ_G dispersion ($\Delta\Gamma_G$) as a function of pressure for two different systems. In (a) and (b): mono-layer graphene on Teflon using water as the PTM. In (c) and (d): double-layer graphene on Teflon with mineral oil (Nujol) as the PTM.

These observations are in agreement with the diamondol hypothesis, since they reinforce that the changes in the Raman spectra that give evidence for the diamondol formation can only be observed for double layer graphene with water as PTM. In fact, the diamondization of single layer graphene in water is expected to occur at much higher pressure levels then the maximum achieved in the present work [18]. Besides, in order to achieve a phase transition to the sp^3 phase within the pressure range employed in the current work, the use of water as the PTM is absolutely necessary, since it provides the hydroxyl groups which covalently bond to the carbon atoms of the top layer, canceling the dangling bonds, and stabilizing the whole structure.

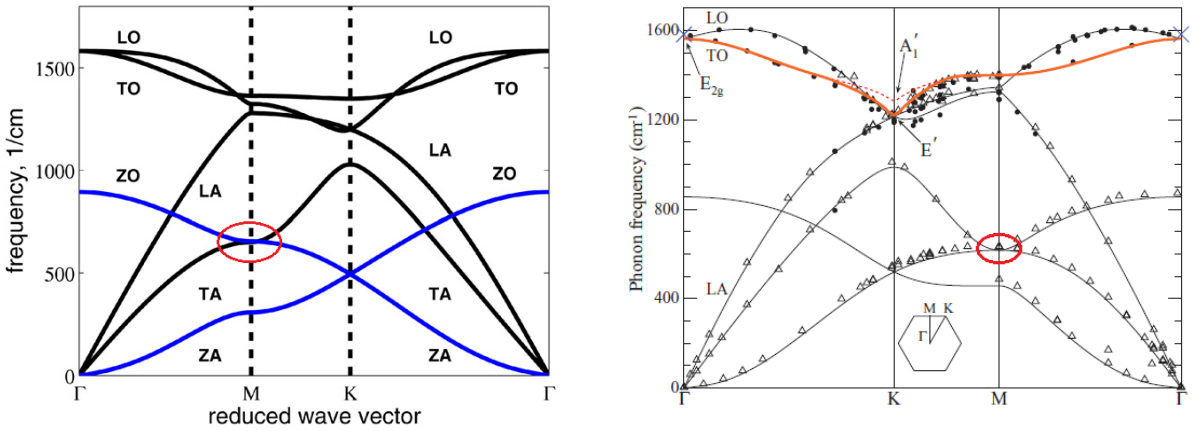

(a) (b)

Figure 5.14: Phonon dispersions of graphene featuring the out of plane (OZ) optical mode at the M point of graphene's Brillouin Zone with frequency around 620cm^{-1}. In (a) : Figure adapted from reference [71]. In (b): Figure adapted from reference [72]

As a final remark, we report for the rise of a new band at $\sim$ 620cm^{-1} appearing at and above approximately 1 GPa. The initial hypothesis was that this peak corresponds to an Ice VI mode since 1 GPa is the transition pressure from liquid water to ice VI [67]. However, this peak was also detected for the mono/H_2O and double/oil samples, which then excluded this initial hypothesis. Another hypothesis is that this mode is associated to the out-of-plane (OZ) optical phonon branch at the M point of graphene's B.Z at $\sim$ 620cm^{-1} [71, 72] (Figs. 5.14a and 5.14b). Since this is a $\vec{q} \neq 0$ phonon, a defect scattering is necessary for momentum conservation. However, no report of the presence of this mode was found in the literature. A third hypothesis is that this mode could actually be the superposition of the small peaks of Teflon around 574 and 596cm^{-1} . This is the least probable hypothesis, because the new peak rises at 620cm^{-1}. Thus, if the third hypothesis was true, the small peaks would have to be shifted by $20 - 40$cm^{-1} in a pressure interval of 0.3 GPa. Such abrupt discontinuity would be possible if Teflon went through a phase transition, however, the change should also be observed in the Raman spectra of the T_1 and T_2 Teflon peaks, which is not the case (Fig. 5.6b and 5.6c). Therefore, from all hypothesis, the second one seems to be the most reliable, specially by taking into account the comparison between the frequency $\times$ pressure plots of the new peak and the G band. However further experiments are needed for a solid understanding about the nature of this new mode.

Chapter 6

Conclusion

In this work, the effect of high pressures on double layered graphene supported by a Teflon substrate was studied via Raman spectroscopy using water as the pressure transmitting media (PTM). The Raman spectra were acquired with both 488 and 532 nm excitation laser lines. Initially, a detailed study of the electronic and vibrational properties of graphene, as well as the interaction between both, was performed. This studied was followed by an investigation (via a quantum approach) of the Raman scattering process and the mechanisms that give rise to strong perturbations of the G band frequency and shape. A value for the slope of the G band frequency with pressure ($\partial\omega_G/\partial P$) of $\sim$ 5cm^{-1}/GPa was obtained via a combination of theoretical analysis and experimental data. This value agrees with experimental observations for free-standing graphene samples subjected to high pressures.

Due to the experimental conditions, the G band was the only Raman feature of graphene analyzed in the high-pressure experiments. As expected, G band frequency (ω_G) blueshifted with increasing pressure, because it is sensitive to both strain and doping effects. However, a precise contribution from each of these effects to ω_G could not be determined due to the lack of information about the 2D band signal. The experimental results provide strong evidence of a phase transition from a pure sp^2 to a $sp^2 - sp^3$ mixed structure from 5 − 6 GPa. The main evidences are the dispersion of the G band with excitation laser wavelength (blueshifting for shorter wavelengths), the enlargement of G band's full width at half maximum (Γ_G) with laser wavelengths and the change of slope of the $\omega_G \times P$ curve. The origin of the dispersion of

ω_G with laser wavelength comes from a resonant selection process where the sp^2 clusters with wider band gaps are selected for shorter excitation wavelength. The wider the band gap is, the higher the G band frequency takes. The explanation provided to that is that the wider the band gap is, the less significant the correction to the E_{2g} phonon due to the electron-phonon interaction will be. The changes on Γ_G with the excitation laser wavelength also comes from a resonant selection process and the explanation given to tis phenomena is that a wider band gap increases the phonon lifetime by prohibiting its decay into an electron hole pair. The change of régime of the $\omega_G \times P$ curve, achieving two plateaus occurring in the pressure ranges from 6 to 9.5 GPa and from 10 to 12.5 Gpa, was attributed to the change in the elastic properties of the system due to the formation of sp^3 bonds. A broadening of Γ_G was also observed, and this is consistent with the clustering of the sp^2 phase, which relax the $\vec{q} = 0$ selection rule. However this broadening started at a relatively low pressure (around 2 GPa), which is bellow the expected transition threshold. The reason for this broadening might be related to the loss of hydrostacity of the medium or to the formation of sp^3 bonds acting as point defects, leading to phonon confinement evidenced by a simultaneous increase of the defect-induced D' band.

We hypothesized that the sp^3 structure formed was the diamondol, a theoretically proposed 2D hydroxylated diamond and experimentally studied in Ref. [18]. We propose that the top layer was hydroxylated at $5-6$ GPa followed by a detach from the Teflon substrate at 9.5 GPa, which led to a hydroxylation of the bottom layer. This hypothesis is consistent with the sp^3 content of the system inferred from $\Delta\omega_G$ and $\Delta\Gamma_G$ data, and also with the fact that graphene was indeed found to be detached from Teflon in some regions after the DAC was opened, and the water was evaporated. To test the diamondol hypothesis, mono and double layer CVD graphene on a Teflon substrate were compressed with a DAC using water and Nujol (mineral oil) as PTMs, respectively. No dispersion of the G band, change in the $\omega_G \times P$ curve or any net decrease in Γ_G with excitation wavelength were observed for both systems, which agrees with the diamondol hypothesis.

It was also observed the rise of a new band at $\sim 620\text{cm}^{-1}$ under 1 GPa and above. Two possibilities were raised about the origin of this band. It could either be a mode from Teflon or graphene. The hypothesis that it is a graphene mode is the most reasonable due to the identification of a mode occurring at the same frequency in the out of plane (OZ) optical branch at point M in the phonon dispersion of graphene , for which a high-density of states is expected due to its flat dispersion. Also, there is a resemblance between the $\omega_G \times P$ curves of the new band and graphene. No previous report about the appearance of this band in the Raman spectrum of graphene was

found in literature.

To confirm the diamondol hypothesis, the duplicate of the original experiment should be carried out. Also, first principle DFT calculations could be performed to understand if diamondol would be possible to exist at the pressure levels achieved in the current experiment. Further experiments should also be performed to understand the origin of the new band at $\sim 620\text{cm}^{-1}$. A simple experiment would be to compress Teflon (with no graphene on it) using water as the PTM, since the absence of this peak would be a strong evidence that it is indeed a graphene mode.

If the diamondol hypothesis is confirmed, this work will open up directions for synthesizing new 2D materials with remarkable properties under high pressure conditions. Indeed new electronic devices able to explore such high pressure transitions could be designed as well as new pressure sensors. For instance, a Pressure Effect Transistor (PET), in which the current is modulated by the application of a local pressure instead of an electric field as in a Field Effect Transitor (FET), could be envisioned. Moreover, one could think of a combination of High Pressure Raman and quantum transport measurements by the construction of a DAC which allows transport measurements, providing a broad picture of the effects of doping and strain in materials subjected to high pressures.

Bibliography

[1] Takehiko Yagi, Wataru Utsumi, Masa-aki Yamakata, Takumi Kikegawa, and Osamu Shimomura. High-pressure in situ x-ray-diffraction study of the phase transformation from graphite to hexagonal diamond at room temperature. *Physical Review B*, 46(10):6031, 1992. 1

[2] Wendy L Mao, Ho-kwang Mao, Peter J Eng, Thomas P Trainor, Matthew Newville, Chichang Kao, Dion L Heinz, Jinfu Shu, Yue Meng, and Russell J Hemley. Bonding changes in compressed superhard graphite. *Science*, 302(5644):425–427, 2003. 1

[3] M Hanfland, H Beister, and K Syassen. Graphite under pressure: Equation of state and first-order raman modes. *Physical Review B*, 39(17):12598, 1989. 1, 89

[4] Wataru Utsumi and Takehiko Yagi. Light-transparent phase formed by room-temperature compression of graphite. *Science*, 252(5012):1542–1544, 1991. 1

[5] M Hanfland, K Syassen, and R Sonnenschein. Optical reflectivity of graphite under pressure. *Physical Review B*, 40(3):1951, 1989. 1

[6] RB Aust and HG Drickamer. Carbon: A new crystalline phase. *Science*, 140(3568):817–819, 1963. 1

[7] Quan Li, Yanming Ma, Artem R Oganov, Hongbo Wang, Hui Wang, Ying Xu, Tian Cui, Ho-Kwang Mao, and Guangtian Zou. Superhard monoclinic polymorph of carbon. *Physical review letters*, 102(17):175506, 2009. 1

[8] Koichiro Umemoto, Renata M Wentzcovitch, Susumu Saito, and Takashi Miyake. Body-centered tetragonal c_4: A viable sp^3 carbon allotrope. *Physical review letters*, 104(12):125504, 2010. 1

[9] Jian-Tao Wang, Changfeng Chen, and Yoshiyuki Kawazoe. Low-temperature phase transformation from graphite to sp^3 orthorhombic carbon. *Physical review letters*, 106(7):075501, 2011. 1

[10] Maximilian Amsler, José A Flores-Livas, Lauri Lehtovaara, Felix Balima, S Alireza Ghasemi, Denis Machon, Stéphane Pailhès, Alexander Willand, Damien Caliste, Silvana Botti, et al. Crystal structure of cold compressed graphite. *Physical review letters*, 108(6):065501, 2012. 1

[11] Shuangchen Lu, Mingguang Yao, Xigui Yang, Quanjun Li, Junping Xiao, Zhen Yao, Linhai Jiang, Ran Liu, Bo Liu, Shuanglong Chen, et al. High pressure transformation of graphene nanoplates: A raman study. *Chemical Physics Letters*, 585:101–106, 2013. 1, 2, 89

[12] SM Clark, Ki-Joon Jeon, Jing-Yin Chen, and Choong-Shik Yoo. Few-layer graphene under high pressure: Raman and x-ray diffraction studies. *Solid State Communications*, 154:15–18, 2013. 1, 2, 89

[13] Jimmy Nicolle, Denis Machon, Philippe Poncharal, Olivier Pierre-Louis, and Alfonso San-Miguel. Pressure-mediated doping in graphene. *Nano letters*, 11(9):3564–3568, 2011. 1, 2, 89

[14] K Filintoglou, N Papadopoulos, J Arvanitidis, D Christofilos, O Frank, M Kalbac, J Parthenios, G Kalosakas, C Galiotis, and K Papagelis. Raman spectroscopy of graphene at high pressure: Effects of the substrate and the pressure transmitting media. *Physical Review B*, 88(4):045418, 2013. 1, 2, 62, 89, 90

[15] John E Proctor, Eugene Gregoryanz, Konstantin S Novoselov, Mustafa Lotya, Jonathan N Coleman, and Matthew P Halsall. High-pressure raman spectroscopy of graphene. *Physical Review B*, 80(7):073408, 2009. 1, 2, 56, 89, 90

[16] LM Malard, MA Pimenta, G Dresselhaus, and MS Dresselhaus. Raman spectroscopy in graphene. *Physics Reports*, 473(5):51–87, 2009. 2

[17] Andrea C Ferrari and Denis M Basko. Raman spectroscopy as a versatile tool for studying the properties of graphene. *Nature nanotechnology*, 8(4):235–246, 2013. 2, 89

[18] Ana PM Barboza, Marcos HD Guimarães, Daniel VP Massote, Leonardo C Campos, Newton M Barbosa Neto, Luiz G Cançado, Rodrigo G Lacerda, Helio Chacham, Mario SC

Mazzoni, and Bernardo RA Neves. Room-temperature compression-induced diamondization of few-layer graphene. *Advanced Materials*, 23(27):3014–3017, 2011. 2, 3, 89, 91, 93, 96

[19] A Greenville Whittaker. Carbyne forms of carbon: evidence for their existence. *Science*, 229(4712):485–486, 1985. 5

[20] Riichiro Saito, Gene Dresselhaus, Mildred S Dresselhaus, et al. *Physical properties of carbon nanotubes*, volume 4. World Scientific, 1998. 5, 14, 16, 17, 19, 20, 22, 23, 24, 25

[21] David Jeffrey Griffiths and Edward G Harris. *Introduction to quantum mechanics*, volume 2. Prentice Hall New Jersey, 1995. 5

[22] Mikhail I Katsnelson and Mikhail Iosifovich Katsnelson. *Graphene: carbon in two dimensions*. Cambridge University Press, 2012. 6, 8

[23] Paula Yurkanis Bruice. Organic chemistry. http://wps.prenhall.com/wps/media/objects/724/741576/chapter_01.html. Accessed: 03-10-2015. 10, 11

[24] The university of manchester-open eduacational resources-physics-advanced quantum mechanis 2. http://oer.physics.manchester.ac.uk/AQM2/Notes/Notes-6.4.html. Accessed:07-21-2014. 12

[25] Phaedon Avouris. Graphene: electronic and photonic properties and devices. *Nano letters*, 10(11):4285–4294, 2010. 17

[26] RA Jishi, L Venkataraman, MS Dresselhaus, and G Dresselhaus. Phonon modes in carbon nanotubules. *Chemical Physics Letters*, 209(1):77–82, 1993. 25

[27] T Aizawa, R Souda, S Otani, Y Ishizawa, and C Oshima. Bond softening in monolayer graphite formed on transition-metal carbide surfaces. *Physical Review B*, 42(18):11469, 1990. 25

[28] Ado Jorio, Mildred S Dresselhaus, Riichiro Saito, and Gene Dresselhaus. *Raman spectroscopy in graphene related systems*. John Wiley & Sons, 2010. 26, 39, 49, 54, 55, 58, 59, 86

[29] Philip L Taylor and Olle Heinonen. *A quantum approach to condensed matter physics*. Cambridge University Press, 2002. 26, 27, 30, 32, 33

[30] W Kohn. Image of the fermi surface in the vibration spectrum of a metal. *Physical Review Letters*, 2(9):393, 1959. 34

[31] S Piscanec, M Lazzeri, Francesco Mauri, AC Ferrari, and J Robertson. Kohn anomalies and electron-phonon interactions in graphite. *Physical review letters*, 93(18):185503, 2004. 34, 64

[32] Daniela Lopes Mafra. *Using inelastic scattering of light to understand the nature of electron-phonon interactions and phonon self-energy renormalizations in graphene materials*. PhD thesis, Departamento de Física-Universidade Federal de Minas Gerais, 2012. 34

[33] William Hayes and Rodney Loudon. *Scattering of light by crystals*. Wiley-Interscience Publications, 1978. 36

[34] Rodney Loudon. *The quantum theory of light*. Oxford university press, 1983. 36, 38, 39, 41, 42, 44

[35] Luiz Gustavo de Oliveira Lopes Cançado. *Raman Spectroscopy of Nanographites*. PhD thesis, Departamento de Física-Universidade Federal de Minas Gerais, 2006. 37, 54

[36] Leandro Malard Moreira. *Raman Spectroscopy of graphene: probing phonons, electrons and electron-phonon interactions*. PhD thesis, Departamento de Física-Universidade Federal de Minas Gerais, 2009. 38

[37] Peter Y Yu and Manuel Cardona. *Fundamentals of semiconductors*. Springer, 1996. 49, 50

[38] Mingyuan Huang, Hugen Yan, Changyao Chen, Daohua Song, Tony F Heinz, and James Hone. Phonon softening and crystallographic orientation of strained graphene studied by raman spectroscopy. *Proceedings of the National Academy of Sciences*, 106(18):7304–7308, 2009. 55, 56, 57, 62

[39] M, M Cardona, and G Güntherodt. Light scattering in solids iv. *Topics in Applied Physics*, 54, 1984. 55

[40] S Ganesan, AA Maradudin, and J Oitmaa. A lattice theory of morphic effects in crystals of the diamond structure. *Annals of Physics*, 56(2):556–594, 1970. 56

[41] H Sakata, G Dresselhaus, MS Dresselhaus, and M Endo. Effect of uniaxial stress on the raman spectra of graphite fibers. *Journal of applied physics*, 63(8):2769–2772, 1988. 56

[42] S Reich, H Jantoljak, and C Thomsen. Shear strain in carbon nanotubes under hydrostatic pressure. *Physical Review B*, 61(20):R13389, 2000. 58, 62

[43] Jakob Zabel, Rahul R Nair, Anna Ott, Thanasis Georgiou, Andre K Geim, Kostya S Novoselov, and Cinzia Casiraghi. Raman spectroscopy of graphene and bilayer under biaxial strain: bubbles and balloons. *Nano letters*, 12(2):617–621, 2012. 60, 62

[44] TMG Mohiuddin, A Lombardo, RR Nair, A Bonetti, G Savini, R Jalil, N Bonini, DM Basko, C Galiotis, N Marzari, et al. Uniaxial strain in graphene by raman spectroscopy: G peak splitting, grüneisen parameters, and sample orientation. *Physical Review B*, 79(20):205433, 2009. 62

[45] OL Blakslee, DG Proctor, EJ Seldin, GB Spence, and T Weng. Elastic constants of compression-annealed pyrolytic graphite. *Journal of Applied Physics*, 41(8):3373–3382, 1970. 62

[46] Otakar Frank, Georgia Tsoukleri, Ibtsam Riaz, Konstantinos Papagelis, John Parthenios, Andrea C Ferrari, Andre K Geim, Kostya S Novoselov, and Costas Galiotis. Development of a universal stress sensor for graphene and carbon fibres. *Nature Communications*, 2:255, 2011. 62

[47] Simone Pisana, Michele Lazzeri, Cinzia Casiraghi, Kostya S Novoselov, Andre K Geim, Andrea C Ferrari, and Francesco Mauri. Breakdown of the adiabatic born–oppenheimer approximation in graphene. *Nature materials*, 6(3):198–201, 2007. 63, 64, 65, 66

[48] Anindya Das, S Pisana, B Chakraborty, S Piscanec, SK Saha, UV Waghmare, KS Novoselov, HR Krishnamurthy, AK Geim, AC Ferrari, et al. Monitoring dopants by raman scattering in an electrochemically top-gated graphene transistor. *Nature nanotechnology*, 3(4):210–215, 2008. 63

[49] Kostya S Novoselov, Andre K Geim, SV Morozov, D Jiang, Y_ Zhang, SV Dubonos, IV Grigorieva, and AA Firsov. Electric field effect in atomically thin carbon films. *science*, 306(5696):666–669, 2004. 63

[50] KSA Novoselov, Andre K Geim, SVb Morozov, Da Jiang, MI Katsnelson IV Grigorieva, SV Dubonos, and AA Firsov. Two-dimensional gas of massless dirac fermions in graphene. *nature*, 438(7065):197–200, 2005. 63

[51] Yuanbo Zhang, Yan-Wen Tan, Horst L Stormer, and Philip Kim. Experimental observation of the quantum hall effect and berry's phase in graphene. *Nature*, 438(7065):201–204, 2005. 63

[52] Michele Lazzeri and Francesco Mauri. Nonadiabatic kohn anomaly in a doped graphene monolayer. *Physical review letters*, 97(26):266407, 2006. 63, 64

[53] Max Born and Robert Oppenheimer. Zur quantentheorie der molekeln. *Annalen der Physik*, 389(20):457–484, 1927. 64

[54] JM Ziman. *Electrons and phonons*. Oxford University Press, London, 1961. 64

[55] H Scott Fogler. *Elements of chemical reaction engineering*. Prentice-Hall International Inc., New Jersey, 2009. 68

[56] Xuesong Li, Weiwei Cai, Jinho An, Seyoung Kim, Junghyo Nah, Dongxing Yang, Richard Piner, Aruna Velamakanni, Inhwa Jung, Emanuel Tutuc, et al. Large-area synthesis of high-quality and uniform graphene films on copper foils. *Science*, 324(5932):1312–1314, 2009. 68, 69

[57] Keun Soo Kim, Yue Zhao, Houk Jang, Sang Yoon Lee, Jong Min Kim, Kwang S Kim, Jong-Hyun Ahn, Philip Kim, Jae-Young Choi, and Byung Hee Hong. Large-scale pattern growth of graphene films for stretchable transparent electrodes. *Nature*, 457(7230):706–710, 2009. 68

[58] Peter W Sutter, Jan-Ingo Flege, and Eli A Sutter. Epitaxial graphene on ruthenium. *Nature materials*, 7(5):406–411, 2008. 68

[59] Luiz GP Martins, Yi Song, Tingying Zeng, Mildred S Dresselhaus, Jing Kong, and Paulo T Araujo. Direct transfer of graphene onto flexible substrates. *Proceedings of the National Academy of Sciences*, 110(44):17762–17767, 2013. 71, 72

[60] Acrísio Lins de Aguiar. *Nanotubos de Carbono de Parede Dupla submetidos a condiçoes extremas de Altas Pressões e Altas Temperaturas*. PhD thesis, Departamento de Física-Universidade Federal do Ceará, 2012. 74, 76, 77

[61] Almax easyLab Limited. *Diacell μScopeDAC HT(G) Users Guide*. Almax easyLab Limited, University of Reading Science and Technology Center, Whiteknights Road Early Gate Reading, RG6 6BZ, Berkshire, United Kingdom, November 2013. Issue 1.3. 75

[62] HK Mao, PM Bell, JW t Shaner, and DJ Steinberg. Specific volume measurements of cu, mo, pd, and ag and calibration of the ruby r_1 fluorescence pressure gauge from 0.06 to 1 mbar. *Journal of Applied Physics*, 49(6):3276–3283, 1978. 75

[63] GJ Piermarini, S Block, and JD Barnett. Hydrostatic limits in liquids and solids to 100 kbar. *Journal of Applied Physics*, 44(12):5377–5382, 1973. 75, 78

[64] Di L Decker. High-pressure equation of state for nacl, kcl, and cscl. *Journal of Applied Physics*, 42(8):3239–3244, 1971. 75

[65] HK Mao, J-A Xu, and PM Bell. Calibration of the ruby pressure gauge to 800 kbar under quasi-hydrostatic conditions. *Journal of Geophysical Research: Solid Earth (1978–2012)*, 91(B5):4673–4676, 1986. 76

[66] Kenichi Takemura. Pressure scales and hydrostaticity. *High Pressure Research*, 27(4):465–472, 2007. 77

[67] DV Antsyshkin, AN Dunaeva, and OL Kuskov. Thermodynamics of phase transitions in the system ice vi-ice vii-water. *Geochemistry International*, 48(7):633–642, 2010. 78, 88, 94

[68] Bart Olinger and Po Mo Halleck. Compression and bonding of ice vii and an empirical linear expression for the isothermal compression of solids. *The Journal of Chemical Physics*, 62(1):94–99, 1975. 78

[69] Ji Eun Lee, Gwanghyun Ahn, Jihye Shim, Young Sik Lee, and Sunmin Ryu. Optical separation of mechanical strain from charge doping in graphene. *Nature communications*, 3:1024, 2012. 79

[70] AC Ferrari and J Robertson. Resonant raman spectroscopy of disordered, amorphous, and diamondlike carbon. *Physical Review B*, 64(7):075414, 2001. 85, 86, 90

[71] LA Falkovsky. Symmetry constraints on phonon dispersion in graphene. *Physics Letters A*, 372(31):5189–5192, 2008. 94

[72] Pedro Venezuela, Michele Lazzeri, and Francesco Mauri. Theory of double-resonant raman spectra in graphene: Intensity and line shape of defect-induced and two-phonon bands. *Physical Review B*, 84(3):035433, 2011. 94